# An investigation of the structural and magnetic properties of Ho substituted $BiFeO_3$

A dissertation submitted to the Faculty of Science, University of the Witwatersrand, Johannesburg, in fulfillment of the academic requirements for the degree of Master of Science

by

Mehluli Ncube

**May 2012**

# DECLARATION

I declare that this dissertation is my own work, and it is being submitted for the degree of Master of Science in the University of the Witwatersrand, Johannesburg, and has not been submitted before for any degree or diploma examination in any other tertiary institution.

The measurements described in this dissertation were carried out at the School of Physics as well as the School of Chemistry, University of Witwatersrand, Johannesburg.

The data analysis and interpretation is my own original work, which was carried out under the supervision of Dr. Deena Naidoo (supervisor) and Professor Krishanlal Bharuth-Ram (co-supervisor). The work of other scientists is duly acknowledged in the text when used as a reference.

(Signature of Candidate)

Monday, May 14, 2012

# ABSTRACT

The doping of $BiFeO_3$ with lanthanide elements like Ho, with a radius smaller than Bi, is ideal to improve the ferroelectric and magnetic properties of $BiFeO_3$, which in principle can cause structural distortions of the lattice that improve the electrical and magnetic properties. In this work, we report on the temperature dependence of the structural and magnetic properties of Ho substituted $BiFeO_3$ (BHFO) samples, which have been investigated by X-ray diffraction (XRD) and Mössbauer spectroscopic techniques. The XRD and Mössbauer measurements were done at room temperature on the as-synthesized BHFO samples and after annealing the samples in Argon up to 1073 K. The resultant XRD patterns have shown that BHFO is of rhombohedral *R*3m space group, with a majority $Bi_{25}FeO_{90}$ phase and a minority $Bi_2Fe_4O_9$ phase. These two phases are attributed to the local stoichometry fluctuations in $BiFeO_3$ (BFO). A new phase was evident in the XRD spectra after annealing the sample between 673 – 873 K; this has been assigned to the octahedral B-site of $Fe_3O_4$.

The Mössbauer spectra were characterized by broadened features and the magnetic hyperfine splitting patterns were indicative of magnetic ordering mostly probably screwed or slightly antiferromagnetic ordering. The spectra were fitted with two symmetric sextets (S1 & S2) which were present in all annealed samples, a symmetric sextet (S3) which was observable at annealing temperatures greater than 673 K, a Lorentzian doublet (D) and a single line (SL) which were present in all spectra. The extracted hyperfine parameters of sextet S1 are consistent with those of rhombohedral $BiFeO_3$ and are characteristic of magnetically ordered $Fe^{3+}$. At $T_A$ > 673 K, a third sextet S3 was assigned to the high symmetry cubic spinel phase. The paramagnetic doublet D was attributed to the $Bi_{25}FeO_{40}$ phase and the singlet line SL to the $Bi_2Fe_4O_9$ phase which has been observed previously in the studies of $BiFeO_3$ and other $BiFeO_3$ doped systems. The isomer shift and quadrupole splitting values of the paramagnetic doublet D corresponds to an oxidation state of $Fe^{3+}$, while the isomer shift of S1 remained fairly constant up to $T_A$ = 623 K then decreased

gradually after the appearance of S3 indicating an increase of the *s*-electron density at the Fe nucleus. The quadrupole splitting of S2 showed no systematic change with annealing temperature, however at $T_A$ > 623 K this parameter changed dramatically to a negative value with a slightly larger magnetic field. The distribution of the isomer shift and the difference in the quadrupole splitting values and signs are due the variation in the angles between the principal axis of the electric field gradient (EFG) and the spin direction. The hyperfine fields of S1 and S2 remained fairly constant for all measured samples, however at $T_A$ > 623 K the hyperfine field of S3 showed a slight increase which could be due to Ho being substituted at the Fe site in $BiFeO_3$.

In addition, *in-situ* Mössbauer measurements at temperatures in the range 300 – 748 K were made on the BHFO samples. The room temperature spectrum showed similar features as observed on the annealing series of measurements. The hyperfine magnetic fields of the two sextet components (S1 and S2) decreased with increasing temperature and finally collapsed at $T$ > 588 K. The hyperfine fields of both the S1 and S2 components decreased systematically with temperature to a field distribution just below the Néel temperature. From our measurements, we estimated the Néel temperature for BHFO to be in the range 598 – 617 K. The isomer shift for all spectral components showed a linear decrease with increasing temperature which closely followed the usual second order Doppler shift variation with temperature. The S1 and S2 spectral components present at room temperature disappeared just before the Néel temperature resulting in the area fraction of the paramagnetic doublet D dominating the spectrum. From the site populations, an average Debye temperature ($\theta_D$) was estimated to be 240 ± 81 K for BHFO which is lower than the value of 340 ± 50 K cited for $BiFeO_3$.

# ACKNOWLEDGEMENTS

This work would not have been possible without the assistance provided by my supervisors, family, colleagues and friends. They have inspired and motivated me through my studies therefore I would like extend my appreciation to the following people.

I am indebted to my supervisor Dr. Deena Naidoo for his assistance during my experimental work and data analysis. I would also like express my sincere gratitude to him for proof reading my dissertation a number times and providing me with useful suggestions and feedback. Further, thank you Dr. Naidoo for your patience and many hours of consultation. Thank you so much and you have contributed immensely in my becoming a better scientist.

I am grateful to my co-supervisor Professor Krishanlal Bharuth-Ram for his invaluable expertise and his critical comments made on the dissertation. I would like to express my sincere appreciation to Professor H. P. Gunnlaugsson from the Aarhus University, Denmark, for his advice during data analysis of the Mössbauer spectra, and to Professor Dave Billing from the School of Chemistry, University of the Witwatersrand, for his assistance during X-ray diffraction measurements and data analysis. I am grateful for the financial support from the National Research Foundation (NRF) through the award of a grant-holder linked bursary. A special mention goes to Hilary and Wisdom for their input and discussions which assisted me immensely when compiling my dissertation.

I would like to thank my family for their patience and constant support and encouragement during my studies. I will be forever grateful to my wife, Buhle. When all has been said and done, God Almighty is my beginning and my end, and all the way in-between, and to Him I give all the praise and honor for taking me this far!

# TABLE OF CONTENTS

# LIST OF FIGURES

# LIST OF TABLES

*(page intentionally left blank)*

# CHAPTER 1: INTRODUCTION

Perovskite materials have generated much interest in recent years, particularly due to their electric and magnetic properties. More interesting is that these ferroelectric and antiferromagnetic properties are present at room temperature [1]. Such materials seem to be promising candidates for spintronics and magnetoelectronics. $BiFeO_3$ (BFO) is one such material that has received much attention, due to its long range magnetic ordering. This chapter gives a summary of the properties of BFO and its limitations. A comprehensive literature review of X-ray diffraction and Mössbauer spectroscopy studies of BFO systems is included in this chapter and potential applications are discussed.

## 1.1 Background Perovskite Materials

Perovskite materials are fascinating because they display a wide variety of fundamental properties, from magnetism to ferroelectricity, from colossal magneto-resistance to half-metallicity [2]. These materials are used in a number of important technological applications such as electromagnets, sensors and optical storage devices. In recent years multi-ferroic materials have attracted significant interest as they exhibit ferroelectric and ferromagnetic properties. In particular, after the discovery of large electric and magnetic polarization effects in thin BFO films [1], much attention has been devoted to the properties of $BiFeO_3$.

The quest to understand room temperature ferroelectricity of BFO has led to an advent of research in this area [3] and its possible applications. More interestingly is the possible existence of both electronic and magnetic properties in such a material, with miniaturization opening the possibility of combining [4] both these properties into a multi-functional material to produce a single device component to perform one task. Such materials are rare in nature as the conditions of being simultaneously

ferroelectric (materials with a spontaneous electric polarization that can be switched on by an applied electric field) and ferromagnetic (empty and partially filled transition metal orbits) cannot exist at the same time [5].

BFO is an inorganic chemical compound with a rhombohedrally distorted perovskite structure [6] of space group R3c, as shown in Figure 1.1. BFO has a high Curie temperature ($T_C$) of approximately 1143 K and a high Néel temperature ($T_N$) of approximately 647 K [7].

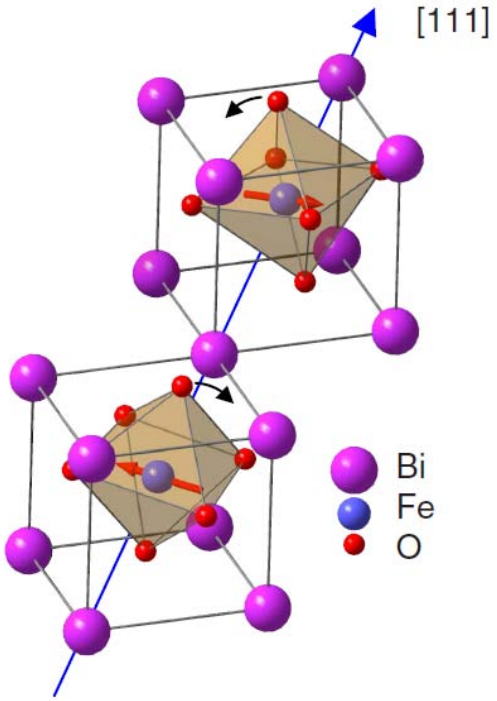


**Figure 1.1: A typical perovskite structure. The red arrow indicates the orientation of the magnetic moment in the (111) plane. The O, Fe and Bi atoms are indicated by red, blue and purple spheres, respectively [8].**

BFO exhibits both ferroelectric and ferromagnetic properties in the same material, i.e. an electric field can induce a change in the magnetization whilst an external magnetic field can induce electric polarization [6]. This phenomenon is known as the magneto-electric effect (ME) effect and materials exhibiting this effect are called magneto-electrics. The ability to couple to either the electric or the magnetic polarization allows an additional degree of freedom in the design of devices. The

sensor industry relies heavily on ferroelectric materials. In addition many ferroelectrics are also ferroelastic meaning a change in their electric polarization is accompanied by a change in their shape resulting in their use to convert sound waves into electrical signals in sonar detectors and to convert electrical impulses into motion in actuators [9].

Spontaneous magnetization occurs when ferromagnetic materials tend to concentrate magnetic flux density (large positive permeability) which leads to their widespread use in applications such as transformer cores, permanent magnets, and electromagnets, for which large magnetic fields are required [10]. Such materials are of interest because they exhibit long range magnetic ordering as well as electric ordering, and are one of the most promising lead-free piezoelectric materials exhibiting multi-ferroic properties at room temperature [11]. There have been many attempts to improve the electrical properties of BFO by doping it with Ba [5], Pb [12] and other rare earth elements such as Ce [13] and Sm [14]. It has been found that substituting certain elements in BFO causes a systematic structural change which increases the ferromagnetic property of the material [15]. In the present project Ho was used as a dopant.

Most single-phase ferro-electromagnetic materials have very few technological applications either due to their low Néel or Curie temperature. However, materials such as $BiFeO_3$ (BFO), and in this case Ho substituted $BiFeO_3$ (BHFO), has a high Néel ($T_N$ ~ 640 K) and high Curie temperature ($T_C$ ~ 1143 K) opening the possibility of potential applications [16] such as storage devices, sensors, actuators and transducers.

## 1.2 Literature review of $BiFeO_3$

$BiFeO_3$ has been reported to have a rhombohedrally distorted perovskite [11] corresponding to the group *R*3*c* structure with unit cell parameters of $a$ = 3.96 Å and $\alpha$ = 89°28', with $Fe^{3+}$ and $Bi^{3+}$ ions displaced along the (111) direction. The space

group *R*3*c* allows for both ferroelectric atomic displacements [17] and weak ferromagnetism below the Néel temperature ($T_N$), which has been observed to be around 640 K. Sosnowska *et al.* [18] showed that each $Fe^{3+}$ spin is surrounded by six anti-parallel spins of Fe nearest neighbors which forms a G-type antiferromagnet. This implies that the Fe magnetic moments are coupled ferromagnetically within the pseudo-cubic (111) planes and anti-ferromagnetically between the adjacent planes [19]. Figure 1.2 shows an illustration of G-type antiferromagnetism.

Holmium ferrite, $HoFeO_3$, exhibits interesting electrical, magnetic and optical properties that can be used mostly in optical memory systems. The crystal structure group is in 14 classes, orthorhombic and of space group *Pbnm.* It exhibits a distorted perovskite (as shown in Figure 1.1) but with Fe environment remaining essentially octahedral.

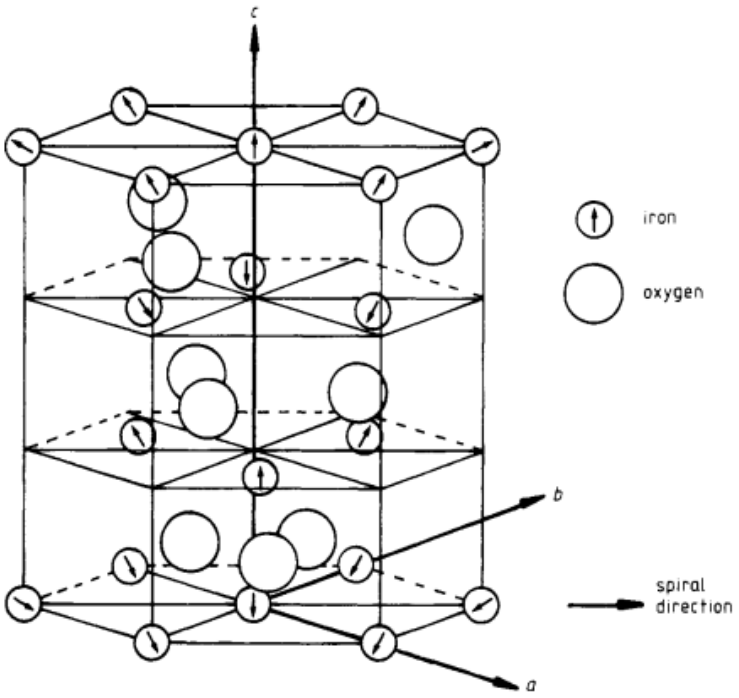


**Figure 1.2: An illustration of G-type ferromagnetic spin alignment of Fe and O atoms [18].**

Blaauw and Van der Woude [11] carried out X-ray studies on the lattice parameters of BFO and found that a number of phase transitions altered the electric ordering in the ferroelectric material. Neutron diffraction measurements on BFO conducted by Fischer *et al.* [17] confirmed that long-range magnetic ordering exists in BFO and at temperatures around 604 K, a paramagnetic state was observed. In Mössbauer experiments, this paramagnetic state was observed in the form of a quadrupole split doublet located at the centre of the Mössbauer spectra, which de Sitter *et al.* [19] identified as the $Bi_2Fe_4O_9$ phase. This phase was also observed by Blaauw and Van der Woude [11] and Fischer *et al.* [17].

Blaauw and Van der Woude [11] performed *in-situ* Mössbauer measurements on $BiFeO_3$ and at 80.6 K their spectra were characterized by a magnetically split feature which transformed into a quadrupole split doublet at 657.3 K. This effect is illustrated in Figure 1.3.

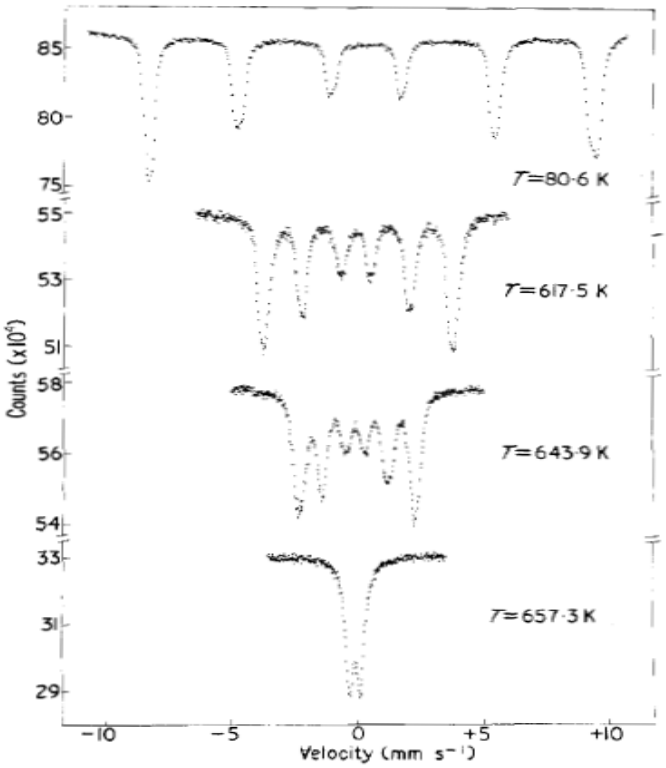


**Figure 1.3:** ***In-situ*** **Mössbauer measurements on BFO recorded at different temperatures [11].**

The doublet component was attributed to the minor impurity phases of and $Bi_2FeO_{49}$ as observed by other authors [17] [19]. Blaauw and Van der Woude also found some discontinuity of the isomer shift around $T_N$ and this was attributed to an increase in the *s*-electron density at the Fe-nucleus.

The magnetic hyperfine field results determined by Blaauw and Van der Woude [11] for BFO show a clear temperature dependence and are consistent with the results obtained for other rare earth orthoferrites such as $LuFeO_3$ and $LaFeO_3$ [20]. A plot of the internal magnetic field as a function of the reduced temperature for $LaFeO_3$ and $LuFeO_3$ shows that the $BiFeO_3$ results fall within these two curves. Therefore, Blaauw and Van der Woude [11] suggested that the room temperature magnetic ordering of BFO is antiferromagnetic which exists above $T_N$, which is modulated with a period of 620 Å. Furthermore, their results revealed that the spectral linewidth was broader than the instrumental linewidth indicative of the non-equivalence of Fe-positions. At temperatures, $T$ > 850 K, the samples used in their work decomposed gradually in the furnace. Table 1.1 presents a summary of the hyperfine parameters determined by Blaauw and Van der Woude [11] for BFO.

**Table 1.1: Hyperfine parameters extracted from *in-situ* Mössbauer measurements on $BiFeO_3$ [11].**

| Temp (K) | $\delta_1$ (mm.s$^{-1}$) | $\delta_2$ (mm.s$^{-1}$) | $\Delta E_Q$ (mm.s$^{-1}$) | $\Delta E_Q$ (mm.s$^{-1}$) | $B_{hf}$ (T) | $B_{hf}$ (T) |
|---|---|---|---|---|---|---|
| 80 | 0.480 | 0.48 | 0.35 | -0.13 | 17.60 | 17.50 |
| 412 | 0.30 | 0.30 | 0.33 | -0.13 | 14.34 | 14.25 |
| 657.3 | - | - | 0.44 | - | - | - |

### 1.2.1 Applications of BFO

The coexistence of both the electric and magnetic ordering in $BiFeO_3$ at room temperature is of particular interest in technological applications. As BFO is a charge-transfer insulator with an energy gap of approximately 2.5 eV, it allows carrier excitation with commercially available femtosecond laser pulses, and hence, enables the development of ferroelectric ultrafast optoelectronic devices as widely

demonstrated in semiconductors [21], and such thin films can be used in nonvolatile random access memory. The high sensitivity of bulk ceramic BFO to ethanol and acetone vapor opens possibilities in semiconductor gas sensors [22].

## 1.3 Literature review of doped BFO

The doping of BFO with rare earth materials $R_{1-x}M_xFeO_3$ mainly depends on the ionic radius difference between $R^{3+}$ and $M^{2+}$ and the synthesis processes [23]. Li *et al.* [24] observed that the substitution of $R^{3+}$ in $RFeO_3$ by $M^{2+}$ may have at least three possible consequences. One such possibility is that $R_{1-x}M_xFeO_3$ can consists of two phases, an orthorhombic and a cubic phase as in the case of $La_{1-x}Ba_xFeO_3$, where the iron in the cubic phase was found to have an intermediate valence state between the trivalence and the tetravalence.

An earlier Mössbauer study performed by Wang [25] on $Bi_{1-x}Sr_xFeO_3$ at room temperature suggested that the Néel temperature was above room temperature, and the magnetic hyperfine splitting indicated that the magnetic ordering was most probably slightly canted antiferromagnetic. The isomer shift and hyperfine field for $Bi_{1-x}Sr_xFeO_3$ for $x$ = 0.3 was found to be similar to that of BFO, which is 0.39 mm.s$^{-1}$ and 49.7 T, respectively. Such parameters for a single six-line sub-spectrum correspond to an asymmetrically tetrahedral surrounded trivalent Fe in oxides [26].

In a recent room temperature Mössbauer investigation of Pb doped BFO samples, Khomchenko *et al.* [12] found two six-line spectra in a magnetically ordered state with the following parameters: $B_{hf1}$ = 50 T, $B_{hf2}$ = 46.1 T, $\delta_1$ = 0.394 mm.s$^{-1}$, and $\delta_2$ = 0.484 mm.s$^{-1}$. These results compare favorably with the Mössbauer hyperfine parameters obtained by Kothari *et al.* [27] for Eu doped BFO ceramics. A room temperature Mössbauer spectrum of a BFO sample doped with 15% Eu was characterized by a doublet with an isomer shift value of 0.393 mm.s$^{-1}$ and a sextet with a hyperfine field of 49.15 T. At temperatures above the Néel temperature, their spectra were described by a quadrupole split doublet with an isomer shift and quadrupole splitting of 0.151 mm.s$^{-1}$ and 0.242 mm.s$^{-1}$, respectively. The quadrupole

split doublet was attributed to $Bi_2Fe_4O_9$, which was similar assignment given for this component by De Sitter *et al.* [19] and Fischer *et al.* [17]. At 10% doping by Eu, the room temperature spectrum were characterized by a sextet and a quadrupole split doublet with the following components $B_{hf}$ = 49.21 T, and $\delta$ = 0.394 mm.s$^{-1}$. Above the Néel temperature the magnetic hyperfine field disappeared and the quadrupole split doublet dominated the spectrum with parameters $\Delta E_Q = 0.388 \pm 0.03$ mm.s$^{-1}$ and $\delta = 0.114 \pm 0.02$ mm.s$^{-1}$.

Fiebig [28] reported that spontaneous magnetization was induced in BFO by changing either the Fe-O-Fe bond angle or by a statistical octahedral distribution of Fe with mixed valence and chemical substitution from which he concluded that different substitutions tend to enhance certain properties of BFO. Kothari *et al.* [29] performed studies on Mn substituted BFO thin films and found that these materials showed enhanced properties in terms of leakage currents. At room temperature, their Mössbauer spectra of Mn doped BFO (10%) were characterized by a sextet and a quadrupole split doublet. Mössbauer measurements conducted at temperatures above $T_N$ showed no existence of multiple oxidation states with increasing Mn doping, as the isomer shift values of $0.179 \pm 0.016$, $0.216 \pm 0.005$, and $0.209 \pm 0.002$ mm.s$^{-1}$ all corresponded to only the $Fe^{3+}$ state.

A number of researchers [30] [31] have reported high leakage currents in BFO, hence making it difficult to observe ferroelectric loops at room temperature. Li *et al.* [5] demonstrated that doping BFO with Ba seems to solve this leakage problem, although some films showed large difference in properties due to their crystalline structure, stress, grain size and composition. For $Bi_{1-x}Ba_xFeO_3$ with $x$ = 0.25, both ferroelectric and ferromagnetic properties were observed at room temperature by P–E (Polarization Electric Field) and M–H (Magnetic Hysteresis) loops. Mössbauer measurements performed on Lanthanum and Holmium ferrites by Pina *et al.* [32] at room temperature resulted in spectra that were characterized by a six line spectra with an isomer shift of 0.385 mm.s$^{-1}$, a quadrupole splitting of 0.005 mm.s$^{-1}$, and a

hyperfine magnetic field of 50.4 T. The isomeric values correspond to the $Fe^{3+}$ state, with a $3d^5$ configuration of the Fe ion which is octahedral.

Previous studies carried out by Kothari *et al*. [27] have shown that $Eu^{3+}$ doping at the Bi sites in BFO have improved the magnetic properties of the BFO material suggesting that multiferroics can be modified by substitutional incorporation at the Bi or Fe sites. Recent studies [33] have demonstrated that it is possible to switch and control local ferromagnetism with an electric field which allows for the exploitation of multiferroic BFO. Ferroelectric switching of polarization has been observed under applied electrical bias conditions, and such results open the possibility of customizing the ferroelectric properties and the probability of rapid implementation of the ferroelectric BFO with the existing data storage technologies [34].

Such possibilities greatly reduce the writing energy of the magnetic random access memory elements, setting up a new avenue to magnetoelectric random access memory elements [27], an exciting new area of condensed-matter research with an unlimited potential to affect magnetic data storage, spintronics and high-frequency magnetic devices. Table 1.2 gives a list of hyperfine parameters extracted from Mössbauer studies of selected ferromagnetic compounds.

**Table 1.2: Hyperfine parameters extracted from Mössbauer studies of different ferromagnetic compounds, where $2\varepsilon = \Delta E_Q$.**

| Compound | $\delta$ (mm.s$^{-1}$) | $\Delta E_Q$ (mm.s$^{-1}$) | $B_{hf}$ (T) |
|---|---|---|---|
| $BiFeO_3$ [1] | | | |
| Sextet 1 | 0.397 | -0.146 | 49.1 |
| Sextet 2 | 0.401 | 0.282 | 49.7 |
| Doublet at 650 K | 0.130 | 0.440 | NR |
| $Bi_{25}FeO_{40}$ doublet [35] | 0.209 | - | - |
| $Bi_{25}FeO_{40}$; $Bi_{12}Fe_4O_9$ Doublet [36] | 0.16 | 0.830 | - |
| $Bi_2Fe_4O_9$ [37] | | | |
| Doublet 1 | 0.494 | 0.960 | - |
| Doublet 2 | 0.619 | 0.383 | - |
| $Fe_3O_4$ [38] | | | |
| A-site Sextet | 0.28 | - | 49.0 |
| B-site Sextet | 0.66 | - | 46.0 |
| $Bi_{0.5}Sr_{0.05}FeO_3$ [23] | | | |
| Sextet 1 | 0.37 | -0.12 | 50.7 |
| Sextet 2 | 0.21 | 0.34 | 42.4 |
| $LaFeO_3$ | 0.395 | 0.007 | 52.8 |
| $Bi_{0.8}Pb_{0.2}FeO_3$ [12] | | | |
| Sextet 1 | 0.39 | - | 50.0 |
| Sextet 2 | 0.48 | - | 46.1 |
| $BiMn_{0.05}Fe_{0.95}O_3$ [39] | | | |
| sextet | 0.36 | -0.18 | 50.9 |
| doublet 1 | 0.40 | 0.63 | - |
| doublet 2 | 0.21 | 0.75 | - |
| Eu doped $BiFeO_3$ [27] | | | |
| 693 K sextet | 0.383 | - | 49.98 |
| 693 K $Bi_2Fe_4O_9$ doublet | 0.141 | 0.444 | - |

## 1.4 Objectives of the study

As illustrated in the literature review, there exists much interest in BFO. However, there are still drawbacks such as the high leakage current which hampers its use in devices. For this reason, it is difficult to obtain good ferroelectricity and reliability [40] of BFO, challenging its technological applications. It is well known that Holmium (Ho), like Lanthanum (La), belongs to the Lanthanides. With the ionic radius of $Ho^{3+}$ (1.05 Å) being smaller than that of $Bi^{3+}$ (1.20 Å), it is expected that Ho

doping could induce structural distortions, leading as in the case of other rare earth dopants in improving the electrical and magnetic properties of Ho substituted BFO ceramics as reported by Al-Haj [41].

Due to the same valence of Ho ions with respect to Bi ions, Ho ion substitution is not expected to suppress the oxygen vacancies, which has been reported to be the cause of the decrease in leakage current [42] of BFO both in bulk and thin film as observed by Wang [43] in the case of Ce doped BFO. Therefore Ho seems to be a promising dopant for Bi in BFO to further improve the ferroelectric properties by reducing the leakage current density of BFO thin films. It is envisaged that Ho will most likely suppress the impurity phases that normally appear in BFO, which causes the reduction of leakage current which normally happens due to the suppression of mobile defects.

In order to enhance the electronic structure and properties of multiferroic materials, the understanding of the physical mechanisms of the family of perovskite-related transition metal oxides $RM_xFeO_3$ is important [23] and needs to be pursued. The chemical substitution of BFO coupled with the study of their structural as well as magnetic properties of the dopant can correlate the observed magnetic properties of the Ho substituted BFO (BHFO) system. Thus far there is no evidence of Mössbauer reports on the BHFO synthesized material. Therefore we embarked on a study of the structural and magnetic properties of BHFO using X-ray diffraction (XRD) and Mössbauer spectroscopy (MS). The results are compared with other rare earth substituted $BiFeO_3$ systems.

X-ray diffraction measurements were performed at room temperature using a Bruker D2 Phaser desktop diffractometer at room temperature, which employs a sealed tube Cu- X-ray source equipped with a Bruker Lynxeye PSD detector using 2.5° primary and secondary beam radial Soller slits as well as a secondary beam Ni filter.

The following Mössbauer measurements have been conducted on the Ho substituted $BiFeO_3$ in standard transmission geometry using $^{57}Co$ in an Rh matrix:

- At room temperature on the as-synthesized samples;
- At room temperature after annealing up to 873 K in Argon atmosphere;
- *In-situ* measurements from 300 K up to 748 K.

# CHAPTER 2: THEORY

This chapter will focus on the theory associated with X-ray diffraction (XRD), the Mössbauer effect, as well as the basic principles of magnetism. The first section describes the XRD technique, how data is acquired and manipulated to probe the structural properties of BHFO. A comprehensive review of the Mössbauer effect will follow. The final part of the chapter will include an overview of magnetism.

## 2.1 X-ray Diffraction

When an X-ray beam strikes an atom, the electrons surrounding the atom oscillate due to the presence electromagnetic field with the same frequency as the incoming X-ray beam. Atoms in a crystal are arranged in a regular pattern, causing the striking beam to produce constructive interference. The waves will be in phase resulting in well defined X-ray beams leaving the sample at various directions with a large number of scattered rays mutually reinforcing one another. From the angles and intensities of these diffracted beams, one can produce a three-dimensional picture of the density of electrons within the crystal. It is from this electron density, that the mean positions of the atoms in the crystal can be determined, as well as their chemical bonds.

### 2.1.1 Lattice Planes and Bragg's Law

X-rays primarily interact with electrons in atoms. When X-ray photons collide with electrons, some photons from the incident beam will be deflected away from the original direction of travel. These scattered X-rays carry information about the electron distribution in materials. The diffracted waves from different atoms can interfere with each other and the resultant intensity distribution is strongly modulated by this interaction. If the atoms are arranged in a periodic pattern, as in crystals, the

diffracted waves will consist of sharp interference maxima with the same symmetry as in the distribution of atoms. Measuring the diffraction pattern therefore allows a deduction of the distribution of atoms in a material.

The resultant peaks from X-ray diffraction patterns are directly related to the atomic distances. Figure 2.1 shows an incident X-ray beam interacting with the atoms which are arranged in a periodic manner. The spacing between the atomic planes occurs over a distance, *d*, and ray 1 reflects off the upper atomic plane at an angle $\theta$ equal to its angle of incidence.

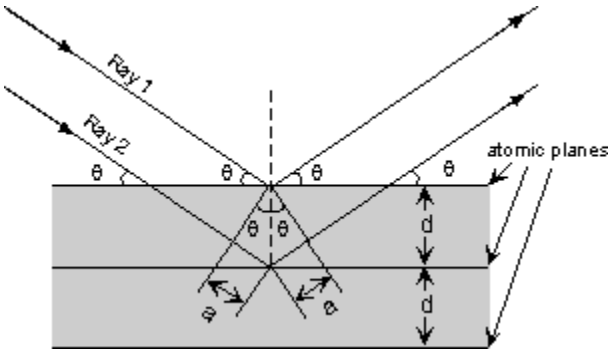


**Figure 2.1: Bragg's law derivation from two incident rays on atomic planes.**

Similarly, if ray 2 reflects off the lower atomic plane at the same angle $\theta$, while it travels a distance of $2a$ farther than ray 1, and this distance $2a$ being equal to an integral number of wavelengths ($n\lambda$), then the condition for constructive interference to occur will be

$$n\lambda = 2a. \tag{2.0}$$

Using trigonometry, in terms of the spacing, *d*, between the atomic planes gives,

$$a = d \sin\theta \tag{2.1}$$

Hence from equation (2.0) and (2.1) we get,

$$n\lambda = 2d \sin\theta. \tag{2.2}$$

This is Bragg's Law for X-ray diffraction which allows us to compute the atomic spacing (*d*-spacing) between the atomic planes.

### 2.1.2 Powder X-ray Diffraction

Powder XRD is one of the most widely used X-ray diffraction technique for characterizing materials. The sample is usually in a powder form, which has crystalline domains which are randomly oriented. When a 2-D diffraction pattern is recorded, it shows concentric rings of scattering peaks corresponding to the various *d*-spacings in the crystal lattice. The positions and the intensities of the peaks are used to identify the underlying structure or phase of the material. Powder diffraction data can be collected using either transmission or reflection geometry, as shown in Figure 2.2. In a powder sample, the particles are randomly oriented; hence these two methods (transmission and reflection) will yield the same data.

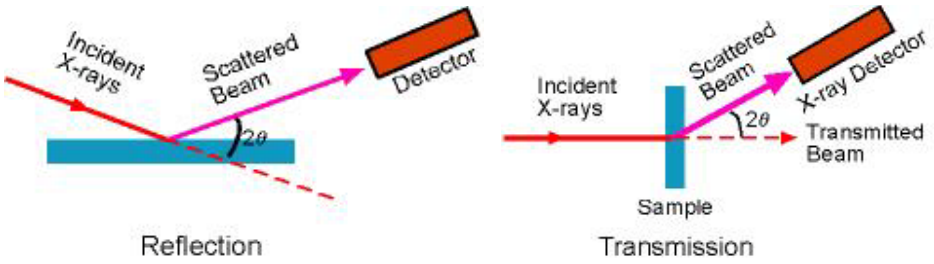


**Figure 2.2: Reflection and Transmission geometry in Powder X-ray diffraction.**

Table 2.1 lists the experimentally determined $K_\alpha$ wavelengths for commonly used materials in X-ray tubes.

**Table 2.1: Commonly used targets with corresponding wavelengths** [44]**.**

| Element | $K_\alpha$ Wavelength $\lambda$ (Å) |
|---|---|
| **Mo** | 0.7107 |
| **Cu** | 1.5418 |
| **Co** | 1.7902 |
| **Fe** | 1.9373 |
| **Cr** | 2.2909 |

## 2.2 Mössbauer Effect

The Mössbauer effect is the resonant recoilless absorption and emission of $\gamma$-rays by nuclei in a solid, i.e. without the loss of energy to recoil. This phenomenon provides a means of studying the local atomic environment around the Mössbauer probe nuclei [45]. The interactions between the nucleus and the electrons depend strongly on the electronic, chemical and magnetic state of the atom. These interactions provide information through the hyperfine parameters, viz. isomer shift, quadrupole splitting and magnetic hyperfine field, which can be determined experimentally from the line positions and the splitting in a Mössbauer spectrum.

In 1958, Rudolph Ludwig Mössbauer (hence the Mössbauer effect named after him) discovered that for an emitting and absorbing nuclei bound in a solid, a certain fraction of gamma rays are emitted and absorbed with negligible energy loss due to recoil. When this happens in both the source and absorber, the condition for resonant absorption of gamma rays is satisfied. Mössbauer's discovery of the recoilless emission and absorption of $\gamma$-rays allows for the possibility of detecting minute changes in nuclear energy levels of the order of $10^{-12}$ eV. The high resolution of recoil-free emission and absorption of 14.4 keV $\gamma$-rays allows such small energy perturbations of the order of $10^{-7}$ to $10^{-8}$ eV to be detected and hence the knowledge of the local atomic environment of the nuclei can be deduced. When a nucleus is in an excited state of energy $E_e$ with $Z$ protons and $N$ neutrons it decays by emitting a $\gamma$ - photon to the ground state of energy $E_g$, as shown in Figure 2.3.

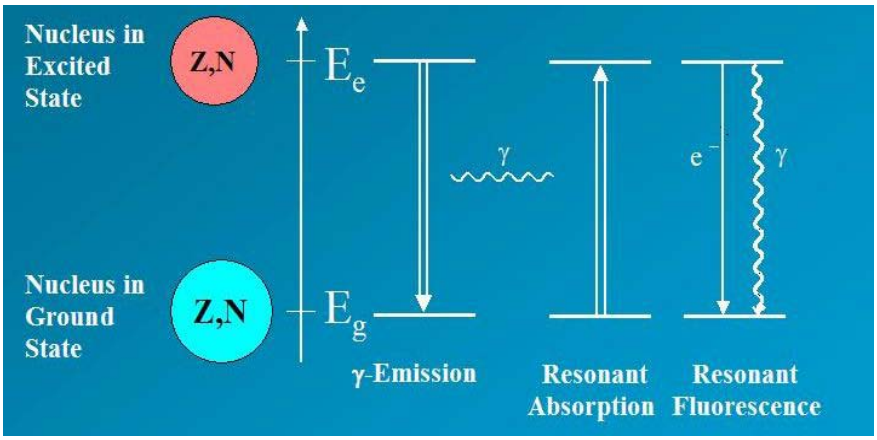


**Figure 2.3: Mössbauer effect, recoilless nuclear resonance absorption and fluorescence of $\gamma$-radiation.**

The $\gamma$ photon energy ($E_o$), where $E_o = E_e - E_g$, may be absorbed by a nucleus of the same proton and neutron number in the ground state, and the transition (resonant absorption) to the excited state $E_e$ can take place, hence producing a resonant fluorescence $\gamma$-ray photon. Conventional $^{57}$Fe-Mössbauer spectroscopy uses the radioactive $^{57}$Co(Rh) isotope as a source, which decays by electron capture to an excited state of $^{57}$Fe which emits 14.4 keV gamma rays ($\gamma$-rays) as it subsequently decays to its ground state, as depicted in Figure 2.4.

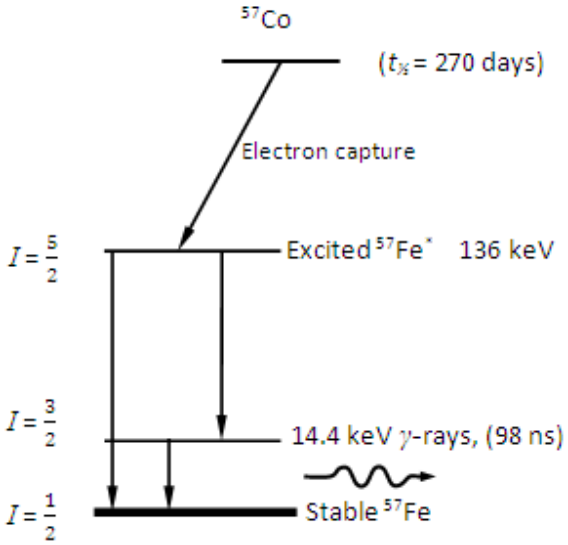


**Figure 2.4: Decay scheme for $^{57}$Co.**

### 2.2.1 Nuclear resonance and Natural linewidth

The mean lifetime ($\tau_N$) regulates the resonance for any particular nuclide. The mean lifetime has impact on the resonant lines as stated by Heisenberg's uncertainty principle

$$\Gamma = \frac{\hbar}{\tau_N}. \tag{2.3}$$

where $\Gamma$ is the linewidth, $\hbar = h/2\pi$ ($h$ is the Planck's constant) and $\tau$ is the mean life of the excited state. For $^{57}$Fe which has an energy transition of 14.4 keV, and a mean lifetime of 141 ns, gives us an energy resolution of $5\times10^{-9}$ eV, which inarguable gives Mössbauer spectroscopy the highest resolution as compared to other spectroscopic methods. Maximum resonance only occurs when the spectral line for emission as well as that of absorption appears at the same energy position. Therefore, the distribution of energies about $E_o$, where $E_o$ is the mean energy of the transitional probability as a function of transitional energy $E$, as given by the Breit-Wigner formula is;

$$I(E) = \frac{(\Gamma/2)^2}{(E - E_o)^2 + (\Gamma/2)^2} \tag{2.4}$$

where $\Gamma$ is the energy linewidth of the excited $^{57}$Fe nucleus.

This relative intensity as a function of transition energy can be expressed graphically as shown in the Figure 2.5,

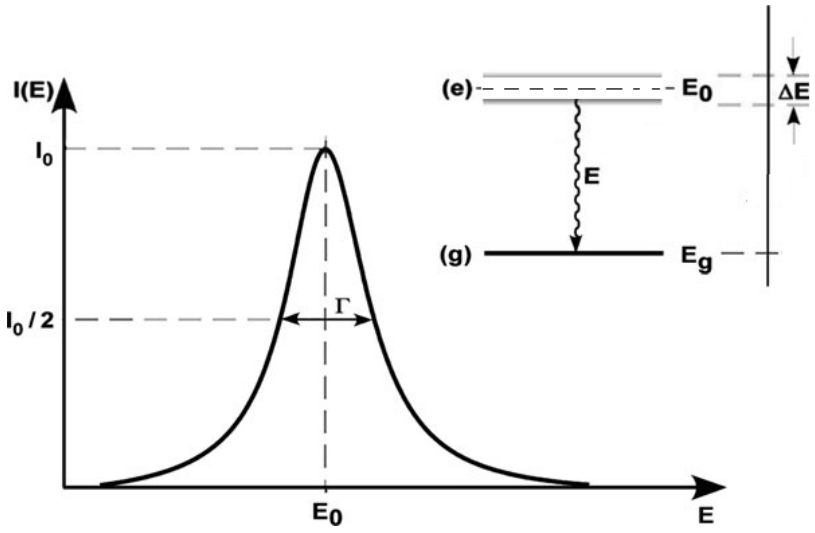


**Figure 2.5: Intensity *I*(*E*) as a function of transition energy (*E*) [46].**

### 2.2.2 Recoil-free fraction and thermal broadening

When a $\gamma$-ray is emitted from an excited nucleus of mass *M*, a recoil is imparted to the nucleus which results in the nucleus moving with some velocity ($v$) in the opposite direction, as shown in Figure 2.6. The nucleus will possess kinetic energy given by

$$E_R = \frac{1}{2}Mv^2. \tag{2.5}$$

The principle of conservation of momentum will thus require that

$$p_n = -p_\gamma = -\frac{E_\gamma}{c} \tag{2.6}$$

where $p_\gamma$ and $p_n$ are the linear momenta of the nucleus and the photon respectively. $E_\gamma$ is the energy of the emitted photon given by

$$E_\gamma = E_0 - E_R. \tag{2.7}$$

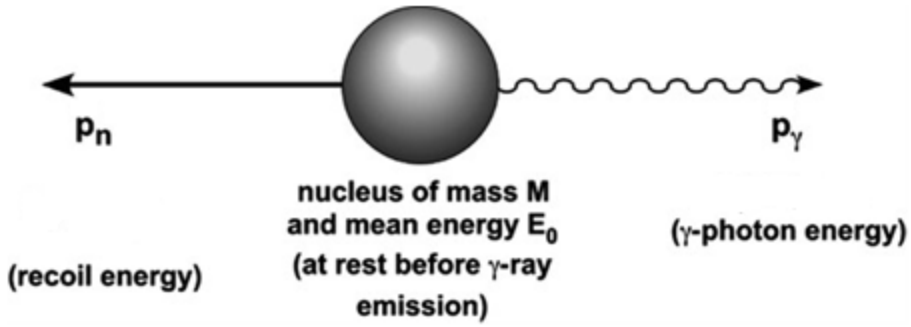


**Figure 2.6: Recoil energy of the excited nucleus [46] showing the directions of the recoil and the *γ*-photon.**

When the nucleus is embedded in a solid, a fraction of the gamma photons are emitted without transfer of energy to nuclear recoil. The recoil free fraction depends on three variables, namely the recoil free energy, which is proportional to $E_\gamma^2$, the lattice properties, and the ambient temperature [47]. The energy of the *γ*-ray may cause excitation of a lattice vibrational mode, because not all nuclei undergo recoil-free transitions hence decreasing the energy of the emitted particle.

The fraction of this emission with zero phonon excitation is known as the recoil free fraction, *f*, or Mössbauer-Lamb factor. The Mössbauer factor is a measure of the probability of recoil-free resonance fluorescence of *γ*-photons. Hence *f* will tend to be larger when the probability of exciting the lattice vibration is small, which in essence means lower *γ*-ray energy. As the binding energy of the atom gets stronger in the lattice, the temperature reduces as the vibrational energy gets lower. The recoil free fraction is defined as the number of recoil-free *γ* events (emission or absorption) divided by the total number of *γ* events. If there is no energy lost to the lattice, the probability that a zero-phonon transition occurs, is given by:

$$f = e^{-k^2 \bullet x^2}, \tag{2.8}$$

where *f* is finite. Since $k^2 = \frac{4\pi^2}{\lambda^2} = \frac{E_\gamma^2}{(\hbar c)^2}$, where $\lambda$ is the wavelength of the *γ*-ray.

The recoil free fraction *f* can be written as;

$$f = \exp\left[\frac{-4\pi^2\left\langle x^2\right\rangle}{\lambda^2}\right] = \exp\left[\frac{-E_\gamma^2\left\langle x^2\right\rangle}{(\hbar c)^2}\right] \tag{2.9}$$

In the above equation, $\left\langle x^2\right\rangle$ is the mean square vibrational amplitude of the emitter or absorber nucleus in the direction of the $\gamma$-ray. The probability of a recoil free transition therefore decreases exponentially with the square of the $\gamma$-ray energy. It should be noted that $f$ increases exponentially with decreasing $\left\langle x^2\right\rangle$ which depends on the temperature and the strength of the binding energy. The Mössbauer effect can therefore be detectable in solids and viscous fluids, as the displacement of the nucleus must always be small compared to the wavelength of the $\gamma$-ray. For a Debye model approximation which is valid for cubic monatomic crystals, $f$ is given by

$$f = \exp\left\{-\frac{6E_R}{k_B\theta_D}\left[\frac{1}{4}+\left(\frac{T}{\theta_D^2}\right)^2\int_0^{\frac{\theta_D}{T}}\frac{x}{e^x-1}dx\right]\right\} \tag{2.10}$$

where $k_B$ is Boltzmann constant, $T$ is the temperature and $E_R$ is the recoil energy of the nucleus of mass $m_N$ expressed as

$$E_R = \frac{E_\gamma}{2m_Nc^2}. \tag{2.11}$$

In equation (2.10), $\theta_D$ refers to the Debye temperature [48], defined as

$$\theta_D = \frac{\hbar\omega_D}{k_B} \tag{2.12}$$

where $\omega_D$ is the Debye frequency limit. For higher temperatures ($T \geq \frac{\theta_D}{2}$), $f$ can be approximated to

$$f = \exp\left\{-\frac{6E_RT}{k_B\theta_D^2}\right\}. \tag{2.13}$$

In the lower temperature limit, ($T << \theta_D$), $f$ is approximated to

$$f = \exp\left\{-\frac{E_R}{k_B\theta_D}\left(\frac{3}{2}+\frac{\pi^2T^2}{\theta_D^2}\right)\right\} \tag{2.14}$$

where $\theta_D$ is a measure for the strength of the bonds between the lattice and the Mössbauer atom. From equation (2.14), $f$ increases with decreasing recoil energy, decreasing temperature, and with increasing Debye temperature.

### 2.2.3 Hyperfine interactions

The energy of the nucleus in a solid is influenced by the chemical environment of its atoms and can be described by the following Hamiltonian:

$$H = H_o + H_{is} + H_{hf} + H_{efg} \tag{2.15}$$

where

$H_o$ represents all terms excluding the hyperfine interaction with the immediate environment.

$H_{is}$ represents the coloumbic interaction between the probe nucleus and the electrons in its neigbourhood.

$H_{hf}$ represents the magnetic interaction of the nuclear spin with the magnetic field in its immediate vicinity.

$H_{efg}$ represents the electric quadrupole interaction between the nuclear quadrupole moment and the local electric field gradient produced by the surrounding charge distribution [49].

The nucleus and its surrounding electrons experience interactions which lead to some changes in the energy levels. It is important to note that with these hyperfine interactions, Mössbauer spectroscopy serves as an immediate probe to the

interactions in the nuclear surroundings, hence giving the ability to monitor the energy level changes. These changes can arise from factors including altering the thermodynamic parameters and changes to the structure which can be either due to stress or strain to either the crystalline or amorphous type of structure, lattice periodicity and many other cases.

#### 2.2.3.1 Electric monopole interaction: Isomer shift

The isomer shift reflects the chemical bonding environment of the Mössbauer active atom and is a function of the *s*-electron density at the nucleus. It results from the Coulomb interaction between the nuclear charge distribution and the *s*-electronic charge density. The interaction energy between the total electronic charge distribution $\rho(\boldsymbol{r})$ and the electrostatic potential $V_{Ne}(\boldsymbol{r})$ generated by charged nucleons is given by:

$$E_{Ne} = \int \rho(r) E_{Ne}(r) dr \tag{2.16}$$

If the nucleus is a point-charge, then the interaction energy would be the same for the ground and excited states of the nucleus. The electron-nuclear interaction would then generate a constant shift of the nuclear energy levels and there would be no isomer shift in Mössbauer experiments [46]. The isomer shift is evident in the spectra as a shift (either to the left or the right) of all the peaks corresponding to a particular atomic environment, as shown in Figure 2.7.

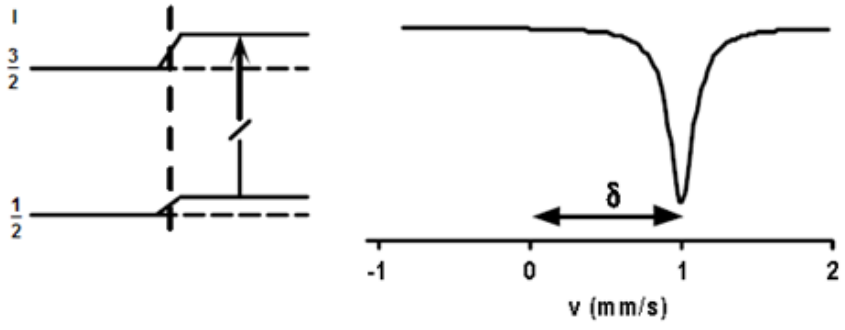


**Figure 2.7: Mössbauer transition and the resulting spectra, which gives the isomer shift $\delta$ [46].**

The isomer shift is usually reported with respect to some standard absorber like metallic iron foil. From the measured values of the isomer shift, one can obtain valuable information about the chemical environment of the nucleus under investigation such as oxidation states and the electronic spin-states (high- or low-spin) of the Mössbauer active atom in the absorber. When additional hyperfine interactions are present, the isomer shift sets the position of centre of gravity for the whole Mössbauer spectrum [50].

When the nuclear radii of the ground and excited states are known, which are the relevant nuclear parameters obtained from the isomer shift; the electronic parameters like the electronic densities can then be derived. The isomer shift is therefore an essential probe to determine the atomic oxidation states, which has proved to be difficult to obtain by other techniques. Any changes in the isomer shift can also reflect the influences on the electronic environment caused by the shielding of one set of electrons by another and covalence effects. Typical $^{57}$Fe isomer shift values as a function of oxidation states are shown in Figure 2.8.

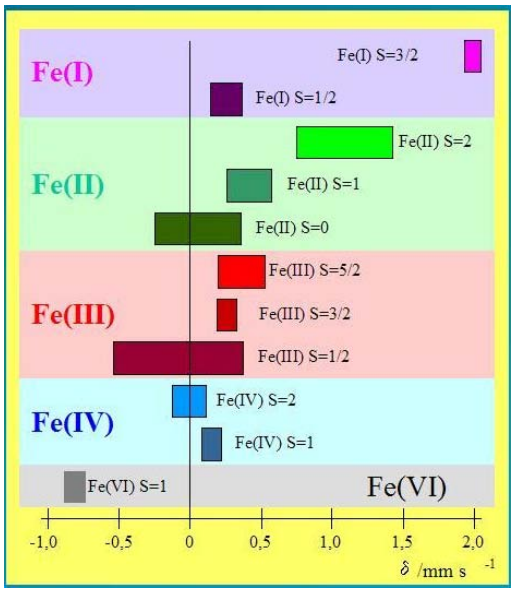


**Figure 2.8: Typical isomer shift values in iron compounds [51].**

The above diagram shows the range of isomer values observed in iron compounds for both high spin and low spin states. For high spin states, the isomer values become

more positive due to the shielding of the 3d electrons, whereas the low spin states are less positive. It should be noted though that low spin states for iron (II) and (III) compounds are almost similar to the high spin states. In such cases, the quadrupole splitting can be considered to distinguish between the states in addition to the isomer values.

#### 2.2.3.2 Second Order Doppler Shift

Some Mössbauer experiments require on-line temperature measurements (*in-situ*). In such cases there is bound to be second order Doppler shift of the isomer shift, which results from the thermal agitation or motion of the Mössbauer atom. This effect will contribute to a shift in the energy, as the emitting or absorbing atoms vibrate with thermal fluctuations with frequencies of about $10^{12}$ Hz .The observed isomer shift is given by

$$\delta_{IS} = \delta_C + \delta_{SOD} \tag{2.17}$$

where $\delta_C$ is the centre shift, and $\delta_{SOD}$ refers to the second order Doppler shift. This is a temperature-dependent effect on the center shift of a Mössbauer spectrum, which may seem too fast to influence the Mössbauer event. The second order Doppler shift arises due to relativistic second order contribution to the Doppler effect, resulting in a change in energy of the emitted gamma rays given by

$$\frac{\partial E}{E} = -\frac{E_\gamma}{2c^2}\left\langle v^2 \right\rangle \tag{2.18}$$

where $E_\gamma$ is the energy of the $\gamma$-ray emitted by the Mössbauer nucleus, $\langle v^2 \rangle$ the mean square velocity of the emitting nucleus, and $c$ the velocity of light. The Debye model approximates the shift in the energy levels as a result of the Doppler shift; this can be written as

$$\delta_{SOD} = -\frac{3}{2}\frac{k_B\theta_D}{mc}\left[\frac{3}{8} + 3\left(\frac{T}{\theta_D}\right)^4 \cdot \int_0^{\frac{\theta_D}{T}} \frac{x^3}{e^x - 1} dx\right]. \quad (2.19)$$

#### 2.2.3.3 Electric quadrupole interaction: Quadrupole Splitting

Nuclei with an angular momentum quantum number of $I > ½$ have a non-spherical charge distribution which gives rise to the quadrupole moment [52]. This nuclear quadrupole moment interacts with the gradient of the asymmetric electric field that arises from other charges in the crystal resulting in the splitting of the nuclear energy levels. The change in the energy of a level due to the quadrupole interaction may be expressed by:

$$\Delta E_Q = E_Q(\pm 3/2) - E_Q(\pm 1/2) = eQV_{zz}/2 \quad (2.20)$$

where ±3/2 and ±1/2 are the excited and ground states respectively. This interaction results in a splitting of energy levels of a nucleus that is proportional to $m^2$, where $m$ is the magnetic quantum number of the level. The quadrupole interaction leads to a splitting of a nuclear transition from a single peak into two peaks. The separation between the two peaks reflects the characteristics of the electric field at the nucleus. The distance between the two resonant lines corresponds to the energy difference $\Delta E_Q$ called the quadrupole splitting and is shown in Figure 2.9.

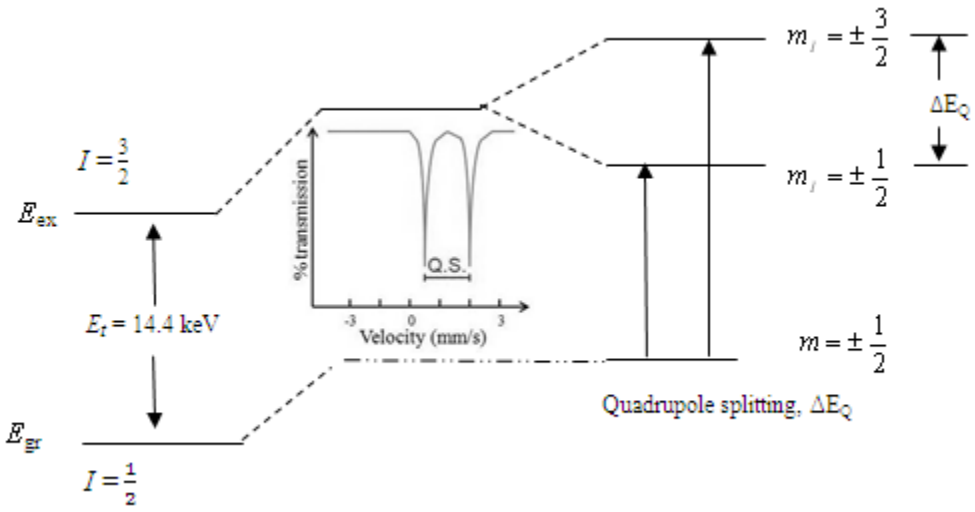


**Figure 2.9: Quadrupole splitting shown by the difference in transition energy between the two states.**

The quadrupole splitting observed in a particular system therefore reflects the symmetry of the bonding environment and the local structure in the vicinity of the Mössbauer atom. Information such as electronic population of various orbitals, isomerisation phenomena, ligand structure, semiconductor properties, and defect structure of solids can thus be obtained by comparing quadrupole splitting data obtained from the materials under study. The quadrupole splitting behaves differently with increasing temperature which is a result of the second order Doppler shift, due to the contribution of [46]

$$V_{ZZ} = V_{ZZ(lattice)} + V_{ZZ(valency)} \tag{2.21}$$

where $V_{ZZ(lattice)}$ is the lattice ligand contribution, and $V_{ZZ(valency)}$ the valence electron contribution. A correction factor [53] for the quadrupole splitting can be expressed as

$$\Delta E_Q = \Delta E_{Q,0}\left(1 - \left(\frac{T}{T_K}\right)^{\frac{3}{2}}\right). \tag{2.22}$$

### 2.2.3.4 Magnetic Hyperfine interaction

The magnetic splitting is a result of the interaction between the nucleus and any surrounding magnetic field. Typically, it splits a single Mössbauer peak into six non-degenerate peaks as shown in Figure 2.10. The nuclear Zeeman splitting is usually measured as the distance between the outermost of these six peaks [50].

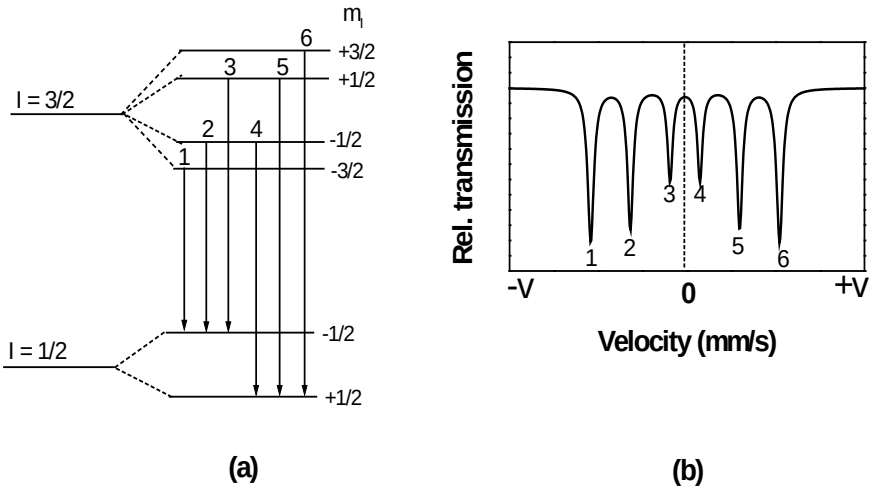


**Figure 2.10: Magnetic splitting of excited and ground state for Nuclear Zeeman, and the transitions (a), and the resulting spectra.**

The Zeeman splitting is especially important in Mössbauer spectroscopy for iron-containing compounds, which are either ferromagnetic or anti-ferromagnetic resulting in strong internal magnetic fields. The spectral line splitting is directly proportional to the magnetic field at the nucleus, and in cases where both the quadrupole splitting and hyperfine splitting occurs, the spectrum will still consist of six peaks, although the peak positions will shift depending on the relative amounts of each type of splitting. The linewidths of the resulting spectra are equal, although their intensities are different. From the transmission spectra, the type of magnetic ordering in a material, the nature of the magnetic interaction as well as the size of magnetic moment on the atoms can be determined.

## 2.3 Magnetism

### 2.3.1 Ferromagnetism

In physics, several different types of magnetism exist. Ferromagnetism is the basic mechanism by which certain materials (such as Fe) form permanent magnets, or are attracted to magnets. Ferromagnetic materials exhibit long-range ordering phenomenon at the atomic level which causes the unpaired electron spins to line up parallel with each other in a domain. According to electromagnetism theory, two nearby magnetic dipoles tend to align in opposite directions, so their magnetic fields will oppose one another as shown in Figure 2.11.

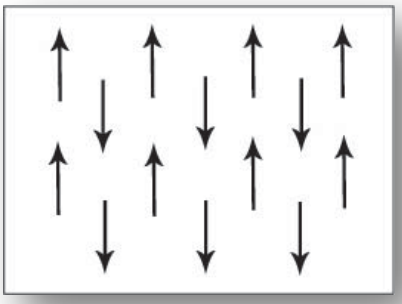

**Figure 2.11: Alignment of fields in a ferromagnetic material.**

Ferromagnetic materials will respond mechanically to an induced magnetic field, which changes slightly towards the direction of the applied field. In a ferromagnet, magnetic moments of equal magnitude arrange themselves parallel to each other. In a ferrimagnet, the moments are unequal in magnitude and order in an antiparallel arrangement. When the moments are equal in magnitude and ordering occurs at the Néel temperature in an antiparallel array to give zero net magnetization, the phenomenon is referred to as anti-ferromagnetism. These transitions from disorder to order represent classic examples of phase transitions [54].

In a few materials, a much stronger interaction between spins arises because the change in the direction of the spin leads to a change in electrostatic repulsion between

neighboring electrons because of a quantum mechanical effect called the exchange interaction. The Pauli exclusion principle states that two electrons with the same spin cannot have the same position, therefore under certain conditions, when the orbitals of unpaired outer valence electrons from adjacent atoms overlap, the distribution of their electric charge in space is further apart when the electrons have parallel spins than when they have opposite spins [55]. This reduces the electrostatic energy of the electrons when their spins are parallel compared to their energy when the spins are anti-parallel, so the parallel-spin state is more stable. In other words, the electrons, which repel one another, can move further apart by aligning the spins of these electrons. For a given ferromagnetic material, the long range order abruptly disappears at a certain critical temperature which is the Curie temperature for the material. Table 2.2 shows different Curie temperatures for different materials.

**Table 2.2: The Curie temperatures for selected crystalline ferromagnetic materials** [56]**.**

| Material | Curie temp.(K) |
|---|---|
| Co | 1388 |
| Fe | 1043 |
| MnBi | 630 |
| Ni | 627 |
| MnSb | 587 |
| Dy | 88 |
| EuO | 69 |

Ferromagnetic materials can retain their magnetization when the external field is removed, as long as the temperature is below the Curie temperature. These materials are characterized by a large positive magnetic susceptibility. Examples of ferromagnetic substances include iron, nickel, cobalt and some of the rare earth elements like Holmium (Ho), Gadolinium (Gd) and Dysprosium (Dy).

### 2.3.2 Paramagnetism

Paramagnetism is caused by the presence of at least one unpaired electron orbital in atoms, molecules, or ions of the paramagnetic material, which results in these particles having a dipole moment. An applied magnetic field tends to align these dipoles in such a way that for a small field and high temperatures the induced field is proportional to the applied field. The magnetization is in the same direction as the applied field. Paramagnets unlike ferromagnets do not retain any magnetization in the absence of an externally applied magnetic field, because thermal motion causes the spins to become randomly oriented in the absence of an external field as shown in Figure 2.12.

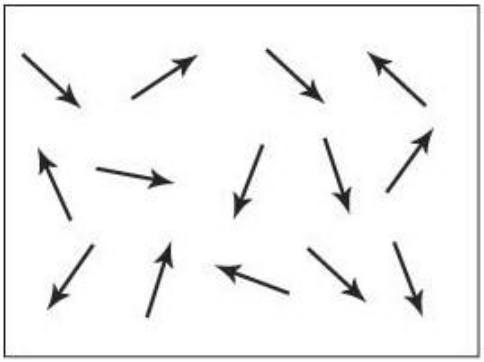

**Figure 2.12: Ordering of magnetic moments in a paramagnetic material.**

When the applied field is removed the total magnetization will thus drop to zero. Even in the presence of the field there is only a small induced magnetization because only a small fraction of the spins will be oriented by the field. Atoms or molecules of paramagnetic materials have permanent dipole magnetic moments, even in the absence of an applied field which usually occurs due to the spin of the unpaired electrons. When a magnetic field is applied, the dipoles will tend to align with the applied field, resulting in a net magnetic moment in the direction of the applied field.

A typical temperature versus susceptibility graph showing the relationship between ferromagnetic and paramagnetic materials is given in Figure 2.13. Well defined Curie and Néel points are shown in the figure. In Table 2.3 a summary of magnetic properties of selected minerals is shown.

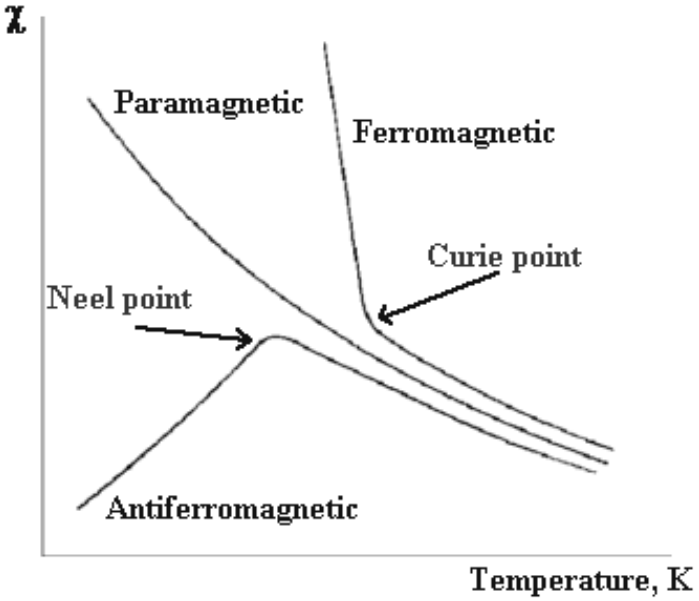


**Figure 2.13: Graphical representation of paramagnetic, ferromagnetic and antiferromagnetic transitions [57].**

**Table 2.3: Magnetic properties of selected materials, where FM is ferromagnetic order, AFM is antiferromagnetic order, $T_c$ is Curie temperature, $\sigma_s$ is the saturation magnetization at room-temperature [57].**

| Mineral | Composition | Magnetic Order | $T_c$ (°C) | $\sigma_s$ (Am$^2$/kg) |
|---|---|---|---|---|
| **Oxides** | | | | |
| Magnetite | $Fe_3O_4$ | ferrimagnetic | 575-585 | 90-92 |
| Ulvospinel | $Fe_2TiO_2$ | AFM | -153 | |
| Hematite | $\alpha$-$Fe_2O_3$ | canted AFM | 675 | 0.4 |
| Ilmenite | $FeTiO_2$ | AFM | -233 | |
| Maghemite | $\gamma$–$Fe_2O_3$ | ferrimagnetic | ~600 | ~80 |
| **Metals & Alloys** | | | | |
| Iron | Fe | FM | 770 | |
| Nickel | Ni | FM | 358 | 55 |
| Cobalt | Co | FM | 1131 | 161 |
| Awaruite | $Ni_3Fe$ | FM | 62 | 120 |

### 2.3.3 Relaxation phenomenon in Mössbauer spectra

The environment of a Mössbauer nucleus can change within its lifetime resulting in a change of the frequency $\omega_o$ of the Mössbauer radiation. Such a phenomenon is called relaxation and it occurs when the hyperfine interactions undergo time dependent fluctuations, which changes the environment of the Mössbauer nucleus. There are two timescales which are involved, namely the lifetime of the nuclear excited state and the Larmor precession time [50] [58] of the nuclear spin. These timescales are usually determined by the nature of the Mössbauer isotope and the interaction being studied, i.e. the mean lifetime of the Mössbauer excited state $\tau_N$ and the Larmor precession time $\tau_L$.

The static magnetic hyperfine splitting is usually observed when $\tau_L$ is smaller than $\tau_N$, which is the slow relaxation limit, $\tau_L >> \tau_N$. The lines start to broaden for relaxation times of the order of the mean life time of the excited nuclear state [59] as shown in Figure 2.14. In the simple case of longitudinal relaxation with a magnetic hyperfine field that can assume only two values + ~$B_{hf}$ and – ~$B_{hf}$, it can be seen that the spectra consists of sextets with narrow lines for spin states of $S_z = +\frac{1}{2}$ and $S_z = -\frac{1}{2}$.

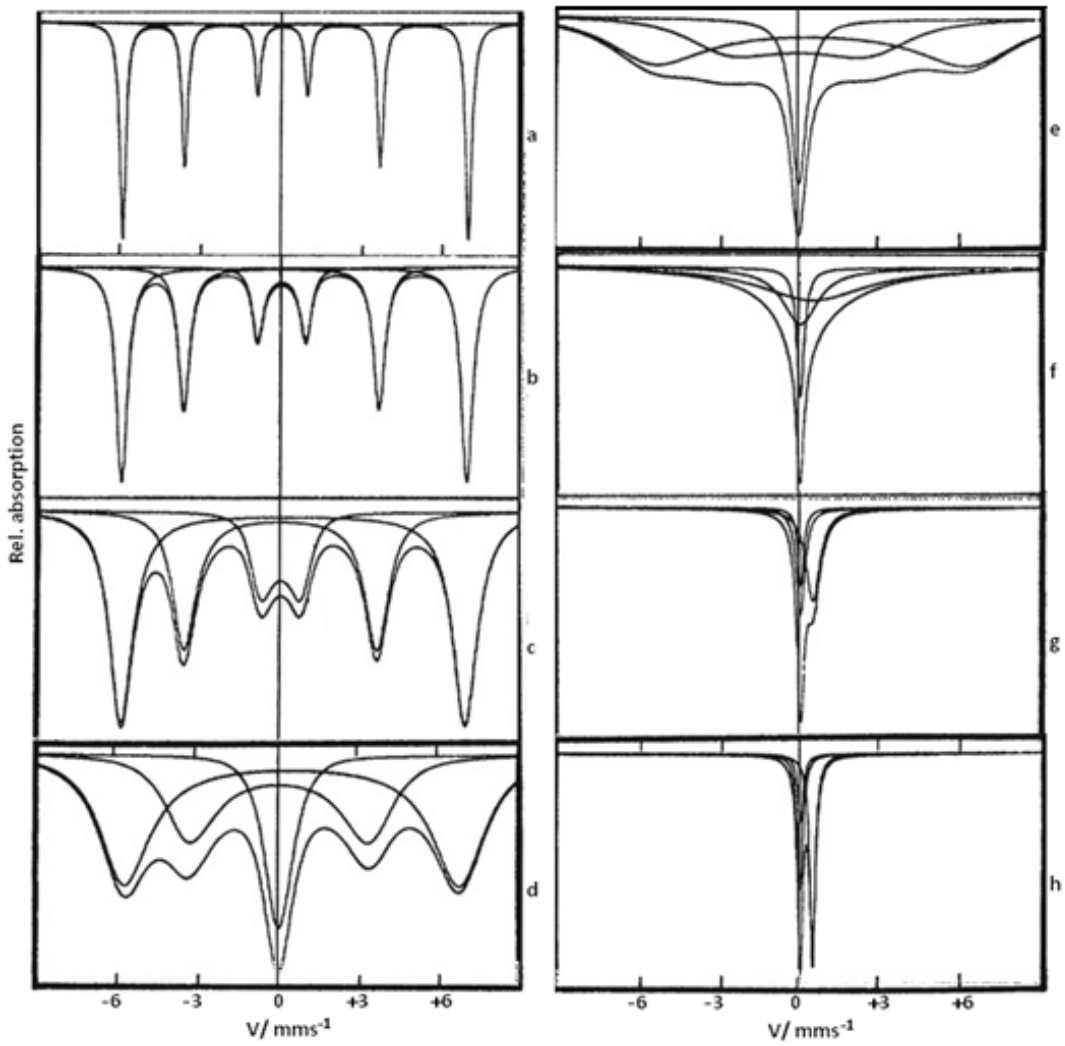


**Figure 2.14: Theoretical $^{57}$Fe Mössbauer relaxation spectra for longitudinal relaxation with the indicated relaxation times [59].**

For the condition $\tau_L \sim \tau_N$, it is observed that individual lines become broader (Figure 2.14d, e, f), and the spectra cannot only be described by six Lorentzian lines, which exhibits a natural broadening linewidth of $^{57}$Fe of approximately $10^{-9}$ eV.

For the case where $\tau_L << \tau_N$, which is fast relaxation time, the magnetic splitting collapses to zero (Figure 3.7h), for $S_z = 0$. It should be noted however that there be more factors other than $\tau_L << \tau_N$ and $\tau_L >> \tau_N$ for fast or slow relaxation times, the system should include the entire lifetime of the excited nuclear state, which would

include the nuclear spin-spin relaxation, super-paramagnetism, cross relaxation, electronic spin-lattice relaxation and other factors as shown in Figure 2.15.

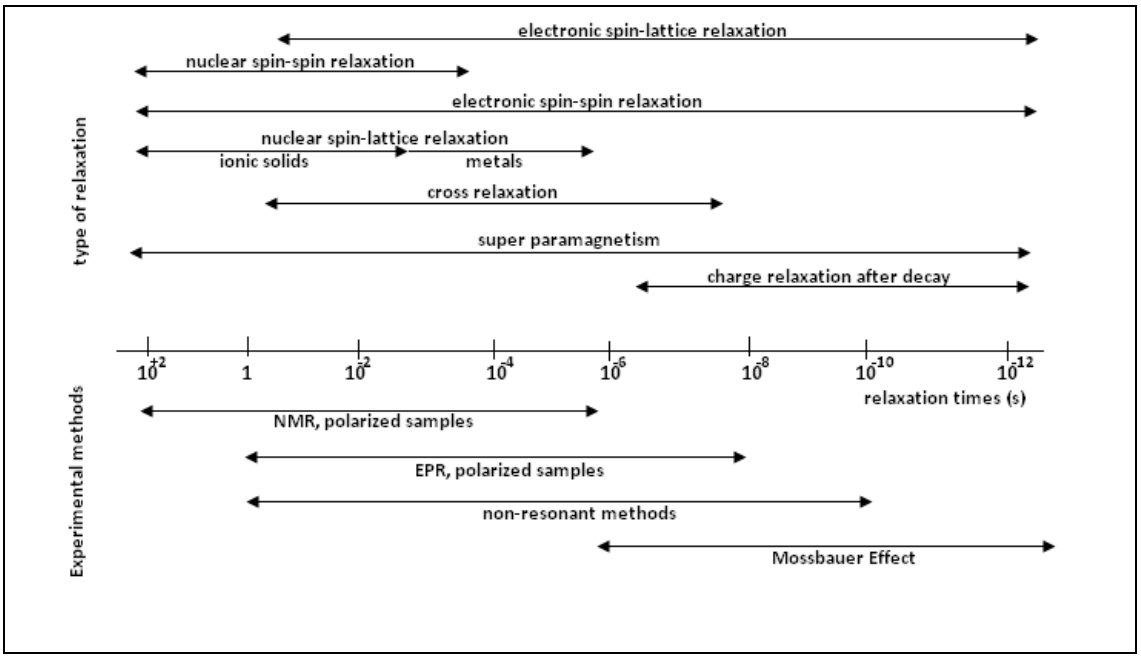


**Figure 2.15: Typical relaxation times in solids [59].**

# CHAPTER 3: EXPERIMENTAL DETAILS

Mössbauer spectroscopy remains the "gold standard" for quantitative determination of the valence state of iron in minerals and identification of various iron oxides. This is a very useful spectroscopic method which complements the more established techniques such as Nuclear Magnetic Resonance (NMR), Electronic Spin Resonance (ESR) and X-ray diffraction [60]. Mössbauer Spectroscopy can provide quantitative information as well as qualitative information about the material under study, for example phase analysis, chemical bonds, valence, magnetism, lattice distortions, impurities, defects and atomic jumps. This chapter focuses on the synthesis and preparation of the Ho doped $BiFeO_3$ sample that was used in the X-ray diffraction and Mössbauer measurements followed by an overview of the associated instrumentation used in the Mössbauer experiments. A brief description of the data acquisition systems and data analysis routines is also included in this chapter. The chapter also highlights the principles of the X-ray diffraction measuring technique which has been applied as a structural characterization tool for the identification of the chemical composition of the material under study.

## 3.1 Sample synthesis

Holmium doped $BiFeO_3$ (BFO) bulk ceramics were synthesized by the solid state reaction method by collaborators from India, at the Institute of Material Science, Acharya Vihar [42]. Highly pure (99.999 %) $Bi_2O_3$, $Ho_2O_3$ and $Fe_2O_3$ powders were mixed with appropriate compositions to form $Bi_{1.05}Ho_{0.05}FeO_3$ and heated at 500 $^oC$ for six hours, and then subsequently quenched to room temperature for immediate grinding in a convectional agate mortar and pestle. The same procedure was repeated five times in order to achieve a homogeneous mixture with a smaller particle size. Respective compositions of powders were palletized using freshly prepared Poly Vinyl Alcohol (PVA) as a binder.

Cylindrical pellets of dimensions 13 mm diameter and 2 mm thickness were prepared by a non-evacuated hydraulic press under a pressure of 10 ton/cm$^2$. The pressed pellets were then slowly heated (50$^o$C/hour) to 200$^o$C and maintained for 4 hours to release the PVA binder from the pellets using a high temperature programmable controller (EuroTherm 2204) vacuum furnace. The sintering schedule of the pellets was carried out @ 50$^o$C/hour heating rate with constant soaking periods of 4 hours at 200$^o$C and 600$^o$C. This soaking period was required to remove any volatile impurity/organic materials (binder) from the pellets until the samples were finally sintered at 850$^o$C for 24 hours [42].

## 3.2 Sample preparation for Mössbauer measurements

In Mössbauer spectroscopy it is important to prepare a sample that has the correct thickness and is texture free for optimal absorption to occur. Materials that are free of Fe can be used as extenders, such as sugar or milk powder. The following principles need to be considered for the specific mass and thickness of the sample:

1. If the sample is too thick with resonant nuclei, appreciable line broadening is observed in the spectra. A rule of thumb is to use 5 – 10 mg/cm$^2$ of natural Fe in a sample per resonant line. The natural abundance of Fe is 2.17%, which corresponds to 0.7 mg/cm$^2$ of natural Fe. A mineral containing 10 wt. % of Fe should have 7 mg of $^{57}$Fe per cm$^2$. Thus for a single resonance line we would need approximately 5 mg/cm$^2$ of Fe [61].
2. If the sample is too thick with non-resonant nuclei, then the electronic absorption will reduce the count rate to unacceptable low levels. The attenuation of the $\gamma$-radiation by the absorber may be obtained from the transmission function $\frac{I}{I_o} = \exp(-\mu_e \rho x)$, where $I_o$ is the incident radiation and $I$ is the intensity of the admitted radiation, $\mu_e$ is the mass absorption coefficient (cm$^2$/g) for the 14.4 keV $\gamma$-radiation, $\rho$ is the density and $x$ is the

thickness dimension of the sample in centimeters. A computed value of 30% - 40% is always considered adequate.

To circumvent texture, single crystal absorbers or randomly oriented small crystals in a powder are used. A $Bi_{1.05}Ho_{0.05}FeO_3$ pellet was crushed using a pestle and mortar in acetone to powder to avoid oxidation and to spread uniformly across a sample holder. The sample holder is shown in Figure 3.1.

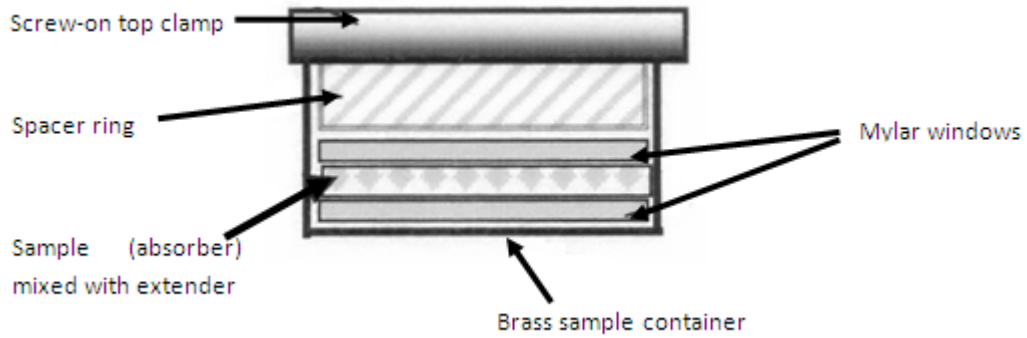


**Figure 3.1: Sample holder made of brass (diameter Φ = 1.7 cm) used to load powdered samples. The holder was used for room temperature $^{57}$Fe Mössbauer measurements.**

Hearne *et al.* [62], deduced a principal factor that determines the effective absorber thickness $t_a$ which is given by:

$$t_a = \frac{N_o d_a}{A \times 10^3} \sigma_o f_a a \tag{3.1}$$

where $N_o$ is the Avogadro's number, $d_a$ being the absorber's thickness, $A$ is the mass number, and $f_a$ is the recoil-free fraction of the absorber. It should be noted that $\frac{N_o d_a}{A \times 10^3}$ is the number of the Mössbauer atoms per unit area. From equation (3.1), small resonant intensities can be achieved when $t_a$ is taken be less than unity, though line distortions will occur with an increase of $t_a$.

The absorber thickness is however an issue that needs to be considered, as the $^{57}$Fe absorption spectra cannot be collected in reasonable time without using an amount of absorber which does not cause considerable thickness effects [63]. One can get a quantitative analysis of when and how thickness effects of the absorber are important and to what extent the area ratios can be different from the population ratios. For a single Lorentzian line centered at $E_o$, a single line absorber with intrinsic resonance absorption cross-section can be given by

$$\sigma_a(E) = \frac{\sigma_o \dfrac{\Gamma^2}{4}}{(E - E_o)^2 + \dfrac{\Gamma^2}{4}} \tag{3.2}$$

where $\sigma_o$ is the cross-section at resonance given by

$$\sigma_o = \frac{\lambda^2}{2\pi} \frac{2I^* + 1}{2I + 1} \frac{1}{1 + \alpha} \tag{3.3}$$

where $\lambda$ being the wavelength of the Mössbauer $\gamma$-ray, $I^*$ and $I$ is the nuclear spin states of the excited and ground states, respectively and $\alpha$ is the conversion coefficient of the transition.

## 3.3 Mössbauer Instrumentation

The conventional Mössbauer experimental arrangement consists of a radiation source, an absorber, a detector (gas proportional counter), as well as the drive electronics necessary to produce the relative motion between the absorber (sample) and the source. The source is mounted on a vibrator, which moves back and forth at a certain velocity which results in a Doppler shift of the energy of the recoilless $\gamma$-ray in accordance with the equation

$$E_\gamma = E_o\left(1+\frac{v}{c}\right) \tag{3.4}$$

where $v$ is taken to be positive when the source is moving towards the absorber (hence increasing $\gamma$-ray radiation) and negative when moving away (hence decreasing $\gamma$-ray radiation). A typical transmission Mössbauer setup is shown in Figure 3.2. This arrangement allows for a well defined $E_o$ to be scanned over an energy range that includes the splitting and shift of the nuclear energy levels of the absorber [47].

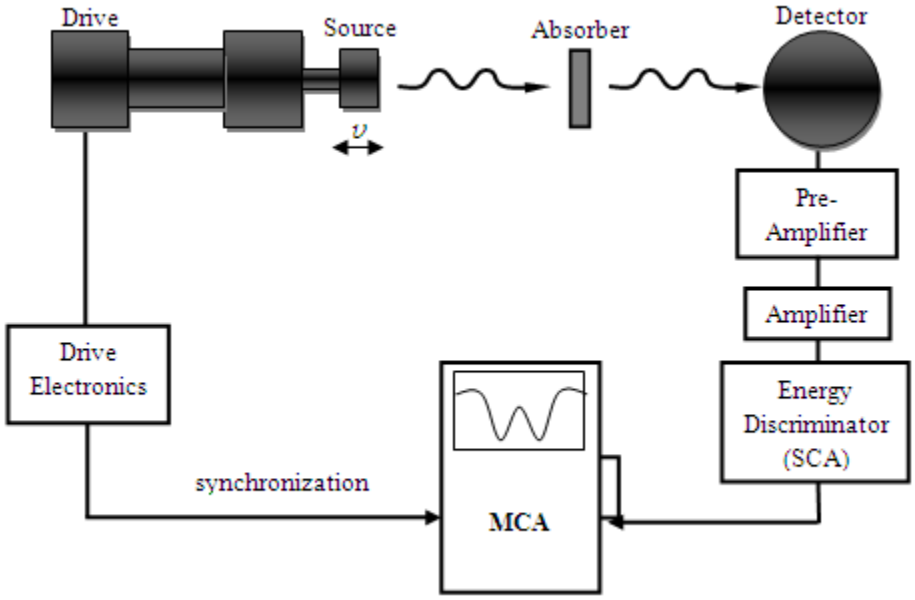


**Figure 3.2: A typical transmission Mössbauer setup.**

The $\gamma$-ray photon strikes the counter at different energies and only the 14.4 keV photon is absorbed by $^{57}$Fe. A single channel analyzer (SCA) is used to eliminate most of the background radiation and X-rays. The charge pulse from the counter is then amplified and differentiated by the preamplifier, and further amplified before it is fed into the Multi-Channel Analyzer (MCA). In the MCA, the charge pulse is counted with the address corresponding with the Doppler velocity ***v*** given by the corresponding number in the clock counter.

There are two operational modes for the data acquisition system, namely the Pulse Height Analysis mode (PHA) and the Multichannel Scaling Mode (MCS). In the PHA mode, the incoming pulses are sorted into bins depending on their pulse height, which is proportional to the energy of the gamma or X-ray which is absorbed in the proportional detector, with the energy channels shown in Figure 3.3.

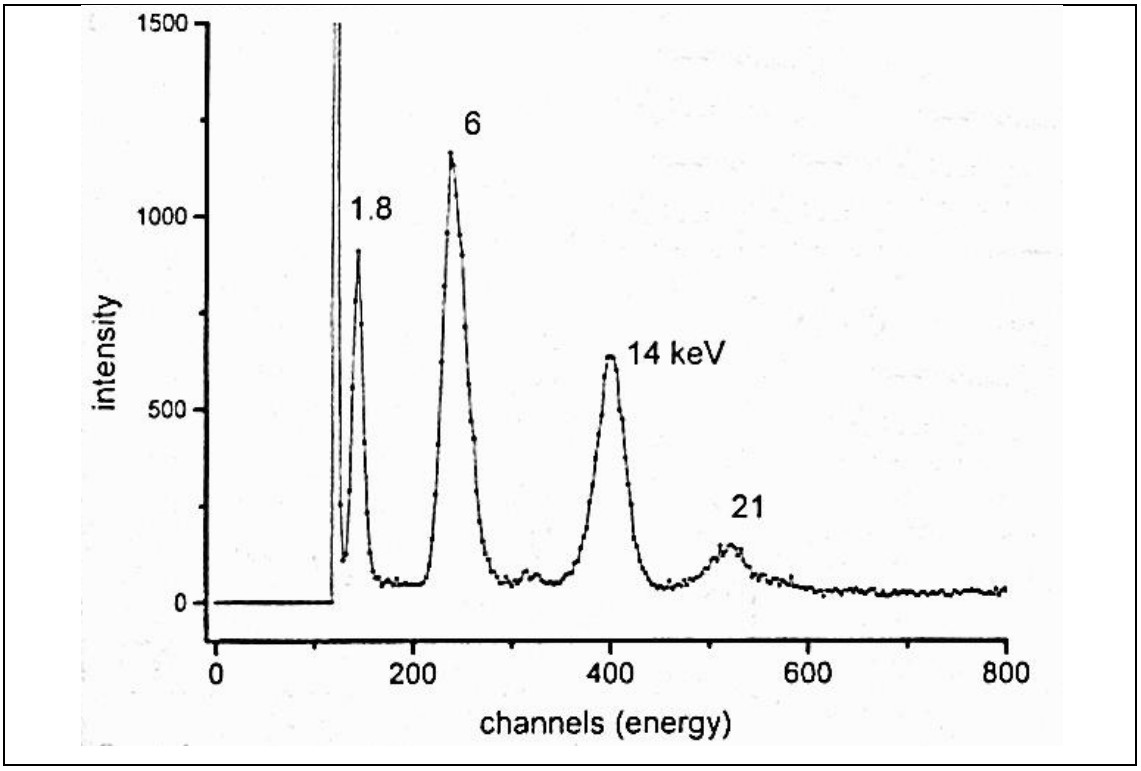


**Figure 3.3: Pulse height spectrum with discriminator windows open showing the complete energy spectrum from the $^{57}$Co source.**

The ratio of the 14.4 keV $\gamma$-ray to 21 keV X-ray is measured, and typically a ratio of 3:1 is ideal. After measuring the ratios, the 21 keV X-ray is then removed by appropriately changing the lower level discriminator (LLD) and the upper level discriminator (ULD) windows. The count rate of the 14.4 keV $\gamma$-rays is measured and thereafter the mode is changed to MCS for data acquisition. In order to obtain nuclear resonance absorption, the sample to be investigated must be irradiated with gamma radiation, which results upon the transition of the 14.4 keV nuclear level of $^{57}$Fe which occurs as a result of the decay of $^{57}$Co to $^{57}$Fe [64].

The gas proportional counter contains krypton (Kr) plus a small amount of methane quench gas. One method for quenching discharges is to add a small amount (~10%) of an organic gas, such as methane, in the chamber. The quenching gas molecules have a weaker affinity for electrons than the chamber gas does; therefore, the ionized atoms of the chamber gas readily acquire electrons from the quenching gas molecules. Thus, the ionized molecules of the quenching gas reach the chamber wall instead of the chamber gas. These molecules are neutralized by gaining electrons, and the energy liberated does not cause further ionization, but causes dissociation of the molecule. This dissociation quenches multiple discharges, and the quenching gas molecules are eventually consumed, thus limiting the lifetime of the proportional counter [65]. A $\gamma$-ray photon incident through the Beryllium (Be) window of the detector ionizes some of the Kr atoms, creating ion-electron pairs. This will cause the positive ions to drift towards the outer walls and hence electrons are attracted towards the centre wire. The accelerating electron causes an avalanche effect, which is the ionization of more atoms, thus increasing the effective gas gain. The rise time of the signal pulse is then caused by the shortened travel time to the center wire by the suppression of the random electron motion by the methane gas.

### 3.3.1 The Mössbauer Spectrometer at the University of Witwatersrand (WITS)

The Mössbauer spectrometer at WITS is set up as shown in Figure 3.4. This particular layout was used for room temperature measurements. In this setup (Figure 3.4) typical distances of 10 cm between the source and absorber was utilized and a distance of 5 cm was used between the absorber and detector.

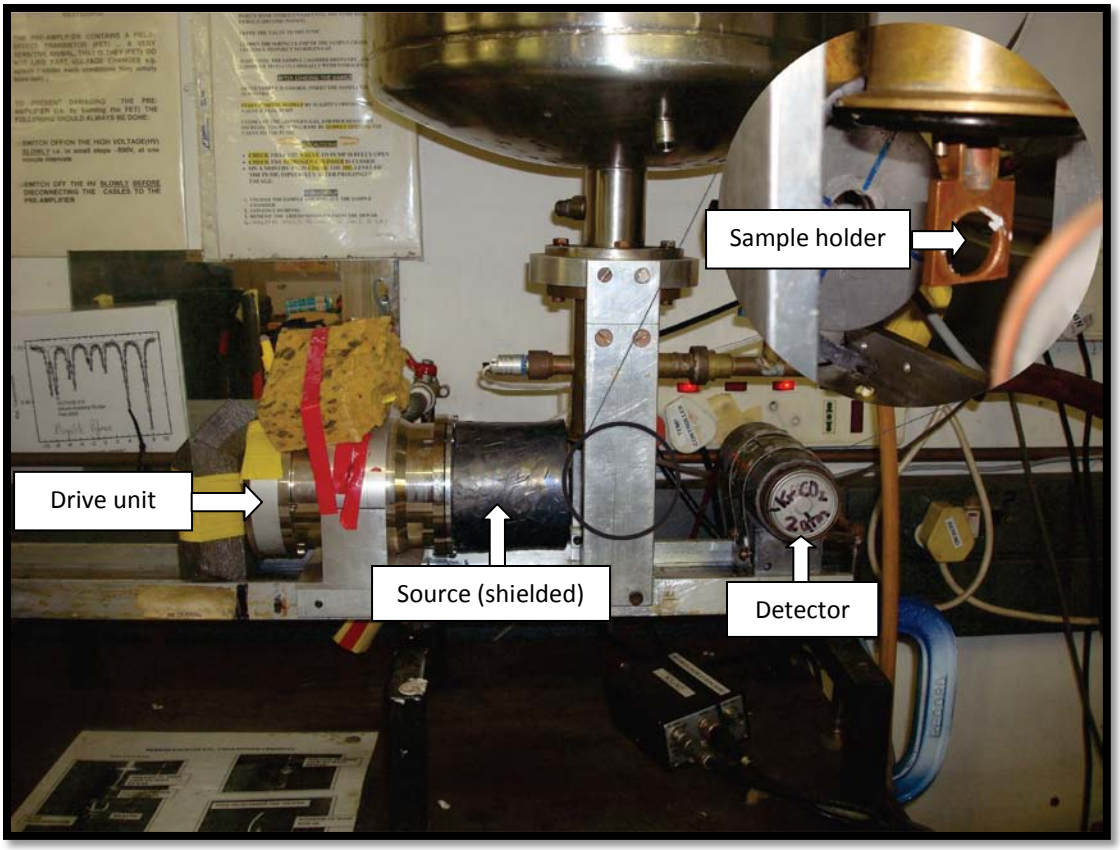


**Figure 3.4: The layout of the Mössbauer instrumentation at WITS University.**

The appropriate distances required to optimize the acquisition time can be determined by the activity, absorber characteristics, effective thickness and diameter of the absorber [66]. A $^{57}$Co (Rh) source with an activity of 50 mCi was utilized and the setup above was used to achieve maximum absorption area, and alignment through the absorber has to be optimal to obtain appreciable count rates, and to avoid any geometrical effects such as baseline drift. The Mössbauer spectra were recorded in a horizontal transmission mode, with the velocity waveform generated by an analyzer version controller card (PCA II). A spectrum was collected in 1024 channels, which was later transformed to 512 channels during the data analysis procedures. A typical room temperature spectrum was collected continuously for a period of up to 2 days with a background of 4 million counts. The BHFO samples were annealed between 373 K and 1073 K using a lab built furnace and in Argon gas. All Mössbauer measurements were then conducted at room temperature.

### 3.3.2 *In-situ* measurements

The magnetic properties of certain ferromagnetic materials cannot be fully appreciated at room temperature as the Curie or Néel temperature of the Mössbauer absorber can be considerably above or below room temperature. The need to monitor such temperatures is necessary hence the need for *in-situ* measuring systems becomes important.

The horizontal transmission arrangement for the *in-situ* setup was set to the MCS mode with the velocity waveform also generated by the analyzer version controller card, which was set to a dwell time of 100 μs per channel. The spectrum was collected in 1024 channels, with a mirror image in 512 channels, and adjacent channels added together for optimal analysis purposes as it reduces statistical scattering. The *in-situ* measurements were conducted with the Mössbauer furnace MBF-100 as shown in Figure 3.5, which can be operated to a temperature of 1173 K. The associated electronics is similar to that described in section 3.4.

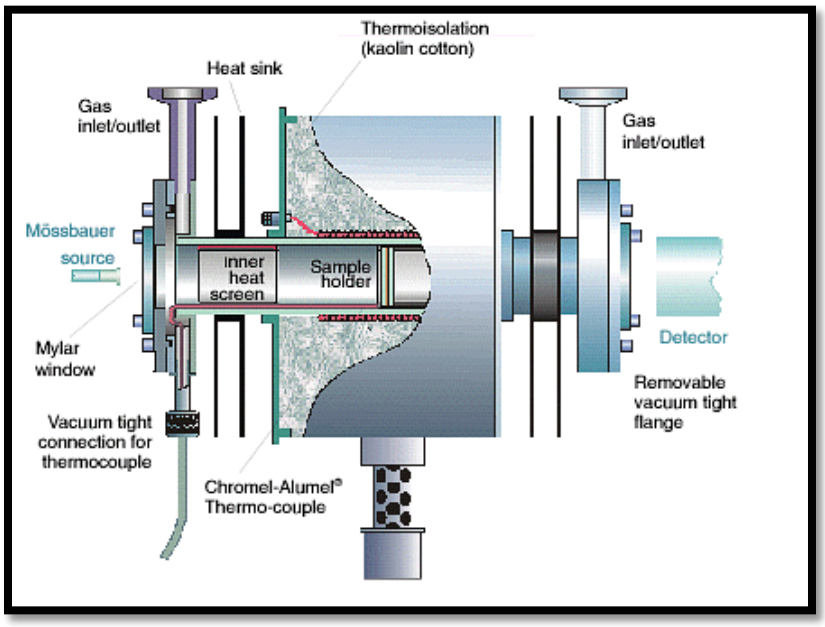


**Figure 3.5: The MBF-1100 Mössbauer Furnace for *in-situ* measurements [67].**

The furnace is designed to anneal in air, vacuum or any gas of choice. The sample is sandwiched inside a boron nitrite holder of thickness 0.8 mm with internal and external diameter of 13 mm and 16.9 mm, respectively, with 5% absorption of $\gamma$-radiation. A Mylar foil in this furnace allows for the absorption of the 14.4 keV $\gamma$-radiation of $^{57}$Co to be less than 5% hence allowing for better data acquisition.

The temperature controller TR-55 supplies a constant voltage to the furnace and has a temperature stability of 0.08 $^{o}$C/$^{o}$C at 50 ppm/$^{o}$C process. The actual arrangement for the *in-situ* system is illustrated in Figure 3.6, with the temperature controller shown in the inset.

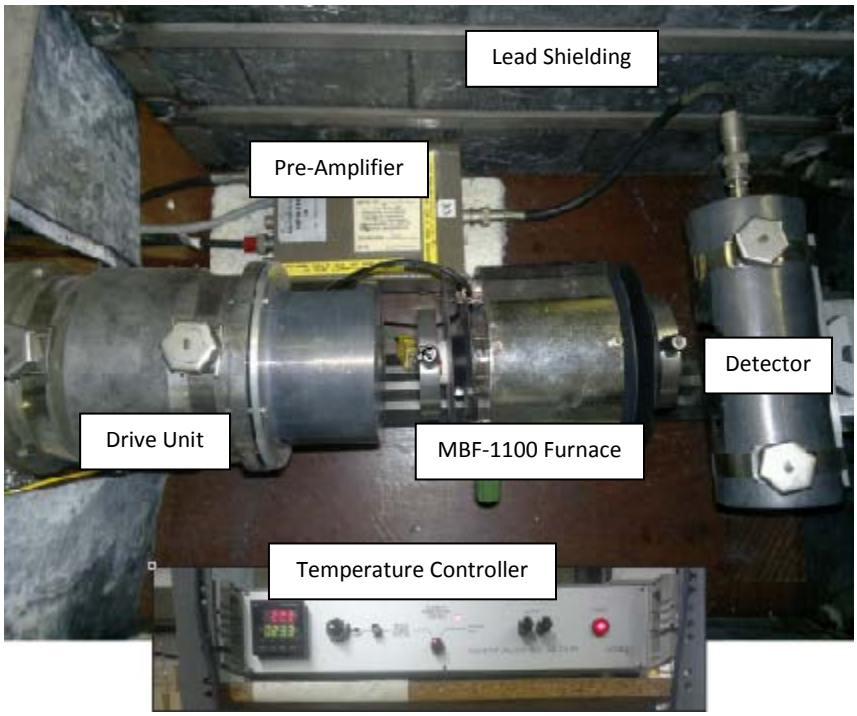


**Figure 3.6: Top view of the *in-situ* Mössbauer setup at WITS University.**

### 3.3.3 Calibration of Mössbauer Spectra

A typical Mössbauer spectra of $\alpha$-Fe is shown in Figure 3.7 which is a mirror image of the spectra and has 1024 channels. In order to reduce statistical noise the 1024 channels need to be reduced to 256 channels, which is achieved by folding the

spectra and adding the adjacent channels as shown in Figure 3.7. A 12 $\mu$m Fe foil, which is approximately 99.98% pure, was used for calibration purposes and a minimum of 3000 counts per channel was sufficient for calibration. A simple sextet from the $\alpha$-Fe foil was used to fit the calibration file with a theoretical magnetic field $B_{hf}$ of 32.9 T to 33.1 T, an isomer shift and quadrupole shift of zero.

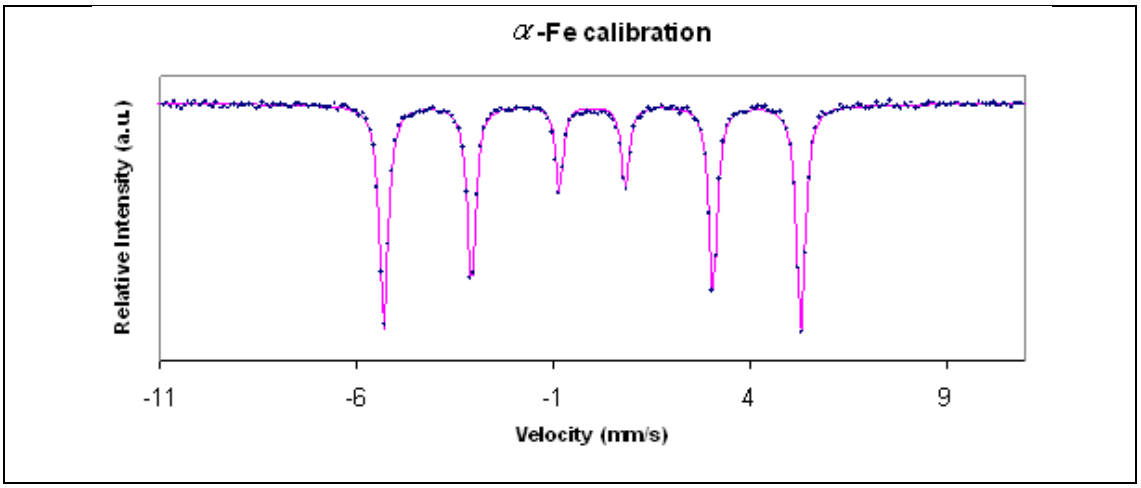


**Figure 3.7: Folded and fitted spectrum for $\alpha$-Fe.**

### 3.3.4 Mössbauer spectral analysis

The assumption that the absorber produces spectra which is the sum of Lorentzian line shapes can be described by the Breit-Wigner formula given in equation (2.4) which simplifies the fitting of spectra, by using non-linear least square techniques. The minimum value of the linewidth is given by the Heisenberg's uncertainty principle:

$$\Gamma = \frac{(\hbar \ln 2)}{T_{½}} \tag{3.5}$$

where $T_{½}$ is the half-life of the excited state of the isotope.

The sextets, which are magnetically split usually has identical pairs, linewidths and intensities have their energy positions determined by the hyperfine magnetic field,

the isomer shift as well as the quadrupole spitting. Similarly, the doublets are also assumed to have the same intensity as well as the linewidth, and this is always at Full Width Half Maximum (FWHM). All Mössbauer spectra analysis in this project was done with program Vinda, which is essentially a toolbox of macros in Microsoft excel from a Visual Basic Application that was developed by Professor Haraldur Páll Gunnlaugsson [68] of the University of Aarhus, Denmark. A summary of the fitting process used in Vinda is described in Appendix A.

## 3.4 X-ray diffraction data acquisition system

The room temperature XRD data were collected using a Bruker D2 Phaser desktop diffractometer shown in Figure 3.8 with the insert showing how a sample is loaded. The Bruker D2 Phaser employs a sealed tube Cu X-ray source and is equipped with a Bruker Lynxeye PSD detector using 2.5° primary and secondary beam radial Soller slits which has a high performance signal to noise ratio and a secondary beam Ni filter. The specific details for the diffractometer are listed in Table 3.1.

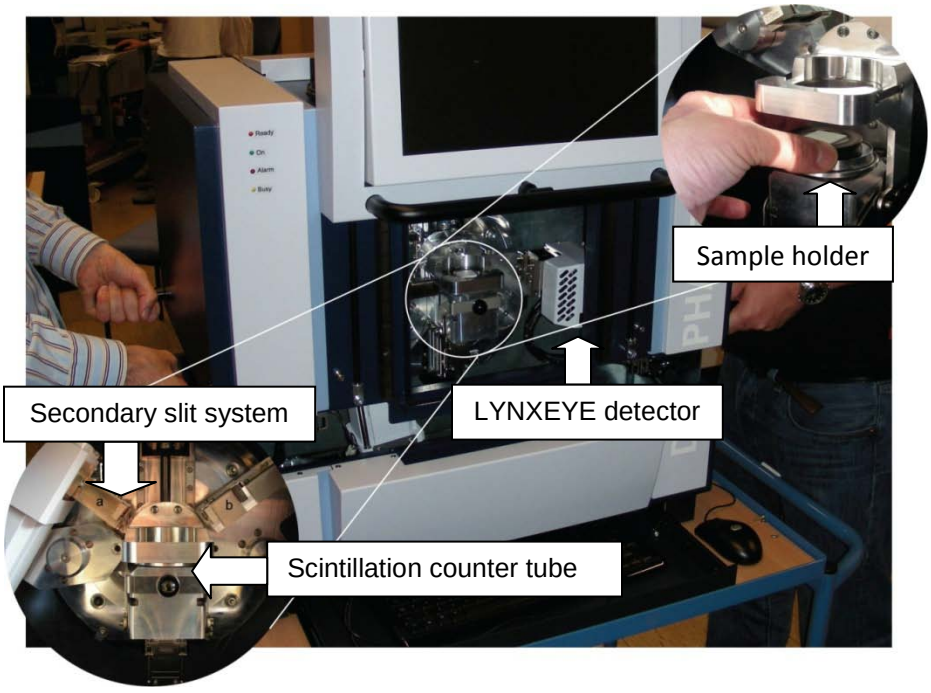


**Figure 3.8: D2 Phaser desktop diffractometer, with the insert showing how the sample is loaded.**

**Table 3.1: The Bruker D2 Phaser settings.**

| | Parameter | Value |
|---|---|---|
| **Collection mode** | Bragg/Brentano Transmission | |
| **Goniometer radii** | Primary radius (mm) | 70.7 |
| | Secondary radius (mm) | 70.7 |
| **Detector** | 2theta angular range ($^{o}$) | 5 |
| **Slits** | Primary Soller slit ($^{o}$) | 2.5 |
| | Secondary Soller slit ($^{o}$) | 2.5 |
| **X-ray Generator** | Cu radiation – Voltage | 30 kV |
| | Cu radiation – Current | 10 mA |

All samples were loaded by pressing on a zero background silicon single crystal disk supported in a polymer circular sample holder. The thickness of the powder samples should be ideally large enough to prevent the beam from passing through to the substrate below. The generally accepted reduction of the beam intensity is approximately one thousandth ($1/1000^{th}$) of the initial beam intensity. The data from the spectrometers is analyzed using the DIFFRAC PLUS EVA software which is ideal for 2- and 3-dimensional data analysis as well as presentations. It allows for peak searching, data smoothing using Fourier filtering, *Kα2*-stripping using the Rachinger method, and background subtraction. This analysis can offer information such as phase matching as well as particle size analysis.

EVA is a comprehensive and extremely versatile graphics program for easy, fast and convenient 2- and 3-dimensional data evaluation and presentation. A complete collection of the best algorithms for powder diffraction data is provided including a unique Real-Time-Preview of all evaluations using the "ghost"-function, and calculation of profile parameters such as line position, center of gravity, integrated area and half width is possible. The software allows for a 3-dimensional presentation of waterfall plots, iso-intensity plots, and true 3D plots.

A match for the XRD peaks is found from the database of known compounds which could be either experimental findings or calculated patterns. Many powder diffraction data sets collected from inorganic as well as organic compounds have been compiled

into a database by the Joint Committee on Powder Diffraction Standards (JCPDS), and over 50 000 patterns can be used to identify unknown materials through the patterns. Visual inspection from the matches is what usually determines the perfect peak matching, as the software can only identify compounds which have been searched. A typical finger printing is shown below in Figure 3.9.

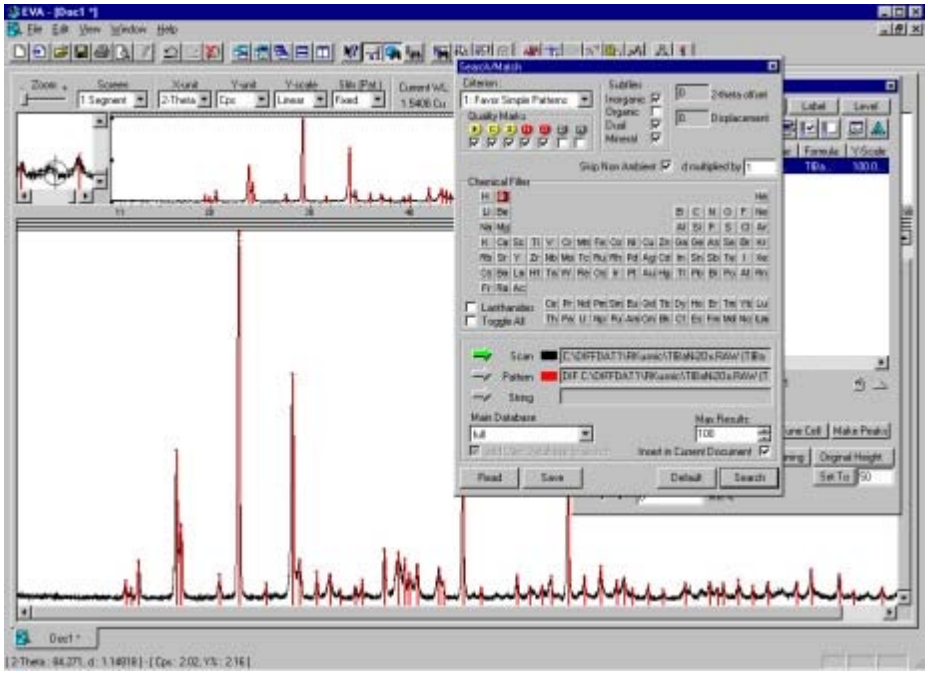

**Figure 3.9: A typical Diffrac PLUS EVA pattern fitting.**

The smoothing of the pattern might be necessary to reduce the noise from background contributions which can arise from continuous radiation, or detector noise. Smoothing will increase the signal to noise ratio, but should be applied when necessary as some peaks may be overlapping which can be destroyed by smoothing.

# CHAPTER 4: RESULTS AND DISCUSSION

This chapter focuses on the analysis and interpretation of data obtained from X-ray diffraction (XRD) and Mössbauer spectroscopy measurements conducted on Ho substituted $BiFeO_3$ (BHFO). The first section of the chapter presents results from X-ray diffraction and Mössbauer measurements on the as-synthesized and annealed BHFO samples with special attention given to the derived hyperfine parameters. The final section of this chapter presents the results obtained from *in-situ* Mössbauer measurements on the BHFO sample.

## 4.1 X-ray Diffraction Measurements

XRD measurements were made at room temperature on the as-synthesized BHFO sample and after annealing in Argon up to 1073 K. These measurements were performed using a Bruker D2 Phaser desktop diffractometer. The diffractometer employs a sealed tube Cu $K_\alpha$ X-ray source and equipped with a Bruker Lynxeye PSD detector using 2.5° primary and secondary beam radial Soller slits. The BHFO sample was loaded by pressing on a zero background silicon single crystal disk supported in a polymer circular sample holder. The XRD patterns for BHFO were obtained in the $2\theta$ range ($10^\circ$ - $90^\circ$) at scan steps of $0.020^\circ$ $min^{-1}$, for a total period of 189 seconds.

### 4.1.1 X-ray Diffraction Spectra

A series of XRD spectra obtained at room temperature for the as-synthesized BHFO and annealed samples are presented in Figure 4.1. The well known room temperature phase of BFO is rhombohedral [42] with an *R*3*c* space group. Our results on BHFO showed the *R*3m phase, with lattice parameters of $a_{rh}$ = 3.962 Å, with a rhombohedral angle of $\alpha_{rh}$ = 89.4°. These parameters are obtained through EVA software from the database of known compounds which could be either experimental findings or

calculated patterns. This phase is dominant in all measured spectra as shown in Figure 4.1.

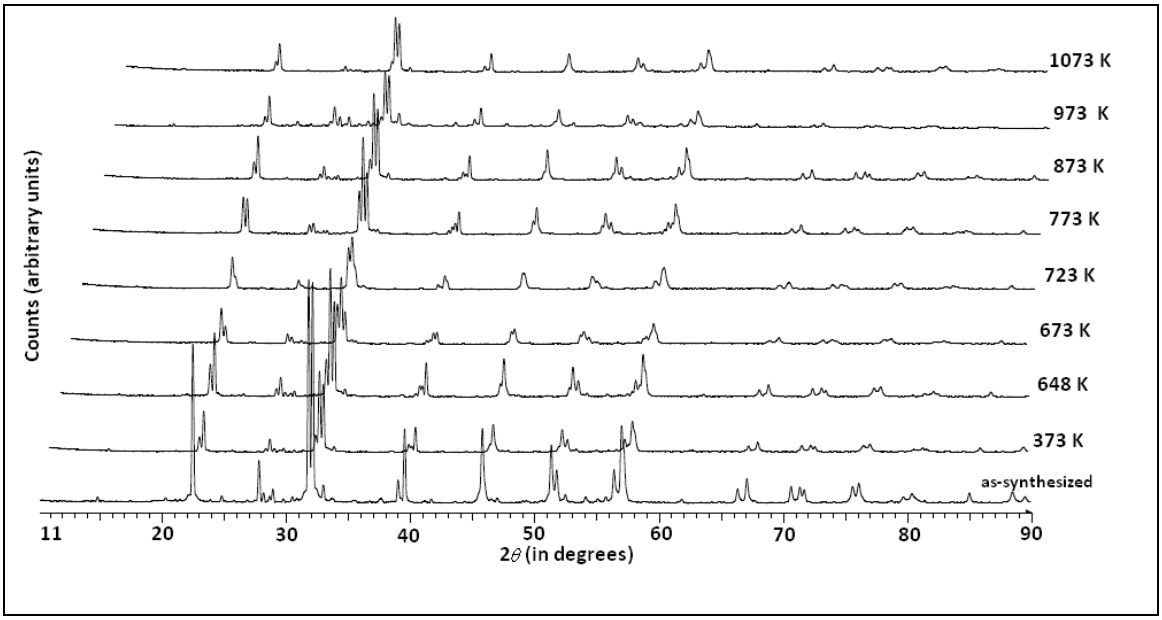


**Figure 4.1: Room temperature X-ray diffraction spectra of BHFO obtained from measurements on the as-synthesized sample and annealed samples (temperatures indicated). The spectra at higher temperatures have been slightly displaced in order to illustrate the variation of the line intensities with annealing temperature.**

### 4.1.2 Assignment of diffraction peaks

The XRD pattern shown in Figure 4.1 reflect contributions from the rhombohedral impurity phase of BFO, a majority $Bi_{25}FeO_{90}$ phase and a minority $Bi_2Fe_4O_9$ phase [12], which has been proposed to be a consequence of the local stoichometry fluctuations in BFO [69]. After annealing between 673 - 873 K, a new dominant component is evident from the finger printing process (as seen later in Figure 4.3) and is assigned to the B-site of $Fe_3O_4$ according to the Joint Committee on Powder Diffraction Standards (JCPDS) file 19-629, and the Inorganic Crystal Structure Database (ICSD) 044525. This site has been reported to have a cubic inverse spinel structure [70]. The evaporation of Bi and strain related effects have been observed to produce Bi-deficient secondary phases which tend to compensate for the

local chemical composition imbalance and structural distortion [71] [72] hence such a phase is present.

In our case, the major impurity phase $Bi_{25}FeO_{90}$ has been determined through the finger printing process using the Bruker DiffracPLUS EVA software. Such a phase has been identified by other researchers [42] [69] [73]. According to the JCPDS file 72-1832, the $Bi_{25}FeO_{40}$ phase is body-centered cubic with lattice parameters, $a = b = c = 10.18120$ Å, and $\alpha = \beta = \gamma = 90^{\circ}$. In Figures 4.2 and 4.3 we present the analysis of the XRD spectral lines using the multiphase "fingerprint" process for the as-synthesized sample and the annealed sample at 723 K, respectively.

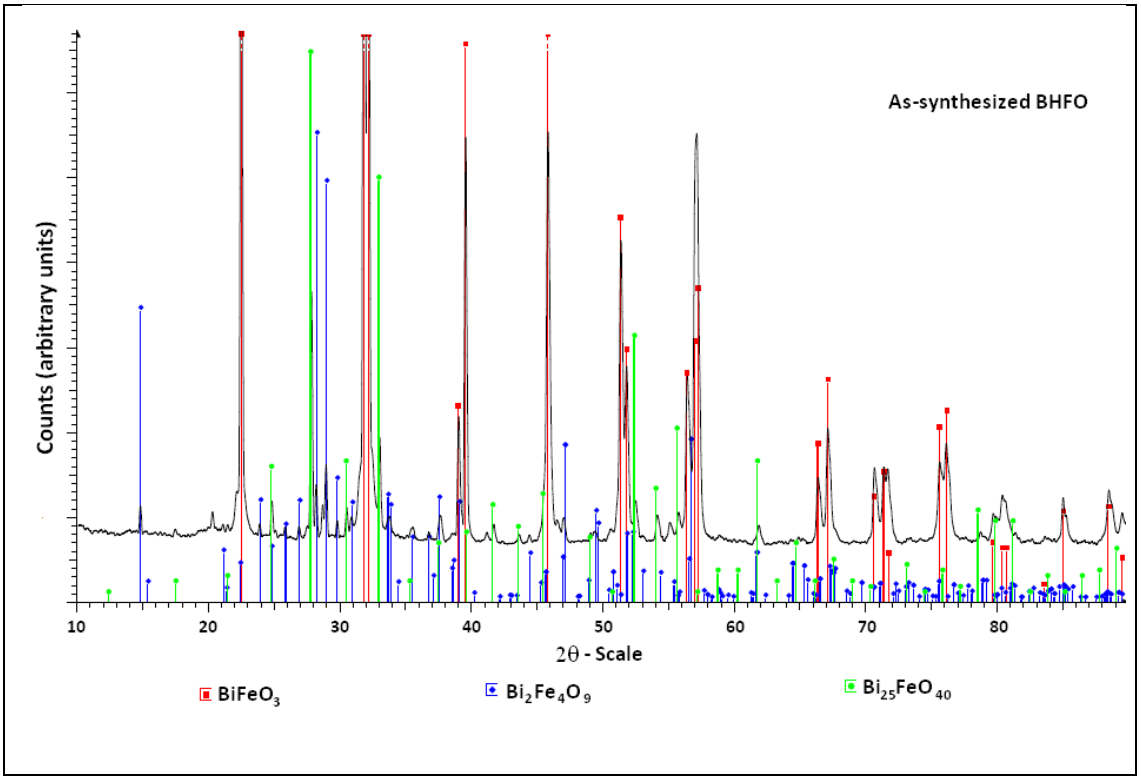


**Figure 4.2: The fingerprint of the different phases for the as-synthesized BHFO sample measured at room temperature. The red lines correspond to the $BiFeO_3$ phase, the blue lines to $Bi_2Fe_4O_9$ and the green lines to $Bi_{25}FeO_{40}$.**

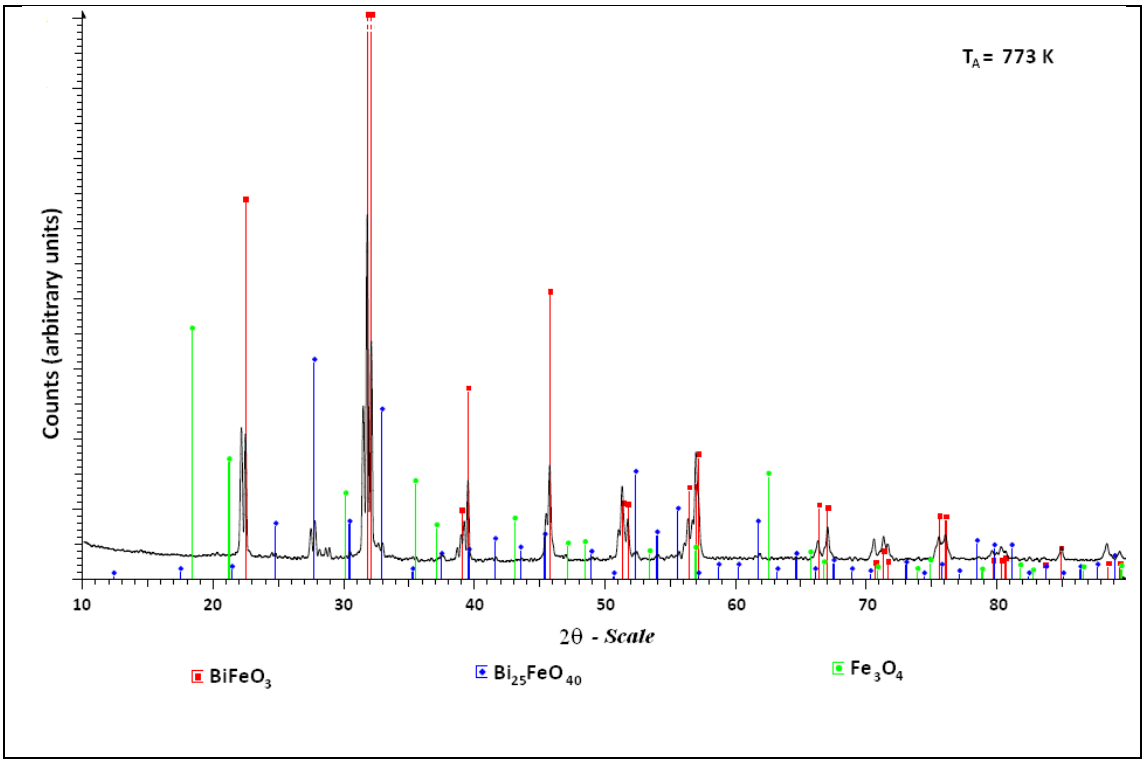


**Figure 4.3: The fingerprint of the different phases of the BHFO sample annealed at 773 K and measured at room temperature. The red lines correspond to $BiFeO_3$ phase, the blue lines to $Bi_{25}FeO_{40}$ and the green lines to $Fe_3O_4$.**

## 4.2 Mössbauer measurements conducted at room temperature on the as-synthesized and annealed samples

The as-synthesized BHFO pellet was fine ground to powder using a pestle and mortar and annealed as described in section 4.1. Mössbauer measurements were then conducted at room temperature on the as-synthesized sample and after annealing the sample between 300 - 873 K. A standard transmission spectrometer fitted with a Wissel drive unit MR-260A operating at constant velocity, and a $^{57}Co$ source of about 50 mCi were utilized in the measurements. The spectra were analyzed in a simultaneous fit using the spreadsheet based code Vinda. A detailed description of Vinda is given in Appendix A.

### 4.2.1 Mössbauer spectra and fitting procedures

Figure 4.4 displays selected Mössbauer spectra obtained at room temperature for the as-synthesized Ho substituted $BiFeO_3$ (BHFO) and annealed samples. The spectra exhibits broadened features due to the hyperfine distributions related to the local variations of the neigbourhood of Fe. The magnetic hyperfine splitting patterns are indicative of magnetic ordering mostly probably screwed or slightly antiferromagnetic ordering.

The spectra show asymmetry which is associated with the inhomogeneous line broadenings and can be accounted for by the spiral magnetic structure of BFO. The differential broadening of the spectral lines with respect to the experimental linewidth can be explained in terms of the presence of different non-equivalent Fe sites in the crystal structure. Any discernable misfits to the data are attributed to statistics and the fact that Bi has a very high absorption coefficient for 14.4 keV Mössbauer gamma-rays. Best fits were obtained using a Lorentzian model developed by D.G. Rancourt [74] with Voigt lineshape. The spectra were fitted with the following spectral components:

(i) Two symmetric sextets (S1 & S2) with identical pairs, which are present in the spectra for the as-synthesized and all annealed samples.
(ii) A symmetric sextet (S3) with identical pairs which is observable at $T_A \geq 673$ K.
(iii) One simple Lorentzian doublet (D) with different line intensities, which is present in all spectra.
(iv) A single line (SL) which is present in all spectra.

The room temperature (RT) spectrum for the as-synthesized BHFO sample is characterized by two sextets (S1 & S2), a doublet (D) and a single line (SL) as shown in Figure 4.4, with TA representing the temperature at which the sample was annealed.

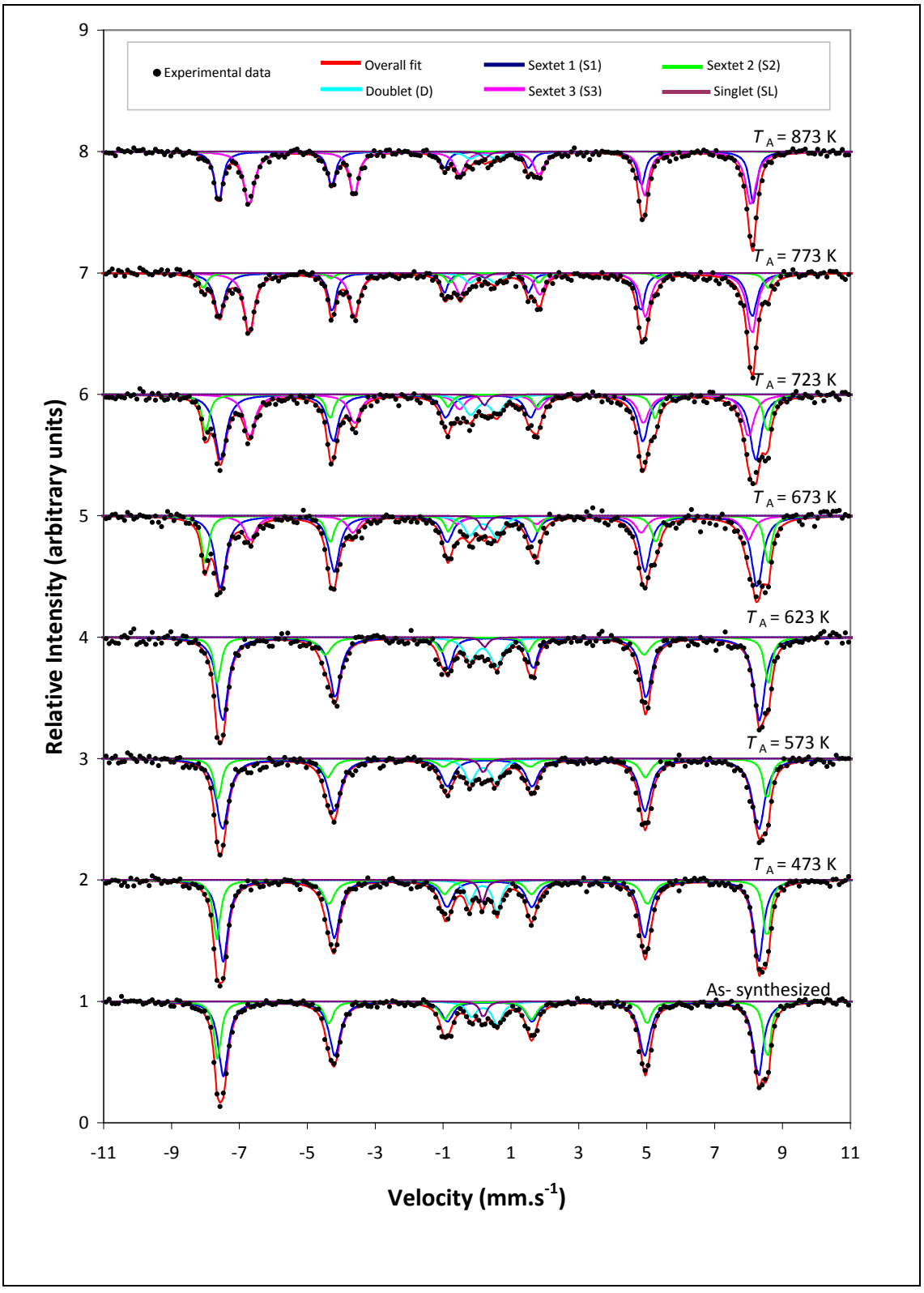


**Figure 4.4: Selected Mössbauer spectra for as-synthesized BHFO and annealed samples.**

The two sextets S1 and S2 indicate a magnetically ordered state, with Zeeman parameters 48.81 T and 50.14 T, isomer shift values of 0.39 $mm.s^{-1}$ and 0.39 $mm.s^{-1}$ and quadrupole split values of 0.03 $mm.s^{-1}$ and 0.13 $mm.s^{-1}$, respectively as shown in Table 4.1. At $T_A \geq 673$ K, a third sextet (S3) is observable in the spectra. A single line (SL) and doublet (D) is present in all spectra. A summary of the hyperfine parameters for all spectral components is given in Table 4.1. Details of the estimated errors can be found in Appendix B.

**Table 4.1: Hyperfine parameters obtained at room temperature for the as-synthesized BHFO and annealed samples (AN = annealed).**

| Annealing Temperature | SEXTET (S1) | | | SEXTET (S2) | | |
|---|---|---|---|---|---|---|
| $T_A$ (K) | $B_{hf}$ (T) | $\delta$ ($mm.s^{-1}$) | $\Delta E_Q$ ($mm.s^{-1}$) | $B_{hf}$ (T) | $\delta$ ($mm.s^{-1}$) | $\Delta E_Q$ ($mm.s^{-1}$) |
| As-synthesized | 48.81(3) | 0.39(1) | 0.03(2) | 50.14(3) | 0.39(1) | 0.13(1) |
| 473 (AN1) | 48.85(4) | 0.39(1) | 0.04(1) | 50.19(4) | 0.39(1) | 0.11(2) |
| 573 (AN2) | 48.92(6) | 0.39(1) | 0.02(1) | 50.09(5) | 0.37(2) | 0.18(3) |
| 623 (AN3) | 48.98(5) | 0.41(0) | 0.01(1) | 50.24(6) | 0.35(1) | 0.24(3) |
| 673 (AN4) | 48.97(6) | 0.36(1) | -0.02(1) | 51.33(5) | 0.38(1) | -0.19(2) |
| 723 (AN5) | 48.81(4) | 0.33(1) | 0.00(1) | 51.23(4) | 0.37(1) | -0.18(1) |
| 773 (AN6) | 48.62(6) | 0.27(1) | -0.03(1) | 51.50(7) | 0.38(1) | -0.25(3) |
| 873 (AN7) | 48.77(5) | 0.27(1) | -0.02(1) | 51.58(9) | 0.38(7) | -0.26(9) |

| Annealing Temperature | SEXTET (S3) | | | DOUBLET (D) | | SINGLET (SL) |
|---|---|---|---|---|---|---|
| $T_A$ (K) | $B_{hf}$ (T) | $\delta$ ($mm.s^{-1}$) | $\Delta E_Q$ ($mm.s^{-1}$) | $\delta$ ($mm.s^{-1}$) | $\Delta E_Q$ ($mm.s^{-1}$) | $\delta$ ($mm.s^{-1}$) |
| As-synthesized | - | - | - | 0.22(1) | 0.76(3) | 0.19(2) |
| 473 (AN1) | - | - | - | 0.18(1) | 0.82(2) | 0.17(3) |
| 573 (AN2) | - | - | - | 0.18(2) | 0.76(3) | 0.18(6) |
| 623 (AN3) | - | - | - | 0.19(2) | 0.78(4) | 0.23(2) |
| 673 (AN4) | 45.42(8) | 0.62(2) | 0.07(4) | 0.18(7) | 0.79(9) | 0.20(5) |
| 723 (AN5) | 45.52(5) | 0.65(1) | 0.00(2) | 0.19(3) | 0.78(6) | 0.22(5) |
| 773 (AN6) | 45.86(5) | 0.69(1) | 0.02(1) | 0.17(1) | 0.77(4) | 0.24(2) |
| 873 (AN7) | 45.78(5) | 0.67(1) | 0.02(1) | 0.17(4) | 0.76(9) | 0.24(2) |

Nalwa and Garg [14] conducted room Mössbauer measurements on Sm doped BFO samples and their spectra were characterized by a six line pattern with hyperfine parameters of $\delta$ = 0.386 mm.s$^{-1}$, $\Delta E_Q$ = 0.0142 mm.s$^{-1}$, and $B_{hf}$ = 49.51 T. These values are comparable with the parameters deduced for S1 ($\delta$ = 0.39 mm.s$^{-1}$, $\Delta E_Q$ = 0.03 mm.s$^{-1}$, $B_{hf}$ = 48.81 T) and S2 ($\delta$ = 0.39 mm.s$^{-1}$, $\Delta E_Q$ = 0.13 mm.s$^{-1}$, $B_{hf}$ = 50.14 T) from our measurements. Khomchenko *et al.* [12] also performed room temperature Mössbauer measurements on Pb doped BFO samples and found two six-line patterns also indicating a magnetically ordered state with values typical of high-spin $Fe^{3+}$ ($B_{hf1}$ = 50 T, $B_{hf2}$ = 46.1 T, $\delta_1$ = 0.394 mm.s$^{-1}$ and $\delta_2$ = 0.484 mm.s$^{-1}$).

### 4.2.2 Annealing behavior of BHFO

Figure 4.5 shows the isomer shift variation with annealing temperature for all spectral components. The isomer shift of S1 is fairly constant up to $T_A$ = 623 K then decreases gradually after the appearance of S3 indicating an increase of the *s*-electron density at the Fe nucleus. The isomer shift of spectral component S2 shows no variation with annealing temperature and a similar trend is observed for S3. For both, the as-synthesized and annealed samples (AN1-AN7), no systematic change in the isomer values for doublet D and singlet SL is evident.

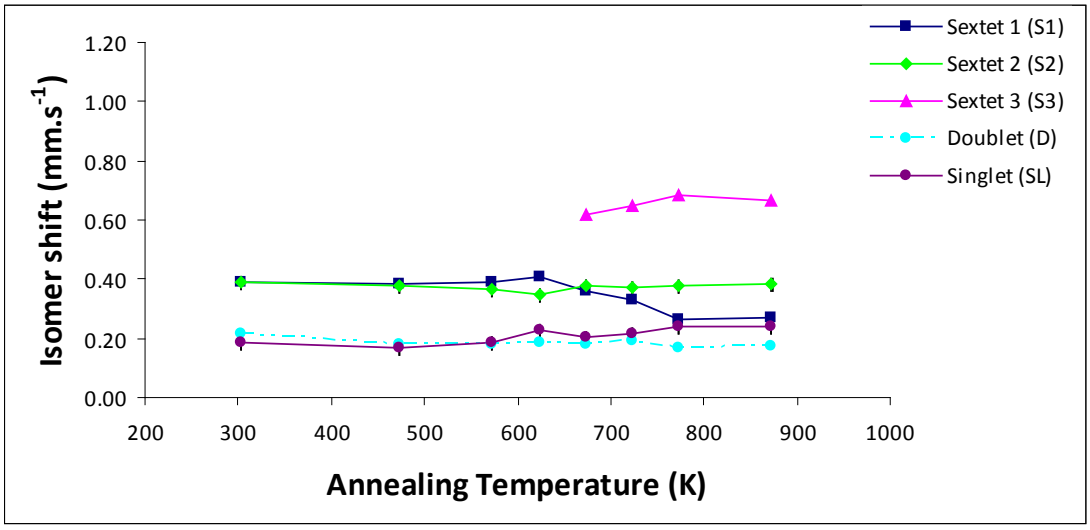


**Figure 4.5: Isomer shift as a function of annealing temperature (K) of the spectral components for the BHFO sample.**

For the as-synthesized and annealed samples AN1-AN7, the quadrupole splitting remains fairly constant for S1 and D. The quadrupole splitting of S3 shows no systematic change with annealing temperature for the annealed samples AN4 - AN7. The quadrupole splitting of S2 remains fairly constant up to $T_A$ = 623 K, then changes quite dramatically to a negative value with a slightly larger magnetic field. The distribution of the isomer shift and the difference in the quadrupole splitting values and signs are due to the variation in the angles between the principal axis of the electric field gradient (EFG) and the spin direction [19]. These observations are illustrated in Figure 4.6.

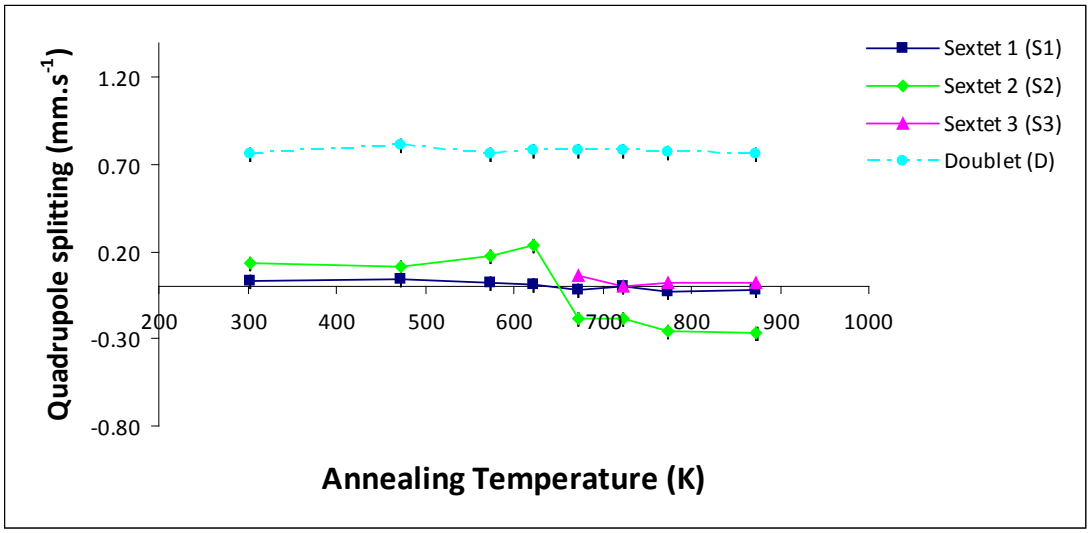


**Figure 4.6: The quadrupole splitting of spectral components as a function of annealing temperature observed in the Mössbauer spectra of BHFO.**

The hyperfine field of S1 ($B_{hf}$ ~ 49 T) remains fairly constant for all measured samples. The hyperfine field of S2 shows no change for the as-synthesized and annealed samples AN1-AN3, however at $T_A$ > 623 K, the hyperfine field ($B_{hf}$ ~ 50 T) of S3 shows a slight increase which could be due to Ho being substituted at the Fe site in $BiFeO_3$. The fluctuating hyperfine field of S2 could be a result of the local magnetic disorder within the crystal. The hyperfine field of S3 ($B_{hf}$ ~ 45 T) remains fairly constant for $T_A$ > 673 K, as shown Figure 4.7. Figure 4.8 shows the intensities

of the spectral components S1, S2, S3, D, and SL for the as-synthesized and annealed BHFO samples versus annealing temperature.

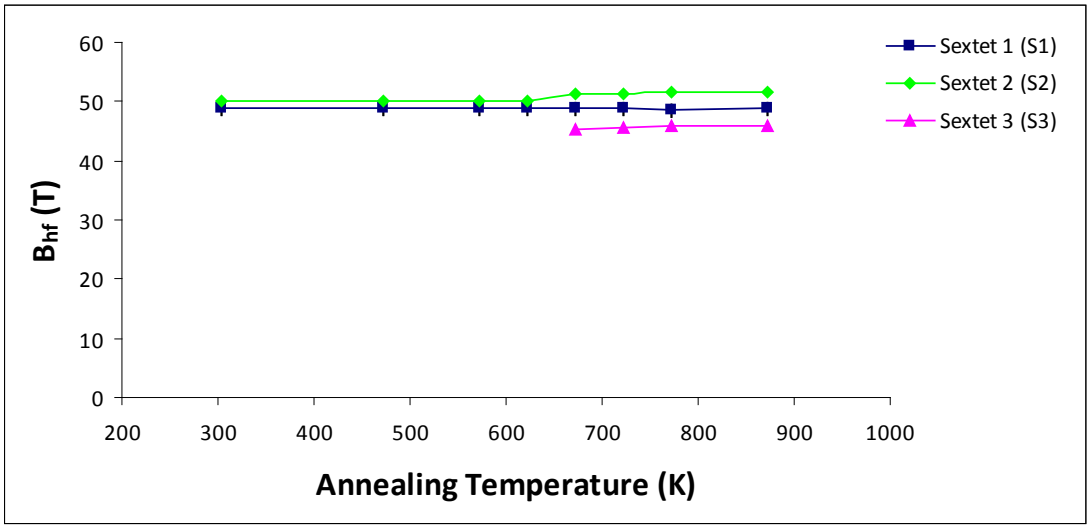


**Figure 4.7: The behavior of the hyperfine magnetic fields as a function of annealing temperature as observed in the Mössbauer spectra for the as-synthesized and annealed BHFO samples.**

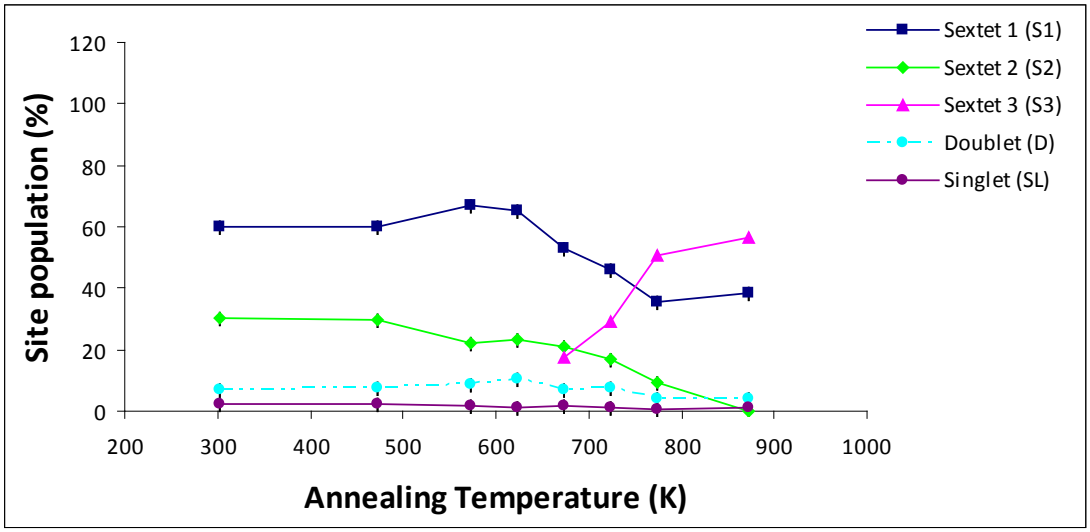


**Figure 4.8: Site population dependence as a function of annealing temperature observed in the Mössbauer spectra for as-synthesized and annealed BHFO samples.**

The area fraction of spectral component S1 decreases gradually from ~ 62% for the as-synthesized BHFO sample to ~ 35% for the sample annealed at $T_A$ = 873 K. For the as-synthesized sample, the spectral component S2 has a site population of ~ 32% population which reduces to 0% for the sample annealed at 873 K. The area fraction of component S3 increases from 17% to 59% for the samples annealed between $T_A$ = 673 K and $T_A$ = 873 K. The area fractions of both D and SL show negligible change in all measured samples.

### 4.2.3 Assignment of spectral components

For the as-synthesized Ho substituted BiFeO3 sample, the extracted hyperfine parameters of sextet S1 ($B_{hf}$ ~ 49 T, $\delta$ = 0.39 ± 0.01 mm.s$^{-1}$ and $\Delta E_Q$ = 0.03 ± 0.02 mm.s$^{-1}$) are consistent with those of rhombohedral $BiFeO_3$ [11] [23] [75]. These values are characteristic of magnetically ordered $Fe^{3+}$ due the presence of hyperfine fields, $B_{hf}$ acting on the nuclear spin. These hyperfine parameters are very similar for the annealed samples AN1-AN3. Some fluctuations in the isomer shift of S1 are observed for the annealed samples AN4-AN7.

The isomer shift and hyperfine magnetic splitting values of S2 ($B_{hf2}$ = 50.1 T, $\delta_2$ = 0.39 mm.s$^{-1}$) are very similar to S1 ($B_{hf1}$ = 48.8 T, $\delta_1$ = 0.39 mm.s$^{-1}$) except that the quadrupole splitting of S2 is much higher. The magnetic pattern of S2 is characteristic of an undoped BFO spectrum and the slightly lower isomer shift value implies Fe is also in the 3+ oxidation state. A possible $Fe^{2+}$ presence from S2 could be contributing to the broadening of the BHFO spectra. For the annealed samples AN4 – AN7, the spectral components of S2 with hyperfine parameters of $\delta$ = 0.37 mm.s$^{-1}$, $\Delta E_Q$ ~ -0.22 mm.s$^{-1}$ and $B_{hf}$ = 51.5 T correspond to $\alpha$–$Fe_2O_3$ [36].

The range of isomer shift values (0.62 - 0.69 mm.s$^{-1}$) and low quadrupole splitting values of 0 to 0.09 mm.s$^{-1}$ for the S3 component extracted from the fits for the annealed samples AN4-AN7 indicates a high symmetry cubic spinel. In this case Fe

is assigned to the non-equivalent B (octahedral) sites [76] of $Fe_3O_4$ corresponding to a mixture of the 2+ and 3+ oxidation states. The hyperfine fields of $Fe^{2+}$ and $Fe^{3+}$ are not appreciably different; therefore the presence of $Fe^{2+}$ could be a contributing factor to the line broadening of S3. From our analysis, the hyperfine field for S3 has been determined to be approximately 46 T.

X-ray diffraction measurements have revealed two secondary non-perovskite phases which have been identified as due to the insufficient reactions between $Bi_2O_3$ and $Fe_2O_3$ powders during the synthesis process [42]. These phases correspond to a majority Bi rich $Bi_{25}FeO_{40}$ phase and a minor $Bi_2Fe_4O_9$ impurity phase [14]. Previous studies of $BiFeO_3$ and doped systems [14] [36] [69] have shown that the origin of the paramagnetic doublet D is attributed to the $Bi_{25}FeO_{40}$ phase and the singlet line SL to the $Bi_2Fe_4O_9$ phase. The broadened doublet D indicates a disordered and amorphized system [77]. The room temperature isomer shift and quadrupole splitting values of the paramagnetic doublet D ($\Delta E_Q$ ~ 0.76 mm.s$^{-1}$, $\delta$ ~ 0.22 mm.s$^{-1}$) and SL, ($\delta$ ~ 0.19 mm.s$^{-1}$) corresponds to Fe with an oxidation state of 3+.

## 4.3 *In-situ* Mössbauer measurements

*In-situ* Mössbauer measurements were conducted on powder BHFO samples held at temperature range of 300 – 748 K using a MBF-1100 Mössbauer furnace with a k-type thermocouple connected to a TR-55 temperature controller. The furnace, through the aluminized Mylar foils and the thin aluminium heat screen foils, offers absorption of the 14.4 keV $\gamma$-rays of less than 5%. The BHFO sample was sandwiched between two $B_4C$ discs with concentric sample holders, which offer minimum additional absorption of about 5%. A measurement time of approximately 4 days was necessary to obtain a BHFO spectrum with acceptable statistics due to increased distance between source-absorber and absorber-detector.

### 4.3.1 Mössbauer spectra and fitting procedures

Best fits were obtained with the following spectral components:

(i) Two symmetric sextets (S1 & S2) with identical pairs, which are present below the Néel temperature ($T_N$).

(ii) One simple Lorentzian doublet (D) with different line intensities, present from 300 K to 748 K.

(iii) A single line (SL) which is present between 300 K and 481 K.

Figure 4.9 shows a series of selected Mössbauer spectra obtained from *in-situ* measurements on Ho doped BFO samples. The room temperature (RT) spectrum has been analyzed with two sextets (S1 & S2), an asymmetric doublet (D) and a single line (SL). The two sextet components (S1 and S2) with hyperfine magnetic fields of 47.99 T and 49.30 T are indicative of a magnetically ordered state which decreases with increasing temperature and finally collapses at $T > 588$ K. The single line (SL) component disappears at similar measuring temperatures. The spectra are then dominated by the paramagnetic doublet D. Table 4.2 presents the hyperfine parameters obtained from Mössbauer measurements at room temperature on BHFO.

### 4.3.2 Annealing behavior

Figure 4.10 presents the temperature dependence of the hyperfine field which exhibits a similar trend as the calculated pattern for $T/T_N < 0.5$ by Blaauw and Van der Woude [11]. In their *in-situ* Mössbauer measurements investigations of the magnetic and structural properties of BFO, they found that the temperature dependency of the hyperfine field is assumed to be proportional to the sublattice magnetization which gives rise to a linear dependency between the internal magnetic field and the net weak ferromagnetic magnetization [20].

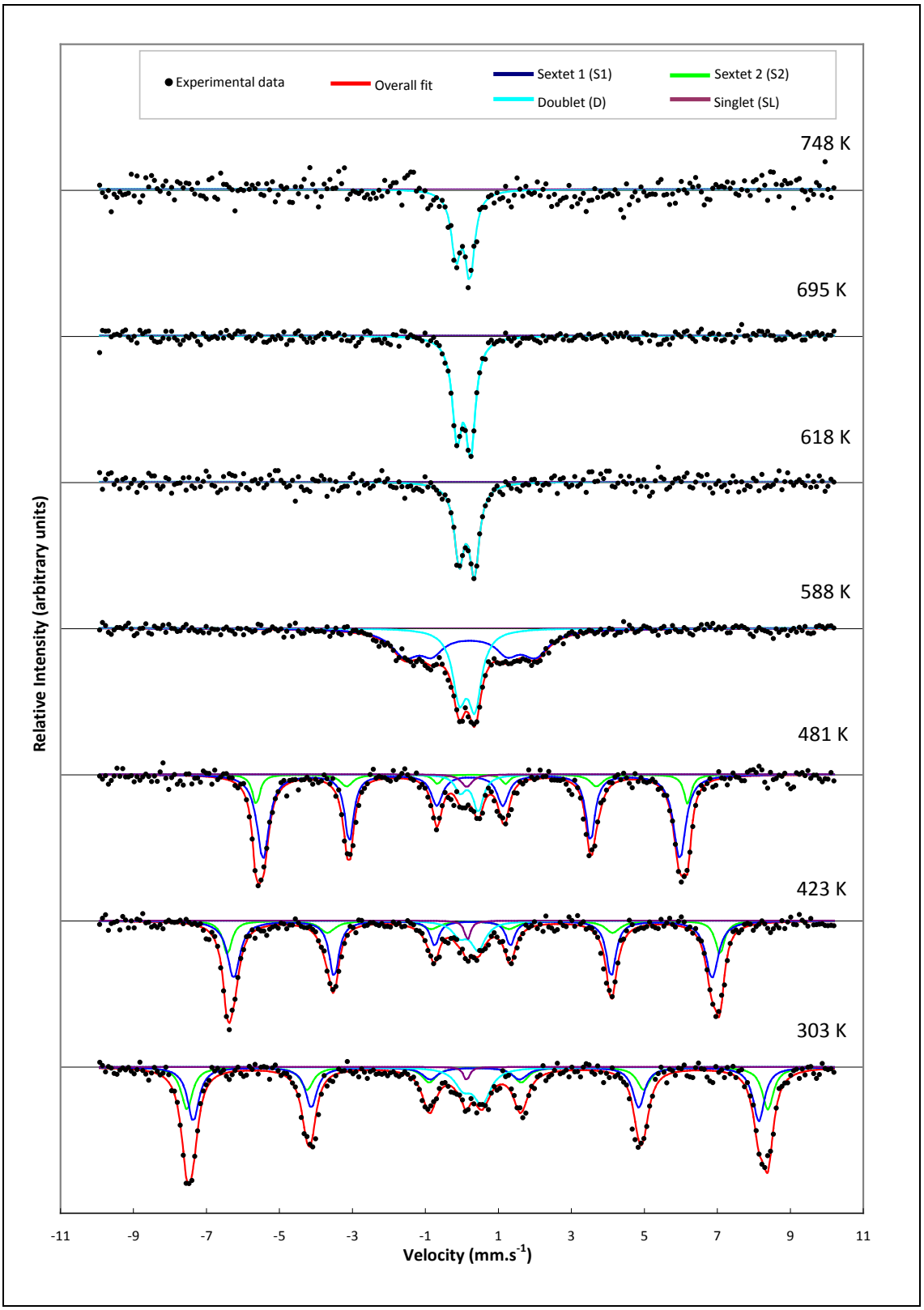


**Figure 4.9: Selected Mössbauer spectra of BHFO observed at the temperatures indicated.**

**Table 4.2: Hyperfine parameters obtained from Mössbauer measurements at room temperature on BHFO.**

| | SEXTET 1 (S1) | SEXTET 2 (S2) | DOUBLET (D) | SINGLET (SL) |
|---|---|---|---|---|
| $B_{hf}$ (T) | 47.99(8) | 49.30(6) | - | - |
| $\delta$ (mm.s$^{-1}$) | 0.37(1) | 0.40(1) | 0.29(4) | 0.13(4) |
| $\Delta E_Q$ (mm.s$^{-1}$) | 0.03(2) | 0.06(2) | 0.52(4) | - |

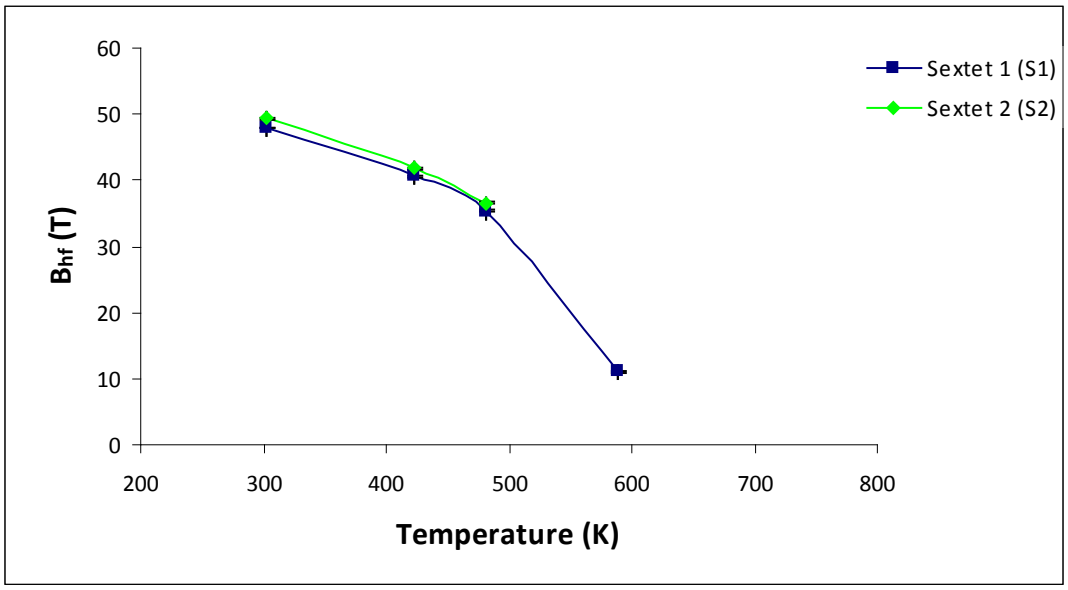


**Figure 4.10: A plot of the hyperfine magnetic field of sextets 1 and 2 as a function of temperature.**

The hyperfine fields of both the S1 and S2 components from our measurements decrease systematically to a field distribution just below the Néel temperature. At $T$ > 588 K, the hyperfine field disappears completely from the spectra which Fischer *et al.* [17] attributes to the Néel temperature. In Fischer's neutron diffraction study of the temperature dependence of the structural and magnetic order parameters of BFO, they determined the Néel temperature, $T_N$ to be 595 ±10 K, and found that the transitions from ferroelectric to paramagnetic at around 600 K.

From our measurements, we estimate the Néel temperature for BHFO to be in the range 598 – 617 K. Above the Néel temperature, only the paramagnetic doublet (D)

component is present in our spectra with hyperfine parameters of $\delta$ = 0.14 mm.s$^{-1}$ and $\Delta E_Q$ = 0.43 mm.s$^{-1}$. Kothari *et al.* [27] also observed a similar transition in their Mössbauer measurements on 0%, 10% and 15% Eu doped BFO ceramics. Their Mössbauer spectra at room temperature were defined by a sextet and at 693 K by a quadrupole split doublet. The room temperature hyperfine parameters for the 0%, 10% and 15% doped samples corresponded to $\delta_{0\%}$ = 0.383 mm.s$^{-1}$, $B_{hf}$ = 49.98 T, $\delta_{10\%}$ = 0.394 mm.s$^{-1}$, $B_{hf}$ = 49.21T, and $\delta_{15\%}$ = 0.393 mm.s$^{-1}$, $B_{hf}$ = 49.15 T. The hyperfine parameters at 696 K for the 0%, 10% and 15% doped samples were $\delta_{0\%}$ = 0.141 mm.s$^{-1}$, $\Delta E_{0\%}$ = 0.444 mm.s$^{-1}$, $\delta_{10\%}$ = 0.114 mm.s$^{-1}$, $\Delta E_{10\%}$ =0.388 mm.s$^{-1}$ and $\delta_{15\%}$ = 0.151 mm.s$^{-1}$, $\Delta E_{15\%}$ = 0.242 mm.s$^{-1}$. Above the Néel temperature, they attributed the doublet to the impurity phase $Bi_2Fe_4O_9$. They observed an increasing fraction of the paramagnetic component with increasing Eu doping, although they ruled out the contribution of the $Bi_2Fe_4O_9$ phase to the observed room temperature magnetism due to its negligible contribution.

For temperatures above the Néel temperature, Blaauw and Van der Woude [11] observed the quadrupole split doublet of BFO in the temperature range 657.3 K to 788.3 K which corresponded to $\Delta E_Q$ = 0.44 to 0.41 mm.s$^{-1}$, respectively. The doublet was fitted with an average linewidth of 0.39 mm.s$^{-1}$. The above results correlate with our data, where at $T$ > 588 K, the paramagnetic doublet with a quadrupole splitting $\Delta E_Q$ = 0.42 mm.s$^{-1}$ becomes dominant. Any misfits to the data can be ascribed to poor statistics even though the spectra were collected over an extended period of 2-3 days. This could be attributed to the fact that Bi has a very high absorption coefficient for 14.4 keV Mössbauer gamma-rays.

Figure 4.11 shows the isomer shifts of the spectral components S1, S2, D and SL as a function of temperature. The isomer shifts for all spectral components show a linear decrease with temperature. This behavior closely follows the usual second order Doppler shift variation with temperature, with the exception of SL which remains fairly constant.

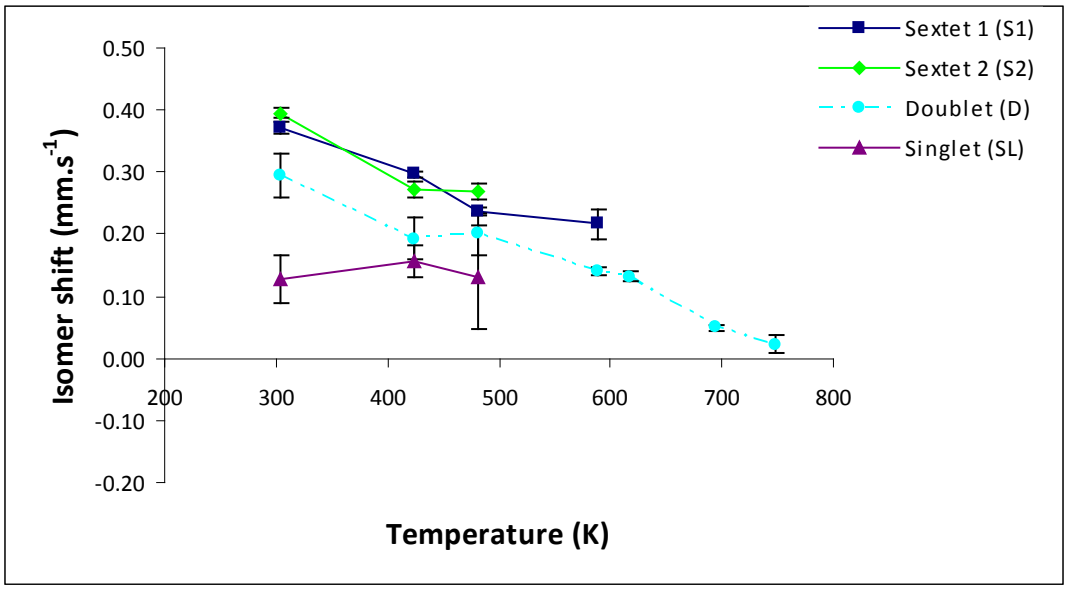


**Figure 4.11: Temperature dependence of isomer shifts observed in the Mössbauer spectra for BHFO. The isomer shifts are given relative to metallic iron.**

Figure 4.12 shows the temperature dependence of the quadrupole splitting of the doublet component observed in the Mössbauer spectra of BHFO. The doublet D decreases from $\Delta E_Q$ = 0.52 mm.s$^{-1}$ at room temperature to $\Delta E_Q$ = 0.38 mm.s$^{-1}$ at 748 K. This follows a trend that would be expected with annealing, and is within the range of values determined by Blaauw and Van der Woude [11] in their study of $BiFeO_3$ and Kothari *et al.* [27] in their study of Eu doped $BiFeO_3$.

Figure 4.13 shows the intensities of the spectral components S1, S2, S3, D, and SL against temperature. The area fraction of the spectral component S1 increases from ~ 40 % at RT to ~ 80 % at $T$ = 481 K while S2 decreases from ~30 % to ~10 %. Both components disappear at the Néel temperature, which is estimated to be above 588 K.

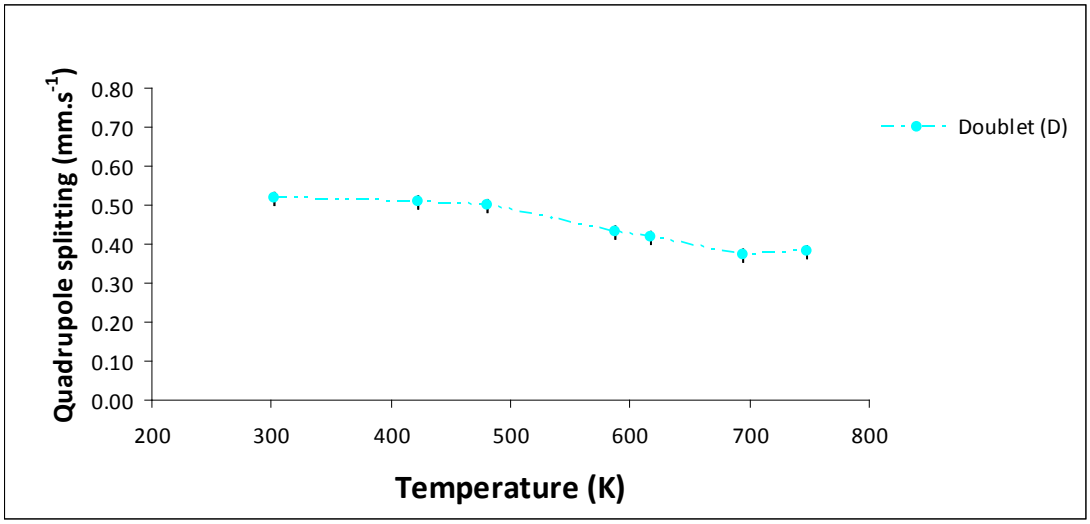


**Figure 4.12: Temperature dependence of the quadrupole splitting as observed in Mössbauer spectra of in-situ BHFO.**

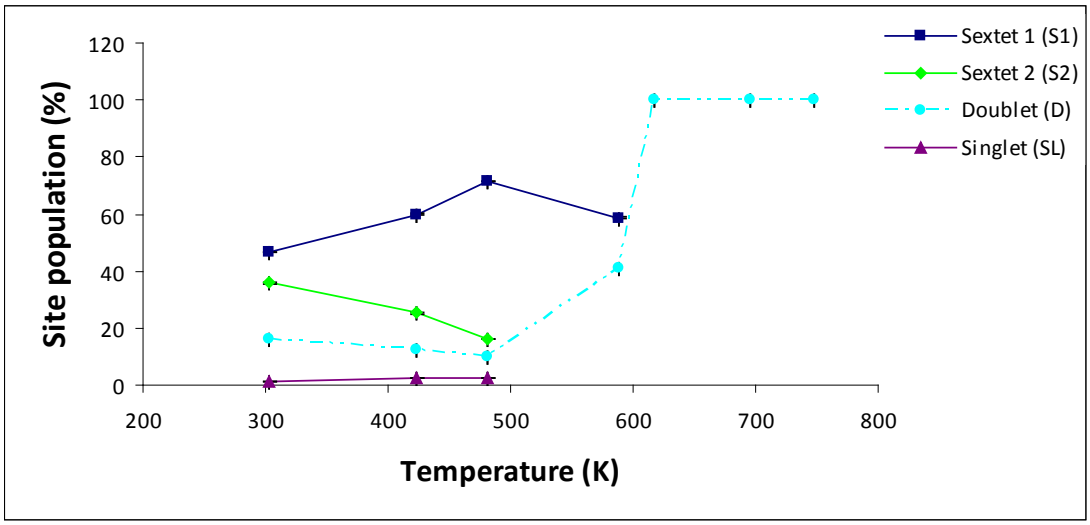


**Figure 4.13: Site population dependence as a function of temperature observed in the *in-situ* Mössbauer spectra for BHFO.**

The area fraction D increases from 10 % to 100 % between $T$ = 516 K and 748 K, where the BFHO spectra is dominated by the paramagnetic phase. At temperatures above 748 K, the sample gradually decomposed in the Mössbauer furnace. The area

fraction of the single line (SL) is fairly constant below 10% throughout the measured temperature range. From the site populations derived from the fits to the spectra, we estimate an average Debye temperature $\theta_D$ = 240 ± 81 K for BFHO. A Debye temperature of 340 ± 50 K has been previously reported for $BiFeO_3$ [11]. Our lower Debye temperature could be attributed to the fact that different crystallographic sites in the same solid have different *f*-factors [63], hence if a sample is not homogenously mixed, large discrepancies can occur. In theory, the Debye temperature can be obtained from temperature dependencies of spectral parameters like line position or spectral areas. The Debye temperature in our case was obtained from spectral areas. More details regarding the calculation of the Debye temperature can be found in Appendix B.

### 4.3.3 Fitted components assignment

The Mössbauer parameters ($B_{hf}$ = 47.99 ± 0.08 T, $\Delta E_Q$ = 0.03 ± 0.02 mm.s$^{-1}$, $\delta$ = 0.37± 0.01 mm.s$^{-1}$) obtained at room temperature for the spectral component S1 are similar to those of rhombohedral BFO ($B_{hf}$ = 49.1 T, $\Delta E_Q$ = 0.04 mm.s$^{-1}$, $\delta$ = 0.39 mm.s$^{-1}$). As discussed earlier these values are characteristic of the magnetically ordered $Fe^{3+}$ state and is due to the presence of hyperfine fields $B_{\mathrm{hf}}$ acting on the nuclear spin.

The spectral component S2 has an isomer shift of 0.40 ± 0.01 mm.s$^{-1}$, a quadrupole splitting value $\Delta E_Q$ = 0.06 mm.s$^{-1}$ and a hyperfine magnetic splitting value $B_{hf}$ = 49.30 ± 0.06 T. These values are very similar to those derived for S1.

De Sitter *et al.* [19] performed $^{57}$Fe Mössbauer measurements on $BiFeO_3$ and found that their spectra were characterized by two superimposed sextets with hyperfine magnetic fields of $B_{hf1}$ = 50.1 T, and $B_{hf2}$ = 49.8 T. These two sites were distinguished from each other by the different $\Delta E_Q$ values, which was attributed to the different

trigonal distortions of the octahedral environment of both the Fe-sites which results in different *q*-values. The isomer shift of the doublet ($\delta$ = 0.29 ± 0.04 mm.s$^{-1}$) is smaller than of the sextets ($\delta_{S1}$ = 0.37 ± 0.01 mm.s$^{-1}$, $\delta_{S2}$ = 0.40 ± 0.01 mm.s$^{-1}$ ), which implies even though all the spectral components S1, S2, and D are in the $Fe^{3+}$ state, the coordination number of the $Fe^{3+}$ in the super paramagnetic particles is lower [77].

The quadrupole splitting of doublet D is fairly constant throughout the temperature range and is attributed to the paramagnetic impurity phase, $Bi_{25}FeO_{40}$ [39]. At $T$ > 618 K, this phase completely dominates the spectra, which is in agreement with the XRD patterns discussed earlier. This presence of these phase transitions is more evident in the high temperature region and is attributed to the instability of BFO at these temperatures with weak reflections from the decomposition to the $Bi_{25}FeO_{40}$ and the minor $Bi_2Fe_4O_9$ impurity phase [73] of the SL spectral component.

# CHAPTER 5: CONCLUSIONS AND RECOMMENDATIONS

X-ray Diffraction (XRD) measurements were made at room temperature on the as-synthesized Ho substituted $BiFeO_3$ (BHFO) samples and after annealing in Argon up to 1073 K. The resultant patterns confirm that BHFO is rhombohedral with *R*3m space group, with lattice parameters of $a_{rh}$ = 3.962 Å and angle, $\alpha_{rh}$ = 89.4°. A majority $Bi_{25}FeO_{90}$ phase and a minority $Bi_2Fe_4O_9$ phase [14] have also been identified from XRD analysis which can be attributed to the local stoichometry fluctuations in BFO [69]. These impurity phases were also determined by Pradhan *et al.* [42]. After annealing in the temperature range of 673 - 873 K, a new phase was evident in our spectra and was assigned to the B-site of $Fe_3O_4$ which has been reported to have a cubic inverse spinel structure [70].

Mössbauer measurements were also conducted at room temperature on the as-synthesized Ho substituted $BiFeO_3$ samples and after annealing in Argon up to 1073 K. All the spectra were characterized by broadened features due to hyperfine distributions related to the local variations of the neigbourhood of Fe and the magnetic hyperfine splitting patterns are an indication of magnetic ordering likely screwed or slightly antiferromagnetic ordering. The spectra showed asymmetry which is associated with the inhomogeneous line broadenings and can be accounted for by the spiral magnetic structure of $BiFeO_3$.

The spectra were fitted with (a) two symmetric sextets (S1 & S2) which were present in all measured spectra (b) a symmetric sextet (S3) which was observable at annealing temperatures greater than 673 K (c) a simple Lorentzian doublet (D) and a single line (SL) which are present in all spectra. The extracted hyperfine parameters of $B_{hf}$ ~ 49 T, $\delta$ = 0.39 ± 0.01 mm.s$^{-1}$ and $\Delta E_Q$ = 0.03 ± 0.02 mm.s$^{-1}$ for sextet S1 which are consistent with those of rhombohedral $BiFeO_3$ [11] [23] [75] and are characteristic of magnetically ordered $Fe^{3+}$ due the presence of hyperfine fields acting on the nuclear spin. These values are comparable to the hyperfine parameters of

$B_{hf}$ = 49.51 T, $\delta$ = 0.386 mm.s$^{-1}$ and $\Delta E_Q$ = 0.0142 mm.s$^{-1}$ deduced by Nalwa and Garg [14] from their studies of Sm doped BFO samples. Our results of S2 are well supported by room temperature Mössbauer measurements performed by Khomchenko *et al*. [12] on Pb doped BFO samples.

At annealing temperature $T_A$ > 673 K, a third sextet (S3) was observable in our spectra with a range isomer shift values (0.62 - 0.69 mm.s$^{-1}$) and low quadrupole splitting values of 0 to 0.07 mm.s$^{-1}$. These values indicate a high symmetry cubic spinel and the Fe atoms are assigned to the non-equivalent B (octahedral) sites [76] of magnetite corresponding to a mixture of the 2+ and 3+ oxidation states [14]. The hyperfine field for S3 has been determined as 45 T. The origin of the paramagnetic doublet D is attributed to the $Bi_{25}FeO_{40}$ phase and the singlet line SL to the $Bi_2Fe_4O_9$ phase which has been observed previously in the studies of $BiFeO_3$ and doped systems [36]. The isomer shift and quadrupole splitting values of the paramagnetic doublet D at room temperature is $\Delta E_Q$ ~ 0.76 mm.s$^{-1}$, $\delta$ ~0.19 mm.s$^{-1}$ and the SL component is ~ 0.21 mm.s$^{-1}$ which corresponds to Fe with an oxidation state of 3+.

The isomer shift of S1 remained fairly constant up to $T_A$ = 623 K then decreased gradually after the appearance of S3 indicating an increase of the *s*-electron density at the Fe nucleus. The isomer shift of the spectral components S2, D and SL showed no variation with annealing temperature whilst the quadrupole splitting of S1, S3 and D also remained fairly constant with increasing temperature. The quadrupole splitting of S2 showed no systematic change with annealing temperature however at $T_A$ > 623 K, this parameter changed quite dramatically to a negative value ($\Delta E_Q$ = -0.19 mm.s$^{-1}$) with a slightly larger magnetic field ($B_{hf}$ = 51.33 T). The distribution of the isomer shift and the difference in the quadruple splitting values and signs are due the variation in the angles between the principal axis of the electric field gradient (EFG) and the spin direction. The hyperfine fields of S1 and S2 remained fairly constant for all measured samples. However at $T_A$ > 623 K, the hyperfine field of S3 showed a slight increase which could be due to Ho being substituted at the Fe site in $BiFeO_3$.

The annealing behavior of the spectral components showed different trends. The area fraction of spectral component S1 decreased from ~ 62% for the as-synthesized BHFO sample to ~ 35% for the sample annealed at $T_A$ = 873 K whilst the site population of S2 decrease from ~32% to 0%. The area fraction of component S3 increased from 17% to 59% for the samples annealed between $T_A$ = 673 K and $T_A$ = 873 K whilst the area fractions of both D and SL showed negligible change in all measured samples.

A similar fitting strategy discussed above was applied for the data acquired from the *in-situ* Mössbauer measurements (300 – 748 K) on Ho doped $BiFeO_3$ samples. The room temperature spectrum showed similar features as described above and the two sextet components (S1 and S2) with hyperfine magnetic fields of ~ 48 T and ~ 49 T decreased with increasing temperature and finally collapsed at $T$ >588 K. The hyperfine fields of both the S1 and S2 components decreased systematically with temperature to a field distribution just below the Néel temperature. Above the Néel temperature, the paramagnetic doublet (D) component with hyperfine parameters of $\delta$ = 0.14 mm.s$^{-1}$ and $\Delta E_Q$ = 0.43 mm.s$^{-1}$ dominated the spectra. For temperatures above the Néel temperature, Blaauw and Van der Woude [11] observed a similar quadrupole split doublet in the temperature range 657.3 – 788.3 K which corresponded to $\Delta E_Q$ = 0.44 to 0.41 mm.s$^{-1}$, respectively. From our measurements, we estimated the Néel temperature for BHFO to be in the range 598 – 617 K. A similar transition was also observed by Kothari *et al.* [29] in their Mössbauer measurements on 0%, 10% and 15% Eu doped BFO ceramics. The isomer shift for all spectral components from our measurements showed a linear decrease with increasing temperature which closely followed the second order Doppler shift variation with temperature. The quadrupole splitting of doublet D decreased from $\Delta E_Q$ = 0.52 mm.s$^{-1}$ at room temperature to $\Delta E_Q$ = 0.38 mm.s$^{-1}$ at 748 K, which follows a similar pattern observed by Blaauw and Van der Woude [11] and Kothari *et al.* [27].

For the area fractions, the spectral component S1 increased from ~40 % at RT to ~80 % at $T$ = 481 K while S2 decreased from ~30 % to ~10 %. These spectral components disappeared just before the Néel temperature resulting in the area fraction of D increasing to 100 % between $T$ = 516 K and 748 K where the BFHO spectra is dominated by this paramagnetic phase. At temperatures above 748 K, the sample gradually decomposed in the Mössbauer furnace. From the site populations, we estimated an average Debye temperature of $\theta_D$ = 240 ± 81 K for BFHO which is lower than the value of 340 ± 50 K that has been previously cited for $BiFeO_3$ [11]. The lower Debye temperature determined from our measurements could be attributed to the fact that different crystallographic sites in the same solid have different *f*-factors [63], hence if the sample is not homogenously mixed, large discrepancies can occur.

In conclusion, to our knowledge this dissertation has reported the first Mössbauer results on as-synthesized Ho substituted $BiFeO_3$ (BHFO) samples. However, to obtain a better understanding of the ferroelectric and magnetic properties of this material, complementary measurements are needed such as magnetization measurements using a Superconducting Quantum Interference Device (SQUID), and Electron Paramagnetic Resonance (EPR) and Nuclear Magnetic Resonance (NMR) measurements. Further, future challenges also include the development of more refined synthesis processes for the fabrication of doped $BiFeO_3$ materials for example by wet chemical methods such as the hydrothermal process in order to suppress the impurity phases that normally appear in BFO and to reduce the leakage current which normally happens due to the suppression of mobile defects.

# APPENDIX

## Appendix A: Fitting using Vinda

The as-synthesized sample and annealed Ho doped $BiFeO_3$ spectra were analyzed in a simultaneous fit using the spreadsheet based tool *Vinda* developed by H. P. Gunnlaugsson [68]. A sample fitting process and an example of error calculations is given below.

### A.1 Reading a spectrum in Vinda

The Vinda macro has a menu bar and it refers to the commands or routines in the macro file. It is attached to the file Vinda_(version).xla, and the settings for this menu bar are always redirected to the file macros_(version).xls. A spectrum is read according to the file format, which sometimes requires the file format to be changed before it can be read. Figure A1 shows a typical Vinda tool bar for spectral analysis. The calibration menu is used when performing calibration. The calibration of a Mössbauer spectra is to find the transformation that takes the *x*-axis in channels and transforms it into a velocity scale, using the spectrum of a standard, $\alpha$-Fe foil. The calibration, involves folding of a spectrum, as the spectrum is recorded twice, as the source approaches the sample and when the source moves away from the sample.

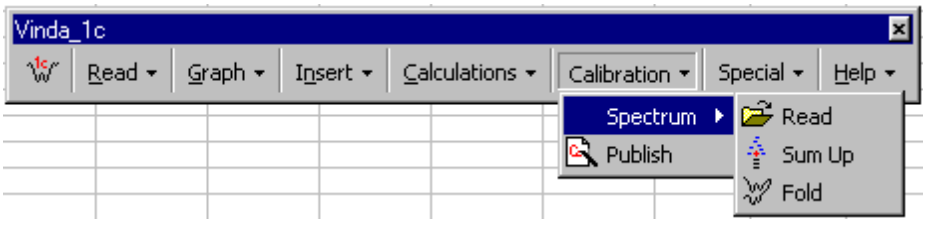


**Figure A1: The Calibration menu.**

From Figure A1, the following procedure is taken when reading the spectra into Vinda:

1. Read the spectra in. This operation is found in the calibration menu.
2. Sum up. If the spectrum is recorded in 1024 points, then 256 points are used in the analysis.
3. Find the folding offset and folding. This is done by optimizing the chi-square value at the top of the sheet by varying the folding offset. On the right of the sheet, one can graphically see the meaning of this parameter for the chi-square value. Having found the folding offset, the last operation is to fold the spectrum. Then the calibration spectrum is displayed on the main graph window to the left, together with the simulation. A typical calibration sheet is shown in Figure A2.

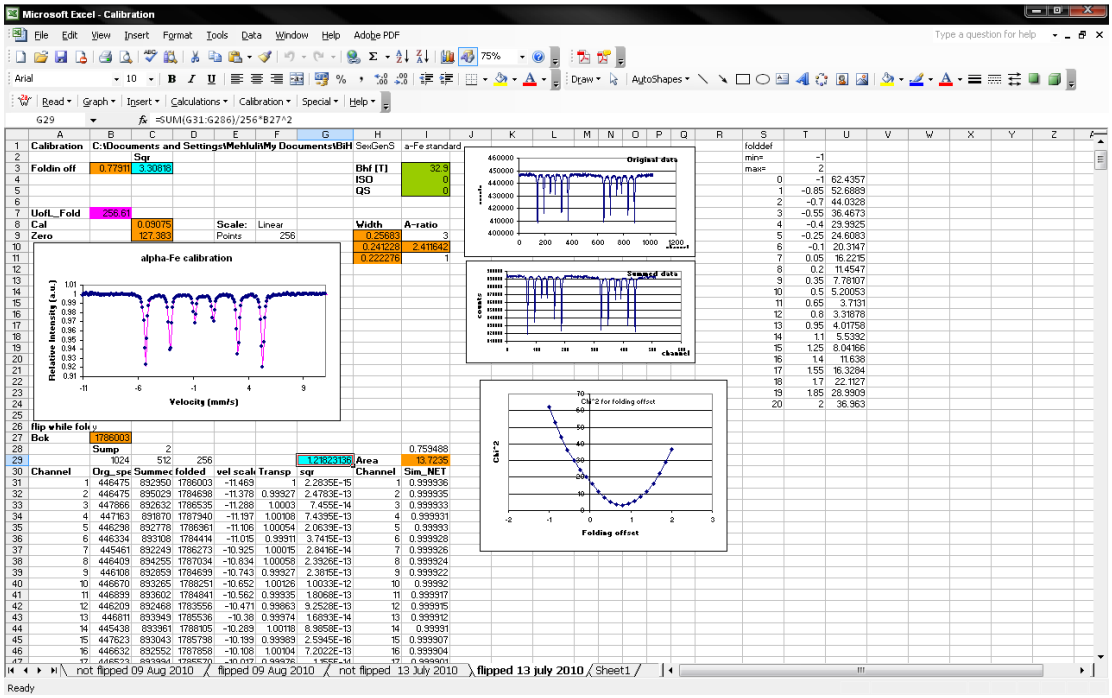


**Figure A2: A typical calibration sheet.**

The calibration sheet contains the necessary settings to perform calibration. The different colours used indicate the meaning of the different cells. For example, the green cells represent standards, and the default is $\alpha$-Fe, cyan represents chi-square

values, orange represents fitting components and yellow cells represent dependent values.

## A.2 Single Spectrum fitting

The fitting parameters (inputted in the "By Changing Cells") of a spectrum is initially varied until a reasonable fit is obtained. The basic principle of the fitting process is to minimize the chi-squared cell (F30) as shown in Figure A3 below. The solver parameter dialog box will always be executed after the target cell and the fitted parameters have been defined. The fitted parameters can vary, and are set with starting values which can change after the solver parameter has been executed. Constraints such as minimum linewidths can be also included during the fitting process as indicated in the solver dialog box.

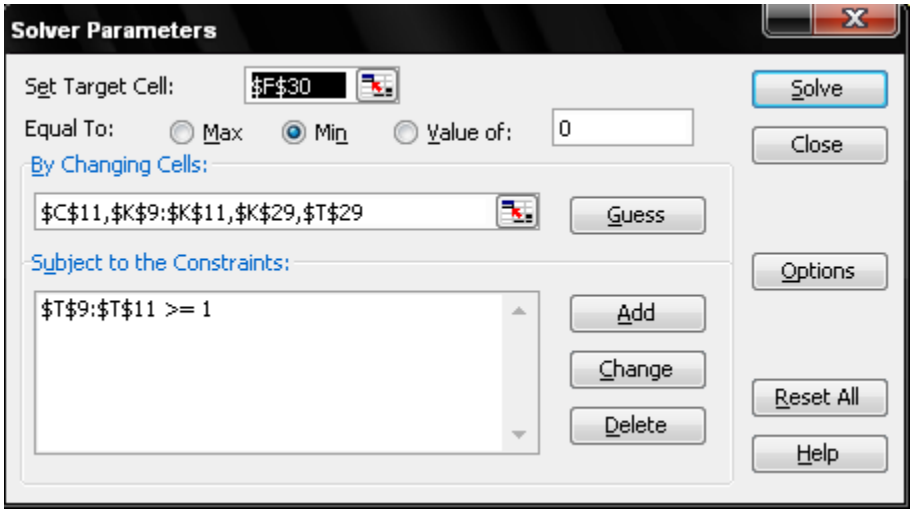


**Figure A3: Solver parameter dialog box for fitting spectra in Vinda.**

The target parameters include the background, area, linewidth, hyperfine magnetic field, isomer shift and quadrupole splitting.

Other spectra can then be fitted with the starting values from the previous spectra, by copying the fitting parameters and then reading the experimental data into a new sheet. An example of a typical spreadsheet for a single spectrum fitting from the

solving process is shown in Figure A4. The spreadsheet shows the spectrum with individual fitted spectral components and the fitting parameters.

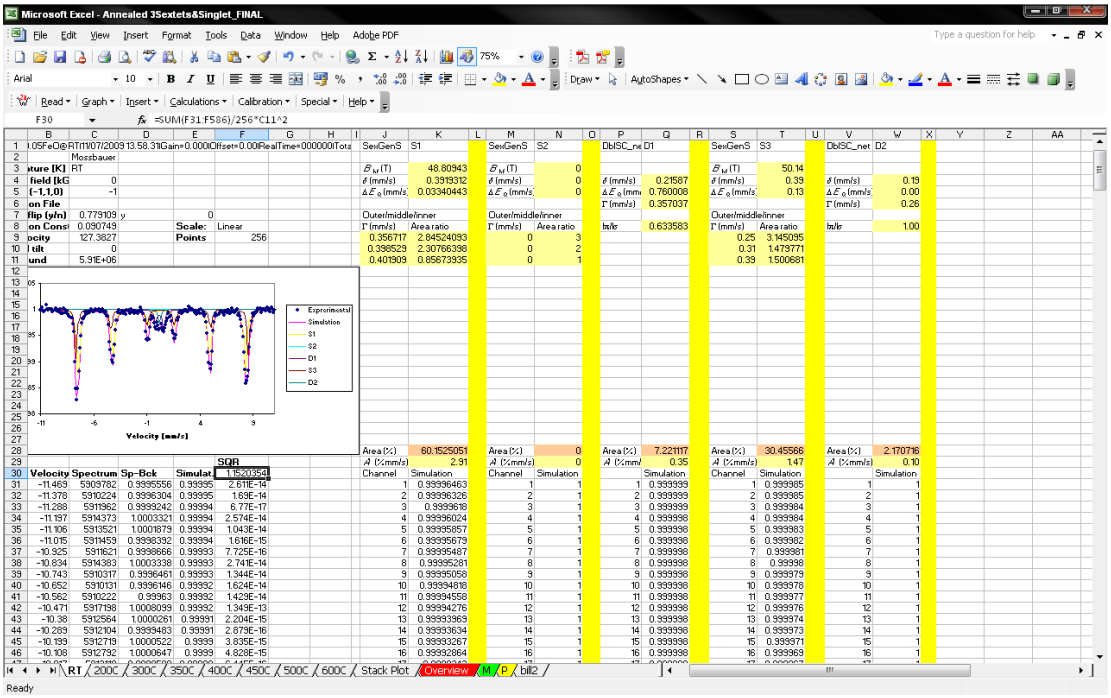


**Figure A4: Spreadsheet showing a single spectrum with fitting parameters.**

## A.2 Simultaneous fitting

When a number of Mössbauer measurements are conducted either at room temperature or *in-situ* then simultaneous fitting is utilized which allows the user to monitor how the fitted parameters vary with for example temperature. After individual spectra have been initially fitted, the fitting parameters are then collated on a single spreadsheet called the "PROG file". A reference chi-squared is then setup, which is a sum of the individual chi-squared values of each spectrum. This fitting procedure enables one to monitor the fitting variables in a single sheet. By varying the necessary cells (fitting variables) the solver program within EXCEL then converges to a solution of calculated fitted parameters. This minimization procedure is normally repeated until a meaningful result is obtained. Figure A5 shows a typical PROG sheet used in a simultaneous fit of spectra.

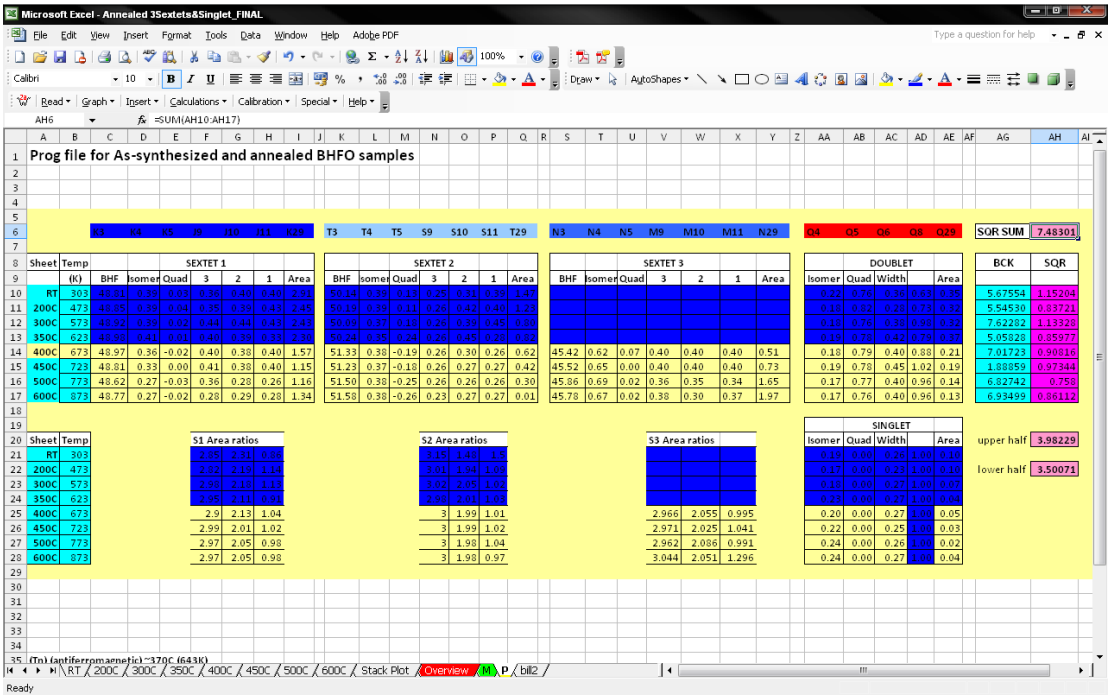


**Figure A5: A typical PROG sheet used in a simultaneous fit of spectra.**

## A.3 Error analysis

The estimated errors of the fitting parameters are determined by the $\chi^2$ value which is defined as:

$$\chi^2 = \sum_{i=1}^{N} \frac{(Data_i - Simulation_i)^2}{Data_i}$$

The value displayed on worksheets, is the value normalized by the number of data points which is convenient as $\chi^2$ approaches 1 implies a perfect fit. In the error calculations, the target cell is defined in cell F30 which should be normalized by the number of data points. The Error Analysis dialog box used in Vinda is shown in Figure A6. For more accurate results, the number of iterations should be greater than unity. A typical error calculation performed on a spreadsheet is shown in Figure A7.

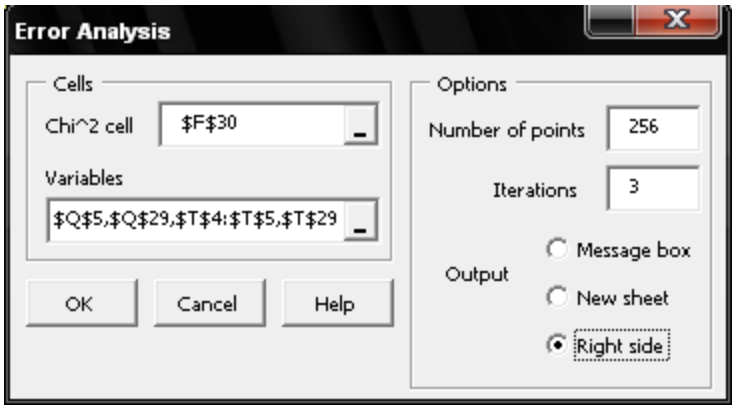


**Figure A6: A sample error analysis dialog box.**

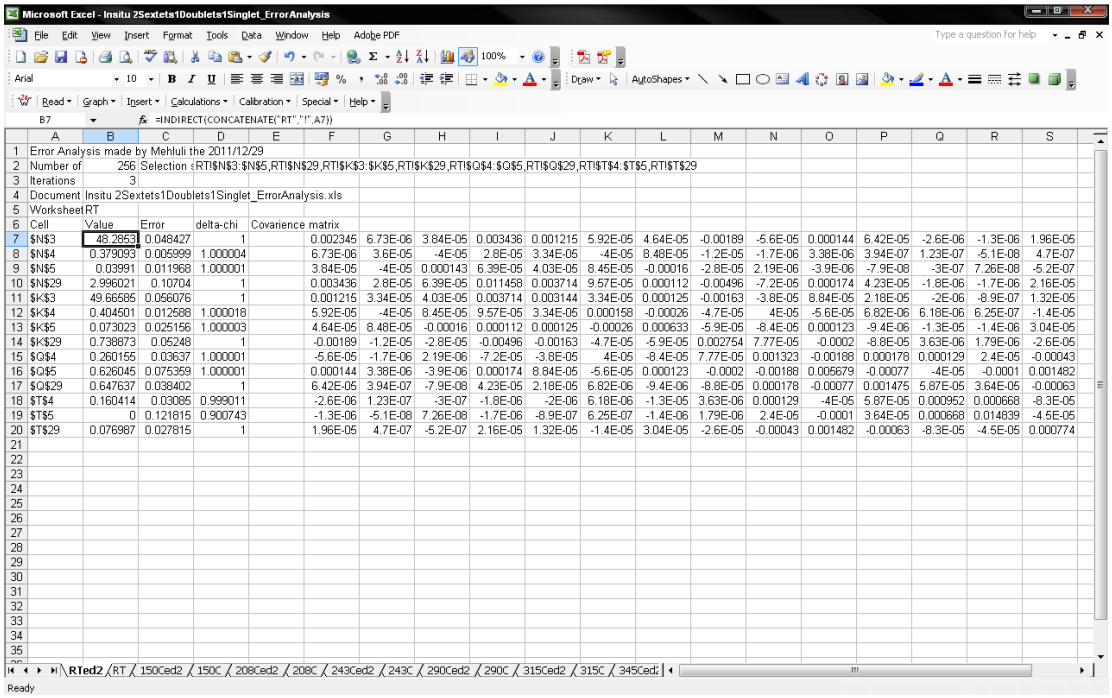


**Figure A7: Typical error calculation result sheet.**

## Appendix B: Debye temperature calculations

In Vinda, there exists a built-in function that enables one to perform Debye temperature calculations (**VindaB.Functions.ffac2([*Temp*],[*Debye*])**). This function uses the recoil free fraction, *f* known as **ffac** and site populations of spectral components as indicated in Figure B1.

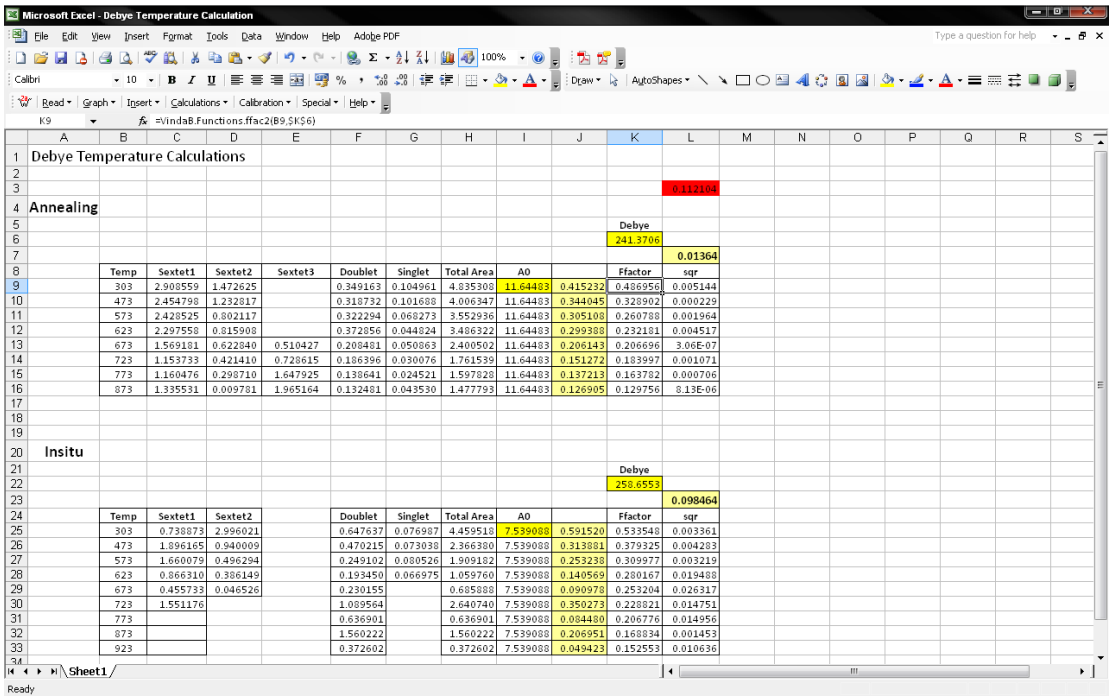

Microsoft Excel - Debye Temperature Calculation

=VindaB.Functions.ffac2(B9,$K$6)

| | A | B | C | D | E | F | G | H | I | J | K | L |
|---|---|---|---|---|---|---|---|---|---|---|---|---|
| 1 | Debye Temperature Calculations | | | | | | | | | | | |
| 3 | | | | | | | | | | | | 0.112104 |
| 4 | Annealing | | | | | | | | | | | |
| 5 | | | | | | | | | | | Debye | |
| 6 | | | | | | | | | | | 241.3706 | |
| 7 | | | | | | | | | | | | 0.01364 |
| 8 | | Temp | Sextet1 | Sextet2 | Sextet3 | Doublet | Singlet | Total Area | A0 | | Ffactor | sqr |
| 9 | | 303 | 2.908559 | 1.472625 | | 0.349163 | 0.104961 | 4.835308 | 11.64483 | 0.415232 | 0.486956 | 0.005144 |
| 10 | | 473 | 2.454798 | 1.232817 | | 0.318732 | 0.101688 | 4.006347 | 11.64483 | 0.344045 | 0.328902 | 0.000229 |
| 11 | | 573 | 2.428525 | 0.802117 | | 0.322294 | 0.068273 | 3.552936 | 11.64483 | 0.305108 | 0.260788 | 0.001964 |
| 12 | | 623 | 2.297558 | 0.815908 | | 0.372856 | 0.044824 | 3.486322 | 11.64483 | 0.299388 | 0.232181 | 0.004517 |
| 13 | | 673 | 1.569181 | 0.622840 | 0.510427 | 0.208481 | 0.050863 | 2.400502 | 11.64483 | 0.206143 | 0.206696 | 3.06E-07 |
| 14 | | 723 | 1.153733 | 0.421410 | 0.728615 | 0.186396 | 0.030076 | 1.761539 | 11.64483 | 0.151272 | 0.183997 | 0.001071 |
| 15 | | 773 | 1.160476 | 0.298710 | 1.647925 | 0.138641 | 0.024521 | 1.597828 | 11.64483 | 0.137213 | 0.163782 | 0.000706 |
| 16 | | 873 | 1.335531 | 0.009781 | 1.965164 | 0.132481 | 0.043530 | 1.477793 | 11.64483 | 0.126905 | 0.129756 | 8.13E-06 |
| 17 | | | | | | | | | | | | |
| 18 | | | | | | | | | | | | |
| 19 | | | | | | | | | | | | |
| 20 | Insitu | | | | | | | | | | | |
| 21 | | | | | | | | | | | Debye | |
| 22 | | | | | | | | | | | 258.6553 | |
| 23 | | | | | | | | | | | | 0.098464 |
| 24 | | Temp | Sextet1 | Sextet2 | | Doublet | Singlet | Total Area | A0 | | Ffactor | sqr |
| 25 | | 303 | 0.738873 | 2.996021 | | 0.647637 | 0.076987 | 4.459518 | 7.539088 | 0.591520 | 0.533548 | 0.003361 |
| 26 | | 473 | 1.896165 | 0.940009 | | 0.470215 | 0.073038 | 2.366380 | 7.539088 | 0.313881 | 0.379325 | 0.004283 |
| 27 | | 573 | 1.660079 | 0.496294 | | 0.249102 | 0.080526 | 1.909182 | 7.539088 | 0.253238 | 0.309977 | 0.003219 |
| 28 | | 623 | 0.866310 | 0.386149 | | 0.193450 | 0.066975 | 1.059760 | 7.539088 | 0.140569 | 0.280167 | 0.019488 |
| 29 | | 673 | 0.455733 | 0.046526 | | 0.230155 | | 0.685888 | 7.539088 | 0.090978 | 0.253204 | 0.026317 |
| 30 | | 723 | 1.551176 | | | 1.089564 | | 2.640740 | 7.539088 | 0.350273 | 0.228821 | 0.014751 |
| 31 | | 773 | | | | 0.636901 | | 0.636901 | 7.539088 | 0.084480 | 0.206776 | 0.014956 |
| 32 | | 873 | | | | 1.560222 | | 1.560222 | 7.539088 | 0.206951 | 0.168834 | 0.001453 |
| 33 | | 923 | | | | 0.372602 | | 0.372602 | 7.539088 | 0.049423 | 0.152553 | 0.010636 |

Sheet1

Ready

**Figure B1: A typical Debye temperature calculation in Vinda.**

This **ffac2** uses the Debye Waller factor, which can be written as;

$$f = \exp\left\{-\frac{6E_R}{k_B\theta_D}\left[\frac{1}{4}+\left(\frac{T}{\theta_D^2}\right)^2\int_0^{\frac{\theta_D}{T}}\frac{x}{e^x-1}dx\right]\right\}$$

where $k_B$ is the Boltzmann constant and the $\theta_D$ is the characteristic Debye temperature.

# REFERENCES


[1] Pokatilov V.S., Sigov A.S., and Konovalova A.O., *Bulletin of Russian Academy of Scie.: Phys.*, vol. 74, pp. 347-351, (2010).

[2] Filippetti A. and Hill N.A., *Phys. Rev.*, vol. B 65, p. 195120, (2002).

[3] Lebeugle D. et al., *Phys. Rev.*, vol. B 76, p. 024116, (2007).

[4] Wang Y., Hu J., Lin Y., and Nan C., *NPG Asia Mater.*, vol. 2(2), pp. 61 – 68, (2010).

[5] Li M., Ning M., Ma Y., Wu Q., and Ong C.K., *J. Phys. D: Appl. Phys.*, vol. 40, pp. 1603 – 1607, (2007).

[6] Benfang Y. et al., *J. Phys. D: Appl.Phys.*, vol. 41, p. 065003, (2008).

[7] Bea H. et al., *Appl. Phys. Lett.*, vol. 87, pp. 072508 – 072511, (2005).

[8] Lubk A., Gemming S., and Spaldin N.A., *Physical Review B*, vol. 80, no. 104110, (2009).

[9] Spaldin N.A. and Fiebig M., *Science*, vol. 309, p. 391, (2005).

[10] Hill N.A., *The Journal of Physical Chemistry B*, vol. 104, pp. 6694 - 6709, (2000).

[11] Blaauw C. and Van der Woude F., *J. Phy. C: Solid State Phy.*, vol. 6, pp. 1422-1431, (1973).

[12] Khomchenko V.A. et al., *J. Phy. Condes. Matter*, vol. 20, p. 155207, (2008).

[13] Liu J. et al., *Journal of Alloys and Compounds*, vol. 493, pp. 544 – 548, (2010).

[14] Nalwa K.S. and Garg A., *J. Appl. Phys.*, vol. 103, p. 044101, (2008).

[15] Singh V.R., Garg A., and Agrawal D.C., *Solid State Communications*, vol. 149, pp. 734 – 737, (2009).

[16] Liu X.H., Qu Z.X., Wei X., and Chen J., *Ceramics International*, vol. 34, pp. 797–801, (2008).

[17] Fischer P., Polomska M., Sosnowska I., and Szymanski M., *J. Phys. C: Solid State Phys.*, vol. 13, pp. 1931 – 1940, (1980).

[18] Sosnowska I., Peterlin-Neumaier T., and Steichele E., *J. Phys. C: Solid State Phys.*, vol. 15, pp. 4835 – 4846, (1982).

[19] De Sitter J., Dauwe C., De Grave E., and Govaert A., *Solid State Comm.*, vol. 18, pp. 645-646, (1976).

[20] Eibschütz M., Shtrikman S., and Treves D., *Phys. Rev.*, vol. 156, pp. 562–577, (1967).

[21] Takahashi K., Kida N., and Tonouchi M., *Phys. Rev. Lett.*, vol. 96, p. 117402, (2006).

[22] Palewicz A., Przenioslo R., Sosnowska I., and Hewat A.W., *Acta Cyst.*, vol. B63, pp. 537 – 544, (2007).

[23] Li J., Duan Y., He H., and Song D., *Journal of Alloys and Compounds*, vol. 315, pp. 259 – 264, (2001).

[24] Li J. and Jing J., *J. Mater. Sci.*, vol. 27, p. 4361, (1992).

[25] Wang L.Y. et al., *Journal of Alloys and Compounds*, vol. 469, pp. 1-3, (2009).

[26] Whitefield H.J., *Aust. J. Chem.*, vol. 20, pp. 859 – 867, (1967).

[27] Kothari D., Reddy V.R., Gupta A., Meneghini C., and Aquilanti G., *J. Phys.: Condens. Matter*, vol. 22, p. 356001 (10pp), (2010).

[28] Fiebig M., *J. Phys. D: Appl. Phys.*, vol. 38, pp. 123–152, (2005).

[29] Kothari D. et al., *J. Phys.: Condens. Matter*, vol. 19, p. 136202, (2007).

[30] Lim S.H. et al., *Appl. Phys. Lett.*, vol. 92, pp. 012918 – 012910, (2008).

[31] Mazumder R., Devi P.S., Bhattacharya D., Choudhury P., and Sen A., *Appl. Phys. Lett.*, vol. 91, pp. 062510 – 062512, (2007).

[32] Pina P.C., Buentello R., Arriola H., and Nava E.N., *Hyp. Int.*, vol. 185, pp. 173 – 177, (2008).

[33] Chu Y. et al., *Nature Materials*, vol. 7, pp. 478 – 482, (2008).

[34] Zavaliche F. et al., *Phase Transitions*, vol. 79, pp. 991–1017, (2006).

[35] Zampiere R.B., de Medeiros S.N., Santos I.A., and Paesano Jr. A., "Development of gas sensors based on Fex(Bi2O3)1-x composites," Universidade Estadual de Maringa, (2008).

[36] Santos I.A et al., *Ferroelectrics*, vol. 338, (2006).

[37] Kostiner E. and Shoemaker G.L., *Journal of Solid State Chemistry*, vol. 3, pp. 186 – 189, (1971).

[38] Vandenberghe R.E., Nedkov I., Merodiiska T., and Slavov L., *Hyp. Int.*, vol. 165, pp. 267 – 271, (2005).

[39] Santos I.A et al., *Journal of Non-Crystalline Solids*, vol. 352, pp. 3721 – 3724, (2006).

[40] Qi X.D., Dho J., Tomov R., Blamire M.G., and MacManus-Driscoll J.L., *Appl. Phys. Lett.*, vol. 86, pp. 062903 – 062905, (2005).

[41] Al-Haj M., *Cryst. Res. Technol.*, vol. 45, pp. 89-93, (2010).

[42] Pradhan S.K. et al., *Journal of Physics and Chemistry of Solids*, vol. 71, pp. 1557-1564, (2010).

[43] Wang Y., *Journal of Applied Physics*, vol. 109, p. 124105, (2011).

[44] Lide D.R., *CRC Handbook of Chemistry and Physics*, 75th ed.: CRC Press, (1994), pp. 10–227.

[45] Mössbauer R.L., "Kernresonanz fluoresent von Gammastrahlung in Ir 191.," *Z. Phys.*, vol. 151, pp. 124-143, (1958).

[46] Gütlich P., Bill E., and Trautwein A.X., *Mössbauer Spectroscopy and Transition Metal Chemistry: Fundamentals and Applications*., (1978), pp. 84-87.

[47] Greenwood N.N. and Gibb T.C., *Mössbauer Spectroscopy*., (1971), pp. 9-16.

[48] Kuzmann E., Nagy S., and Vertes A., *Pure Appl. Chem.*, vol. 75, pp. 801-858, (2003).

[49] Terence C.G., "Principles of Mössbauer Spectroscopy," pp. 11-25, (1976).

[50] Dickson D.P.E. and Berry F.J., *Mössbauer Spectroscopy*., (1947), pp. 2–16.

[51] Gütlich P., Bill E., and Trautwein A.X., *Mössbauer Spectroscopy and Transition Metal Chemistry: Fundamentals and Applications*., (1978), pp. 4 -10.

[52] Parak F., "Radioactive 57Co source," Muchen DE, 4406697, (1983).

[53] Gunnlaugsson H.P. et al., *Hyp. Int.*, vol. 169, pp. 1391-1323, (2006).

[54] "http://science.jrank.org/pages/4083/Magnetism-Types-magnetism.html," (website).

[55] Feynman R.P., Robert L., and Matthew S., *The Feynman Lectures on Physics*, vol. 2, (1963).

[56] Kittel C., *Introduction to Solid State Physics*, 6th, Ed.: John Wiley and Sons, (1986).

[57] "http://wwwchem.uwimona.edu.jm:1104/courses/magnetism.html," (website).

[58] Cadogan J.M. and Ryan D.H., "Mössbauer Spectroscopy," pp. 210-212, (2006).

[59] Gütlich P., Bill E., and Trautwein A.X., *Mössbauer Spectroscopy and Transition Metal Chemistry: Fundamentals and Applications*., (1978), pp. 205-231.

[60] Siedel C.W., *Mössbauer Spectroscopy: Principles and Practice*., pp. 308-321.

[61] Palewicz A., Przenioslo R., Sosnowska I., and Margiolaki C., *Solid State Comm.*, vol. 140, pp. 359-363, (2006).

[62] Hearne G.R., Pasternak M.P, and Taylor R.D., *Rev. Sci. Instrum.*, vol. 65, no. 3787, (1994).

[63] Rancourt D.G., *Nuclear Instr. And Methods in Phys. Research*, vol. B44, pp. 199-210, (1989).

[64] Dyar M.D., Agresti D.G., Schaefer M.W., Grant C.A., and Sklute E.C., *Earth Planet Science*, pp. 83 – 95, (2006).

[65] Dyar M.D., *American Mineralogist*, vol. 69, pp. 1127-1144, (1984).

[66] Gancedo J.R., Gracia M., and Marco J.F., *Hyperfine Interactions*, vol. 83, pp. 71-78, (1994).

[67] "http://wissel-gmbh.de/," (website).

[68] Gunnlaugsson H.P., "Personal Communication," (2008 -2009).

[69] Priyadarshini D., Dash B.N., Rath H., Rath C., and Mishra N.C., *Indian J. Phys.*, vol. 83, pp. 485- 491, (2009).

[70] Uribe J.D. et al., *Microelectronics Journal*, vol. 39, pp. 1391–1393, (2008).

[71] Béa H. et al., *Appl. Phys. Lett.* , vol. 87, no. 072508, (2005).

[72] Lou X.J., Yang C.X., Zhang M., and Scott J.F., *Appl. Phys. Lett.* , vol. 90, pp. 262908 – 26298-3, (2007).

[73] Selbach S.M., Tybell T., Einarsrud M., and Grande T., *Adv. Mater.*, vol. 20, pp. 3692–3696, (2008).

[74] Rancourt D.G. and Ping J.Y., *Nuclear Instruments and Methods in Physics Research*, vol. B58, pp. 85-97, (1991).

[75] Michael C., Moreau J., Achenbach G.D., Gerson R., and James W. J., *Solid State Comm.*, vol. 7, pp. 701 – 704, (1969).

[76] Lee C.S. and and Joe Y.H., *Journal of the Korean Physical Society*, vol. 56, pp. 85 - 88, (2010).

[77] Li J., He H., Lu F., Duan Y., and Song D., *Mat. Res. Soc. Sym. Proc.*, vol. 676, (2001).